
Non-linear Gravitational Clustering in the Universe

By
Nishikanta Khandai

Harish Chandra Research Institute, Allahabad

Submitted to the
Board of Studies in Physical Science Discipline

In partial fulfilment of the requirements

For the degree of

DOCTOR OF PHILOSOPHY

of

Homi Bhabha National Institute



August, 2009

Certificate

This is to certify that the Ph.D. thesis titled “*Non-linear Gravitational Clustering in the Universe*” submitted by Nishikanta Khandai is a record of bona fide research work done under my supervision. It is further certified that the thesis represents independent work by the candidate and collaboration was necessitated by the nature and scope of the problems dealt with.

Date:

Prof. J. S. Bagla

Thesis Advisor

Declaration

This thesis is a presentation of my original research work. Whenever contributions of others are involved, every effort is made to indicate this clearly, with due reference to the literature and acknowledgement of collaborative research and discussions.

The work is original and has not been submitted earlier as a whole or in part for a degree or diploma at this or any other Institution or University.

This work was done under guidance of Prof. J. S. Bagla, at Harish Chandra Research Institute, Allahabad.

Date:

Nishikanta Khandai

Ph.D. Candidate

To My Family....

Acknowledgments

At the outset I would like to thank my parents for supporting me all throughout this endeavour. I would also like to thank my wife Tanusree who has been a constant source of support and encouragement ever since I have known her.

I would then like to thank my advisor Jasjeet for having been so patient with me for all these years. A great deal of what I have learnt is through discussions with him.

I'd like to also thank my collaborators Jayanti, Girish, Jaswant and Kanan. I would like to thank Sriram and Kandu for helping me out for the next phase of my academic cycle. The coursework at HRI was wonderful and I thank my teachers for it.

I would like to thank Daniel J. Price for clarifying several issues regarding their implementation of the adaptive code. I thank Martin White, Volker Springel, Alessandro Romeo, Hugh Couchman, Jun Makino and Ravi Sheth for useful discussions and comments on my manuscripts.

The efficient administrative and engineering staff have made living in HRI very convenient. I will take back many good memories of my friends, batchmates and seniors, it was fun knowing all of them.

Numerical experiments for this thesis were carried out at cluster computing facility in the Harish-Chandra Research Institute (<http://cluster.hri.res.in>). I thank Farooqui for addressing all my cluster related problems. This research has made use of NASA's Astrophysics Data System.

Contents

1	Introduction	3
1.1	The Expanding Universe	4
1.1.1	The Einstein deSitter Model	6
1.1.2	Expansion of the Universe and its effect on Observables	7
1.1.3	The Newtonian Limit	9
1.2	Cosmological Evolution of the Density Field	11
1.2.1	Particle Dynamics in an Expanding Universe	11
1.2.2	Growth of Perturbations	12
1.3	Statistical Measures of Clustering	14
1.3.1	Correlation Function and Power Spectra	14
1.3.2	Mass variance	16
1.3.3	The radial pair-velocity	17
1.4	Non-linear gravitational clustering	18
1.4.1	The Zeldovich approximation	18
1.4.2	Spherical collapse	19
1.4.3	The Press-Schechter formalism	22
2	A Modified TreePM Code	25
2.1	Cosmological N-body simulations	25

2.2	The TreePM Algorithm	27
2.2.1	Moving particles	28
2.3	The scheme of groups	29
2.3.1	Estimating Speedup	30
2.4	A Modified TreePM Algorithm	32
2.4.1	Optimum Parameters of The Modified TreePM Algorithm	32
2.4.2	Errors in Force	36
2.5	A Hierarchy of Timesteps	42
2.6	Discussion	44
3	The Adaptive TreePM Code	47
3.1	Introduction	48
3.2	Adaptive Force Softening	50
3.2.1	Formalism	50
3.3	The Adaptive TreePM Method	53
3.3.1	Estimating the Softening Length	54
3.3.2	Memory Requirements	55
3.3.3	Timestepping Criterion and Integration	56
3.3.4	Cell Acceptance Criterion For ATreePM	57
3.4	Performance characteristics	59
3.4.1	Timing	59
3.4.2	Errors	61
3.5	Validation of the Adaptive TreePM code	64
3.5.1	Two-body collisions: plane wave collapse	64
3.5.2	Convergence with n_n and relevance of the $\nabla\epsilon$ term	66
3.6	Discussion	78
4	Mass function of haloes	83

CONTENTS ix

4.1	Introduction	84
4.2	The Mass Function	86
4.3	Numerical Simulations	88
4.4	Analysis and Results	91
4.5	Discussion	95
4.6	Conclusions	100
5	HI Power Spectrum	103
5.1	Introduction	104
5.2	Modeling the HI distribution	105
5.2.1	<i>N</i> -Body Simulations	109
5.3	Results	117
5.3.1	Bias	119
5.3.2	Radio Maps	126
5.4	Discussion	127
6	Prospects for Detection of HI	131
6.1	Signal and Noise	132
6.1.1	Visibility Correlation	133
6.1.2	System Noise in the Visibility Correlation	134
6.1.3	Noise in Images	137
6.2	Simulated Maps & Signal	138
6.2.1	Visibility Correlation	141
6.2.2	Rare Peaks	142
6.3	Discussion	144

Abstract

Large scale structures traced by galaxies are believed to have formed by amplification of small perturbations. Galaxies are highly over-dense systems, matter density ρ in galaxies is thousands of times larger than the average density $\bar{\rho}$ in the universe. Typical density contrast ($\delta \equiv \rho/\bar{\rho} - 1$) in matter at these scales in the early universe was much smaller than unity in the early universe. Thus the problem of galaxy formation and the large scale distribution of galaxies requires an understanding of the evolution of density perturbations from small initial values to the large values we encounter today.

Initial density perturbations were present at all scales that have been observed. The equations that describe the evolution of density perturbations in an expanding universe have been known for several decades and these are easy to solve when the amplitude of perturbations is small. Once density contrast at relevant scales becomes comparable to unity, perturbations becomes non-linear and coupling with perturbations at other scales cannot be ignored. The equation for evolution of density perturbations cannot be solved for generic initial conditions in this regime. N-Body simulations are often used to study the evolution in this regime.

In this thesis we first develop the numerical tools, and use it to study aspects of gravitational clustering in an expanding universe.

N-Body Methods

A Modified TreePM Code

In chapter 2 we discuss the performance characteristics of using the modification of the tree code suggested by Barnes (1990) in the context of the TreePM code. The optimization involves identifying groups of particles and using only one tree walk to compute force for all the particles in the group. This modification has been in use in our implementation of the TreePM code for some time, and has also been used by others in codes that make use of tree structures.

In this work, we present the first detailed study of the performance characteristics of this optimization. We show that the modification, if tuned properly can speed up the TreePM code by a significant amount. However we show that this optimization not only results in a speedup but computes forces more accurately. Force is explicitly computed at three levels: (i) short range particle-particle (PP) interactions for intra-group particles, (ii) short-range particle-cell (PC) interactions using the BH-Tree and finally (iii) long-range particle-mesh (PM) interactions are computed using Fast Fourier Transforms.

We also demonstrate that this approach optimizes cache utilization in modern processors. We also combine this modification with the use of individual time steps and indicate how to combine these two schemes in an optimal fashion. We find that the combination is at least a factor of two faster than the modified TreePM without individual time steps. Overall performance is often faster by a larger factor, as the scheme of groups optimizes use of cache for large simulations.

The modified method is very well suited and was essential for the development of the Adaptive TreePM method discussed in the next section. The reason for this is that the hierarchy of time steps helps in evolving trajectories for particles with very different softening length, and the modified cell acceptance criterion of the modified TreePM is useful in reducing the force calculation to an effective particle-particle interaction where symmetrization of force does not add a significant overhead.

The Adaptive TreePM method

In chapter 3 we discuss a new N -body code.

One of the limitations of most cosmological codes has been the use of a force softening length that is much smaller than the typical inter-particle separation. This is true of fixed resolution codes. This leads to departures from collisionless evolution that is desired in these simulations. We propose a particle based method with an adaptive resolution where the force softening length is reduced in high density regions while ensuring that it remains well above the local inter-particle separation. The method, called the Adaptive TreePM, is based on the modified TreePM code.

We present the mathematical model and an implementation of this method, and demonstrate that the results converge over a range of options for parameters introduced in generalizing the code from the TreePM code. We reformulate the equations of motion so that energy-momentum conservation is not violated when going from a fixed resolution code to an adaptive resolution code.

We explicitly demonstrate collisionless evolution in collapse of an oblique plane wave. We compare the code with the fixed resolution TreePM code and also an implementation that mimics adaptive mesh refinement methods and comment on the agreement, and disagreements in the results. We find that in most respects the ATreePM code performs at least as well as the fixed resolution TreePM in highly over-dense regions, from clustering and number density of haloes, to internal dynamics of haloes. We also demonstrate that the Adaptive Code is able to better resolve the internal structure of halos and show that the adaptive code is faster than the corresponding high resolution TreePM code.

Aspects of Gravitational Clustering

Mass function of haloes: scale invariant models

In chapter 4 we use the N -body code discussed in chapter 2 to study the clustering properties of dark matter halos through the Mass Function. The Mass Function describes the number density of halos of a given mass in a given cosmology. Even though this relates to a

highly non-linear regime of gravitational clustering, simple theoretical arguments have been used to obtain the form for the mass function that describes results of N-Body simulations to within a factor of a few.

The Press-Schechter mass function is based on the spherical collapse model and has been shown to fit poorly to simulations. On the other hand the Sheth-Tormen mass function is based on the more realistic ellipsoidal collapse model as it becomes possible to take tidal forces due to fluctuations at larger scales into account. The Sheth-Tormen mass function matches the simulations much better than the Press-Schechter mass function. Both of these are based on theoretical arguments and have a universal form, independent of the shape of the initial power spectrum and also insensitive to changes in the cosmological model.

In the last few years, large N-Body simulations of the LCDM model have demonstrated that the mass function is not universal, and various groups have given epoch and cosmology dependant fitting functions for this model. The LCDM model has a gradually varying effective spectral index at relevant scales and a different cosmological background, and this makes the published results difficult to interpret in terms of a theoretical model. We approach this problem differently and see whether the non-universal description can be attributed to a spectrum dependence of the form of the mass function. We specifically look at scale free cosmologies in an Einstein De Sitter background and look for departures of non-universality. This choice of cosmology does not introduce any scale into the problem. These models have the advantage of being self-similar, hence stringent checks can be imposed while running these simulations. We provide spectrum dependent fits for the parameters in the Sheth-Tormen mass function, and show that this allows us to fit simulation data much better. We also show explicitly that the best fit Sheth-Tormen parameters have a clear dependence on power spectrum. Our results also indicate that an improved analytical theory with more parameters is required in order to provide better fits to the mass function.

HI as a probe of the large scale structure

In chapters 5 and 6 we focus on modeling the redshifted 21cm line of neutral Hydrogen (H I) in high resolution dark matter simulations. We study the H I power spectrum and

its evolution and predict prospects for detection, both statistical and direct.

Power Spectrum and its evolution

The redshifted 21cm line is a promising probe of the Epoch of Reionization. However it can also be used for studying large scale structure in the post reionization epoch. Observations tell us that the neutral density parameter $\Omega_{\text{HI}} \simeq 0.001$ in the redshift range $1 \leq z \leq 5$ and is locked in dense clumps. We model the distribution of HI in the post-reionization universe. This model uses gravity only N-Body simulations and an ansatz to assign HI to dark matter haloes that is consistent with observational constraints and theoretical models. The additional feature that we obtain is the bias of HI with respect to Dark Matter, which in earlier work was taken to be unity or derived from very low resolution simulations. We use high resolution simulations to determine scale dependent HI bias over a range of redshifts. Higher resolution simulations are used at larger redshifts in order to cover the range of halo masses where significant amount of HI may be present. The characteristic mass of haloes is smaller at early times and hence higher resolution simulations are required. We highlight the significantly high bias for the HI distribution at small scales. This aspect has not been discussed before and it implies that a statistical detection of HI at large scales and direct detection of the brightest regions at moderate redshifts requires comparable integration time using existing telescopes.

Visibility correlations and prospects for detection

We follow the determination of HI power spectrum in the post-reionization era with computation of visibility correlations. Possibility of a statistical detection using visibility correlations is discussed. Simulated maps of the HI distribution in the post-reionization era are also constructed to study the prospects for direct detection with existing and upcoming radio telescopes. We show that the GMRT¹ and an upgraded MWA² (MWA5000) can potentially detect signal from the HI distribution at high redshifts. MWA5000 can detect visibility correlations at large angular scales at all redshifts accessible to it in the post-reionization

¹Giant Meterwave Radio Telescope. See <http://gmrt.ncra.tifr.res.in> for details.

²The Murchison Widefield Array. See <http://www.mwatelescope.org/> for details.

era. The GMRT can detect visibility correlations at lower redshifts, specifically there is a strong case for a survey at $z \simeq 1.3$. We also discuss prospects for direct detection of rare peaks in the HI distribution using the GMRT. We show that direct detection should be possible with integration time that is comparable to, or even less than, the time required for a statistical detection.

List of Publications

1. The Adaptive TreePM: An adaptive resolution code for cosmological N-body simulations
Authors: Bagla J. S. and Khandai Nishikanta
2009, MNRAS, 396, 2211
2. A Modified TreePM code
Authors: Khandai Nishikanta and Bagla J. S.
2008, Research In Astronomy and Astrophysics 9, 861-873
3. Mass function of haloes: scale invariant models
Authors: Bagla J. S. and Khandai Nishikanta, Girish Kulkarni
2009, arXiv:0908.2702
4. H I as a probe of the large scale structure in the post-reionization universe: Power Spectrum and its evolution.
Authors: Bagla J. S. and Khandai Nishikanta
2009, arXiv:0908.3796
5. H I as a probe of the large scale structure in the post-reionization universe: Visibility correlations and prospects for detection.
Authors: Khandai Nishikanta, Datta Kanan K. and Bagla J. S.
2009, arXiv:0908.3857

Other Publications:

1. Effects of the size of cosmological N-body simulations on physical quantities — III: Skewness
Authors: Bagla J. S., Prasad Jayanti and Khandai Nishikanta
2009, MNRAS, 395, 918
2. Fractal dimensions as a measure of homogeneity
Authors: Yadav Jaswant, Bagla J. S. and Khandai Nishikanta
2009, Manuscript in Preparation

Contents

Chapter 1

Introduction

One of the most important discoveries in modern cosmology was that we live in an expanding Universe (Hubble, 1929). It was observed that galaxies are receding from us with a speed proportional to the distance. Current estimate of the expansion rate is $H_0 = 71.9^{+2.6}_{-2.7} \text{ km/s/Mpc}$ (Komatsu et al., 2009; Mould et al., 2000). If we extrapolate backwards in time then one sees that densities and temperature are singular at an epoch. This singularity is called the Big Bang.

Large scale structures traced by galaxies are believed to have formed by amplification of small perturbations (Peebles, 1980; Padmanabhan, 1993; Peacock, 1999; Padmanabhan, 2002; Bernardeau et al., 2002). Observations of galaxies tell us that these are uniformly distributed on very large scales (Yadav et al., 2005; Sarkar et al., 2009), the scale of homogeneity being $\sim 70h^{-1} \text{ Mpc} - 80h^{-1} \text{ Mpc}$. However they tend to cluster at small scales forming complex structures like filaments, sheets and voids. The measurements of the earliest fluctuations come from observations of the Cosmic Microwave Background (CMB) radiation. These are fluctuations in the radiation field which has come directly to us from the early Universe and are of the order of $\Delta T/T \sim 10^{-5}$ at large scales (Smoot et al., 1992; Komatsu et al., 2009) These observations also suggest that the content of the Universe can be broken down into ordinary matter or baryons, ($\sim 4\%$), cold dark matter $\sim 22\%$ and dark energy $\sim 74\%$

The goal of the study of structure formation in the Universe is to understand the

formation and physical properties of galaxies and their clustering starting from small initial perturbations with a given spectrum. This involves the study of non-linear gravitational clustering along with other physical processes in an expanding Universe. On large scales the clustering properties are dictated by gravity alone. However on small scales non-gravitational effects contribute significantly. The first visible objects are believed to have formed in potential wells generated by highly overdense dark matter haloes. Therefore in order to understand the clustering of galaxies one first needs to understand how dark matter clusters.

In this chapter we describe the basic framework in which one can understand the evolution of perturbations in an expanding Universe. We then describe the tools that are needed in understanding the properties of clustering.

1.1 The Expanding Universe

We begin by describing, in this section, the standard big-bang cosmology (Peebles, 1993; Weinberg, 2008). The assumption that the Universe is homogeneous and isotropic on large scales leads to the choice of a spacetime coordinate system for which the metric takes the simple form known as the Friedmann-Lemaitre-Robertson-Walker (FLRW) metric, Friedmann (1922); Robertson (1929, 1935); Walker (1936); Lemaître (1931b,a):

$$ds^2 = -c^2 dt^2 + a^2(t) \left[\frac{dx^2}{1 - kx^2} + x^2(\sin^2 \theta d\phi^2 + d\theta^2) \right] \quad (1.1)$$

Here $a(t)$ is the scale factor, (x, θ, ϕ) the comoving coordinate (coordinates of the fundamental observer), k is the curvature constant. Values of k can be $+1$, 0 or -1 and the Universe will be closed, flat or open respectively. t is the cosmic time.

We relate the observationally measured coordinates r also known as the *physical* or *proper* coordinates to the comoving coordinate \mathbf{x} by $\mathbf{r}(t) = a(t)\mathbf{x}$. We then have the proper velocity of a given observer:

$$\dot{\mathbf{r}}(t) = \dot{a}(t)\mathbf{x} + a(t)\dot{\mathbf{x}} = \mathbf{v}_h + \mathbf{v}_p \quad (1.2)$$

Where the second term \mathbf{v}_p is called the *peculiar* velocity of objects. In the absence of

peculiar velocities we have:

$$\mathbf{v}_h = \left[\frac{\dot{a}(t)}{a(t)} \right] a(t) \mathbf{x} = \left[\frac{\dot{a}(t)}{a(t)} \right] \mathbf{r}(t) \equiv H(t) \mathbf{r}(t) \quad (1.3)$$

This is the Hubble Law with $H(t)$ being Hubble's parameter. Hubble's constant is its value today, i.e., at $t = t_0$. Thus the expansion of the Universe leads to objects moving away from us at a speed proportional to the distance.

The evolution of $a(t)$ is governed by the matter and energy density in the Universe. In order to compute for $a(t)$ we have to solve Einstein's field equations for the FLRW metric.

$$G_{\mu\nu} - \Lambda g_{\mu\nu} = 8\pi G T_{\mu\nu} \quad (1.4)$$

with $G_{\mu\nu} \equiv R_{\mu\nu} - \frac{1}{2}g_{\mu\nu}R$ the Einstein tensor and $R_{\mu\nu}, R$ and $g_{\mu\nu}$ are the Ricci tensor, Ricci scalar and the metric tensor respectively. $T_{\mu\nu}$ is the energy-momentum tensor, Λ is the cosmological constant and G is the gravitational coupling constant. Under the assumptions of homogeneity and isotropy $T_{\mu\nu}$ takes the form (we have taken $c = 1$):

$$T_{\mu\nu} = dia[-\bar{\rho}(t), p(t), p(t), p(t)] \quad (1.5)$$

here $p(t)$ is the pressure and $\bar{\rho}(t)$ is the energy density. Using the R_{00} and R_{ii} components of the Ricci tensor and equating them with the corresponding components of the energy-momentum tensor we obtain:

$$\frac{\dot{a}^2 + k^2}{a^2} = \frac{8\pi G}{3}\bar{\rho} + \frac{\Lambda}{3} \quad (1.6)$$

$$2\ddot{a} + \frac{\dot{a}^2 + k^2}{a^2} = -8\pi Gp + \Lambda \quad (1.7)$$

These two equations alongwith the equation of state (EoS) $p = p(\bar{\rho})$, completely determine the three functions, $a(t)$, $\bar{\rho}(t)$, $p(t)$. Using the conservation of the energy-momentum tensor, $T_{;\nu}^{\mu\nu} = 0$ one obtains, (equivalently one could have used eq. 1.6 and eq. 1.7):

$$\frac{d}{da}(\bar{\rho}a^3) = -3a^2p \quad (1.8)$$

Given an EoS $p = p(\bar{\rho})$ one can integrate this equation to obtain $\bar{\rho} = \bar{\rho}(a)$. For an EoS of the form $p = w\bar{\rho}$, the density varies as

$$\bar{\rho} \propto a^{-3(1+w)} \quad (1.9)$$

The constituents in our Universe can typically be classified as radiation and relativistic matter, with EoS $p_{rad} = \frac{1}{3}\bar{\rho}_{rad}$, non-relativistic matter with EoS $p_{nr} \approx 0$ and the cosmological constant with $p_\Lambda = -\bar{\rho}_\Lambda$. Using eq. 1.9 one sees that the corresponding energy density scales as $\bar{\rho}_{rad} \propto a^{-4}$, $\bar{\rho}_{nr} \propto a^{-3}$ and $\bar{\rho}_\Lambda = \text{constant}$, independent of a . In other words expansion of the Universe dilutes the energy density of radiation and non-relativistic matter.

It is possible to define a characteristic density in terms of the Hubble constant, eq. 1.3, the critical density $\bar{\rho}_c$ defined as:

$$\rho_c = \frac{3H_0^2}{8\pi G} \quad (1.10)$$

$\bar{\rho} = \bar{\rho}_{rad} + \bar{\rho}_{nr}$ is the sum of both relativistic and non-relativistic matter. We define the dimensionless density parameter for the i^{th} component of matter:

$$\Omega_i \equiv \frac{\bar{\rho}_i(t_0)}{\rho_c} \quad (1.11)$$

Eq. 1.6 can now be rewritten as:

$$\frac{\dot{a}^2}{a^2} + \frac{k}{a^2} = H_0^2 \left[\Omega_{rad} \left(\frac{a_0}{a} \right)^2 + \Omega_{nr} \left(\frac{a_0}{a} \right)^3 + \Omega_\Lambda \right] \quad (1.12)$$

$$H^2(a) = H_0^2 \left[\Omega_{rad} \left(\frac{a_0}{a} \right)^2 + \Omega_k \left(\frac{a_0}{a} \right)^2 + \Omega_{nr} \left(\frac{a_0}{a} \right)^3 + \Omega_\Lambda \right] \quad (1.13)$$

where $\Omega_k = \Omega_{nr} + \Omega_{rad} + \Omega_\Lambda - 1$ with $k = a_0^2 H_0^2 \Omega_k$ is the density parameter due to the curvature and $\Omega_\Lambda = \frac{\Lambda}{3H_0^2}$. Observations tells us that $\Omega_{tot} = \Omega_{nr} + \Omega_{rad} + \Omega_\Lambda = 1.099^{+0.100}_{-0.085}$ (Komatsu et al., 2009) which tells us that Universe is nearly flat, $\Omega_k = \Omega_{tot} - 1 \approx 0$.

1.1.1 The Einstein deSitter Model

The Einstein deSitter model is perhaps the simplest cosmological model where one considers a flat Universe with only non-relativistic matter, i.e. $\Omega_{tot} = \Omega_{nr} = 1.0$. With $p = 0$ one obtains using eq. 1.8:

$$\frac{d}{da} (\bar{\rho} a^3) = 0 \Rightarrow \bar{\rho}(t) = \bar{\rho}(t_0) \left[\frac{a(t_0)}{a(t)} \right]^3 \quad (1.14)$$

Substituting it in eq. 1.6 one can solve for $a(t)$ given the initial condition $a(t = 0) = 0$:

$$a(t) = [6\pi G \bar{\rho}(t_0)]^{\frac{1}{3}} a(t_0)^{\frac{2}{3}} \quad (1.15)$$

If we normalise $a(t)$ to unity today, i.e. at $a(t_0) = 1$, we obtain:

$$6\pi G \bar{\rho}(t_0) = t_0^{-2} \Rightarrow a(t) = \left(\frac{t}{t_0}\right)^{\frac{2}{3}} \quad (1.16)$$

The Einstein deSitter Universe expands forever with a decelerating rate of expansion and the density decreases as:

$$\bar{\rho}(t) = \frac{1}{6\pi G t^2} \quad (1.17)$$

1.1.2 Expansion of the Universe and its effect on Observables

The expansion of the Universe affects the measurements of physical quantities. Here we describe some of them.

- *The Hubble scale:*

The Hubble parameter defines a time scale and can be used to define a length scale (Peebles, 1980; Padmanabhan, 1993) over which physical processes act coherently. The comoving Hubble radius is defined as

$$d_H(z) = \frac{c}{H(z)} \quad (1.18)$$

This is also the scale at which general relativistic effects become important. For $l \ll d_H$ Newtonian gravity is often adequate.

- *Redshifting of emitted frequency:*

Suppose a source is emitting a signal at a frequency ν_{em} . If the the observer is static with respect to the source then the observed frequency, ν_{obs} , is the same as the emitted frequency, $\nu_{obs} = \nu_{em}$. If there is a relative motion between observer and source then $\nu_{obs} \neq \nu_{em}$ and the shift may be defined as $1 + z = \nu_{em}/\nu_{obs}$. If the relative speed v is much smaller than the speed of light then this shift is $z = v/c$. Suppose now that the

observer and source are separated by an infinitesimal distance δr . Due to expansion the relative velocity is $\delta v = \frac{\dot{a}}{a}\delta r$ and the relative frequency shift is:

$$\frac{\delta\nu}{\nu} = -\frac{\delta v}{c} = -\frac{1}{c}\frac{\dot{a}}{a}\delta r = -\frac{\dot{a}}{a}\delta t = -\frac{da}{a} \quad (1.19)$$

Where we have used the fact that light travels on a null surface, $c\delta t = \delta r$ This implies that

$$\nu(t)a(t) = \text{constant} \quad (1.20)$$

and the frequency shift z can be written as

$$1 + z(t) = \frac{a(t_0)}{a(t)} \quad (1.21)$$

Expansion of the Universe leads to a decrease in frequency, or a *redshifting* of the frequency. The redshift function $z(t)$ and scale factor $a(t)$ are equivalent descriptors of expansion and can be used as time variables. A decrease in frequency leads to an increase in wavelength $\lambda_{obs} = \lambda_{em}(1 + z)$

- *Scaling of momentum due to expansion:*

One can use similar arguments to show that the momentum of particles (Padmanabhan, 1996) decreases due to expansion.

$$p(t)a(t) = \text{constant} \quad (1.22)$$

In the case of non-relativistic motion $v \propto p$ hence the proper velocity also decreases as a^{-1} due to expansion.

- *The luminosity distance and angular diameter distance:*

Consider an emitter and an observer in a static Universe. The source has luminosity L . Then in a time interval dt it emits energy Ldt . The observed flux is

$$Sdt = \frac{Ldt}{4\pi^2 D^2} \quad (1.23)$$

Here D is the distance between emitter and observer. In an expanding Universe this distance is given by integrating over the null geodesic in the radial direction:

$$c \int_{t_e}^{t_{obs}} \frac{dt}{a(t)} = \int_0^D \frac{dx}{1 - kx^2} \quad (1.24)$$

The energy is received in a time interval dt_{obs} and is related to the time interval for emission dt_e by $dt_e/a(t_e) = dt_{obs}/a(t_{obs})$. Similarly the radiation is redshifted by a factor $a(t_e)/a(t_{obs})$. The flux is received in a sphere of surface $4\pi^2 D^2 a^2(t_{obs})$. The observed flux is therefore:

$$\begin{aligned} S &= \frac{dt_e}{dt_{obs}} \frac{a(t_e)}{a(t_{obs})} \frac{L}{4\pi^2 a^2(t_{obs}) D^2} \\ &= \frac{L}{4\pi^2 a^2(t_{obs}) D^2 (1+z)^2} \end{aligned} \quad (1.25)$$

It is convenient to define a quantity called the *Luminosity Distance*, $D_L(z) = a(t_{obs})D(1+z)$ which reduces the above equation to a form similar to the expression in the case of a static Universe, eq. 1.23.

$$Sdt = \frac{Ldt}{4\pi^2 D_L^2(z)} \quad (1.26)$$

Similar considerations can be used to define quantity called the *Angular Diameter Distance*, $D_A(z)$, for relating the angular size of an object in an expanding Universe. These two distance measures are related by

$$D_A(z)(1+z)^2 = D_L(z) \quad (1.27)$$

1.1.3 The Newtonian Limit

In principle, the process of structure formation should be studied in a fully covariant manner within the theory of general relativity. However Newtonian mechanics is generally valid at most scales of cosmological interest. It is valid in regions which are small compared to the Hubble radius $l \ll d_H$ and large compared to the Schwarzschild radius of most massive black holes. Newton's equations of motion (EoM) are recovered in the weak field limit of general relativity, i.e., when $\Phi \ll c^2$. Conversely if one assumes that particle motions are non-relativistic $v^2/c^2 \ll 1$ one can reduce an arbitrary metric to the following form (Landau & Lifshitz, 1975) in the Newtonian limit:

$$ds^2 = -(c^2 + 2\Phi_{av})dt^2 + d\mathbf{r}^2 \quad (1.28)$$

with $\Phi_{av} \ll c^2$. Here Φ_{av} is the effective Newtonian potential that should be used in the equations of motion.

Consider the following coordinate transformation in the FLRW metric:

$$\begin{aligned}\mathbf{r} &= a(t)\mathbf{x} \\ \bar{t} &= t - t_0 + \frac{1}{2} \frac{H(t)a^2(t)}{c^2}x^2 + \mathcal{O}(x^4) = t - t_0 + \frac{H^{-1}}{2} \frac{a^2x^2}{d_H^2} + \mathcal{O}(x^4)\end{aligned}\quad (1.29)$$

Where d_H is the Hubble radius. In the above transformation the spatial coordinates have been changed from comoving to the proper coordinates and the time has been corrected for the gravitational redshift. The transformation changes the metric to:

$$ds^2 = - \left[1 - \frac{\ddot{a}}{a} \frac{r^2}{c^2} \right] c^2 d\bar{t}^2 + \left[1 + \left(\frac{\dot{a}}{a} \right)^2 \frac{r^2}{c^2} + \frac{k}{a^2} r^2 \right] dr^2 + r^2 [d\theta^2 + \sin^2 \theta d\phi^2] \quad (1.30)$$

Here we have ignored cubic and higher order terms in $r/d_H \ll 1$ because we are only interested in regions that are small compared to the Hubble radius. The coefficient of dr^2 can be set to unity if $v^2/c^2 \ll 1$, $r \ll d_H$ and $r \ll d_k$. Here $d_k = ca/\sqrt{k}$ is the curvature scale. The line element then reduces to :

$$ds^2 = - \left[1 - \frac{\ddot{a}}{a} \frac{r^2}{c^2} \right] c^2 d\bar{t}^2 + dr^2 + r^2 [d\theta^2 + \sin^2 \theta d\phi^2] \quad (1.31)$$

Comparing this with eq. 1.28 one can identify the the effective Newtonian potential due to the homogeneous and isotropic background Universe.

$$\Phi_{av} = - \frac{1}{2} \frac{\ddot{a}}{a} r^2 = \frac{2}{3} \pi G (\bar{\rho} + 3p) \quad (1.32)$$

For a Universe with only non-relativistic matter and cosmological constant the potential takes the form:

$$\Phi_{av} = \left(\frac{2}{3} \pi G \bar{\rho}_{nr} - \frac{1}{6} \Lambda \right) r^2 = \left(\frac{1}{4} H_0^2 \Omega_{nr} \frac{a_0^3}{a^3} - \frac{1}{2} H_0^2 \Omega_\Lambda \right) r^2 \quad (1.33)$$

The potential and the Newtonian approximation are valid only when the particle motions are non-relativistic, and the scales of interest are much smaller than the Hubble scale. Gravitational clustering occurs at scales which are much smaller than the scale of homogeneity, which current studies estimate it to be $\sim 70h^{-1}Mpc$ (Yadav et al., 2005; Sarkar et al., 2009) This scale is indeed much smaller than the Hubble scale $\sim 3000h^{-1}Mpc$. We can therefore study gravitational clustering in the Newtonian framework.

1.2 Cosmological Evolution of the Density Field

1.2.1 Particle Dynamics in an Expanding Universe

The dynamical evolution of a self-gravitating set of particles can be described by the following equations:

$$\begin{aligned}\ddot{\mathbf{r}}(t) &= \ddot{a}(t)\mathbf{x}(t) + 2\dot{a}(t)\dot{\mathbf{x}}(t) + a\ddot{\mathbf{x}}(t) = -\nabla\Phi_{tot} = -\nabla(\Phi_{av} + \phi) \\ \nabla_r^2\Phi_{tot} &= \nabla_r^2(\Phi_{av} + \phi) = 4\pi G\rho - \Lambda = (4\pi G\bar{\rho} - \Lambda) + 4\pi G\bar{\rho}\delta \\ \rho(\mathbf{r}) &= \sum_i m_i \delta_D^3(\mathbf{r} - \mathbf{r}_i)\end{aligned}\tag{1.34}$$

Here \mathbf{r}_i is the position of the i^{th} particle, Φ_{tot} is the total gravitational potential, with a contribution from the background Universe Φ_{av} and that due to perturbations in it ϕ . ρ is the density field of the set of particles, m_i the mass of the i^{th} particle and δ is the density contrast characterising the perturbations in the density field defined as

$$\delta(\mathbf{r}) = \frac{\rho(\mathbf{r}) - \bar{\rho}}{\bar{\rho}(t)}\tag{1.35}$$

The terms corresponding to the background expansion can be identified, in the limit $\delta = 0$, as

$$\ddot{a}\mathbf{x} = -\nabla_r\Phi_{av}(t) \quad \text{or} \quad \Phi_{av}(t) = -\frac{1}{2}a\ddot{a}x^2 = -\frac{1}{2}\frac{\ddot{a}}{a}r^2\tag{1.36}$$

Where we have recovered eq. 1.32. The rest represents the equation of motion of particles due to fluctuations in the density

$$a\ddot{\mathbf{x}} + 2\dot{a}\dot{\mathbf{x}} = -\nabla_r\phi\tag{1.37}$$

We finally obtain for the EOM due to the perturbed field using eq. 1.13 and eq. 1.34

$$\begin{aligned}\ddot{\mathbf{x}} + 2\frac{\dot{a}}{a}\dot{\mathbf{x}} &= -\frac{\nabla_r\phi(\mathbf{x}, t)}{a} = -\frac{\nabla_x\phi(\mathbf{x}, t)}{a^2} \\ \nabla_x^2\phi = 4\pi G a^2 \bar{\rho} \delta &= \frac{3}{2}H_0^2\Omega_{nr}\frac{\delta}{a}\end{aligned}\tag{1.38}$$

In the Universe without perturbations the perturbed potential $\phi = 0$. We then see from the above equation that $a^2\dot{x} = a\mathbf{v}_p = \text{constant}$. Thus the velocity dependant term in the EOM acts as a damping term and the timescale of damping is fixed by the rate of expansion $H(t) = \dot{a}/a$. The expansion time scale in a matter dominated Universe $t_{exp} \sim (G\bar{\rho})^{-1/2}$ and the collapse time scale goes as $t_{col} \sim (G\rho)^{-1/2} \simeq (G\bar{\rho})^{-1/2}(1 - \delta/2)$, both of which are of the same order. Therefore the growth of perturbations is slow as compared to a static Universe.

1.2.2 Growth of Perturbations

The complete equations

The density contrast grows with time as overdense regions collapse and accrete matter at the expense of under dense regions. We can follow the evolution of the density contrast by combining the EOM, eqs. 1.38 with the expression for density, eq. 1.34. The Fourier component $\delta_{\mathbf{k}}$ of the density contrast $\delta_{\mathbf{x}} \equiv \delta(\mathbf{x}, t)$ are related through a Fourier transform:

$$\delta_{\mathbf{x}}(t) = \int \frac{d^3\mathbf{k}}{(2\pi)^3} \delta_{\mathbf{k}}(t) \exp(i\mathbf{k} \cdot \mathbf{x}) \quad (1.39)$$

$$\delta_{\mathbf{k}}(t) = \int \frac{d^3\mathbf{x}}{V} \delta_{\mathbf{x}}(t) \exp(-i\mathbf{k} \cdot \mathbf{x}) \quad (1.40)$$

Using eq. 1.34 and eqs. 1.38 we obtain the evolution equation for Fourier components of the density contrast (Peebles, 1980).

$$\ddot{\delta}_{\mathbf{k}} + 2\frac{\dot{a}}{a}\dot{\delta}_{\mathbf{k}} = 4\pi G\bar{\rho}_{nr}\delta_{\mathbf{k}} + A_{\mathbf{k}} - B_{\mathbf{k}} \quad (1.41)$$

where

$$A_{\mathbf{k}} = 2\pi G\bar{\rho}_{nr} \sum_{\mathbf{k}' \neq 0, \mathbf{k}} \left[\frac{\mathbf{k}' \cdot \mathbf{k}}{|\mathbf{k}'|^2} + \frac{\mathbf{k} \cdot (\mathbf{k} - \mathbf{k}')}{|\mathbf{k} - \mathbf{k}'|^2} \right] \delta_{\mathbf{k}'} \delta_{\mathbf{k}-\mathbf{k}'} \quad (1.42)$$

$$B_{\mathbf{k}} = \frac{1}{M} \sum_{i=1,N} m_i (\mathbf{k} \cdot \dot{\mathbf{x}}_i)^2 \exp(-i\mathbf{k} \cdot \mathbf{x}_i) \quad M = \sum_{i=1,N} m_i \quad (1.43)$$

$A_{\mathbf{k}}$ and $B_{\mathbf{k}}$ are non-linear coupling terms between different modes. $B_{\mathbf{k}}$ couples density contrasts in an indirect manner through peculiar velocities of particles.

The linear limit

One can obtain the linear limit ($\delta_{\mathbf{k}} \ll 1$) by dropping terms that are quadratic or of higher order in perturbed quantities.

$$\ddot{\delta}_{\mathbf{k}} + 2\frac{\dot{a}}{a}\dot{\delta}_{\mathbf{k}} = 4\pi G\bar{\rho}_{nr}\delta_{\mathbf{k}} \quad (1.44)$$

It can be shown that in a Universe without a relativistic component, the Hubble parameter itself is a solution of the equation (Heath, 1977). That is however a decaying solution. The second solution can be obtained using the Wronskian(Heath, 1977).

$$\begin{aligned} X &= 1 + \Omega_{nr} \left(\frac{1}{a} - 1 \right) + \Omega_{\Lambda}(a^2 - 1) \\ b(t) &\propto \frac{X^{1/2}}{a} \int^a \frac{da}{X^{3/2}} \end{aligned} \quad (1.45)$$

$b(t)$ is the growing mode of density perturbations.

This can be easily solved in an Einstein deSitter Universe $X = a^{-1}$ and $b(t) \propto a(t) = (t/t_0)^{2/3}$. The growth rate is a power law with a small index as compared to an exponential rate in a static Universe (Jeans, 1902). One can cast the EOM eq.1.38 in a useful form by using the growing mode as a time function:

$$\begin{aligned} \frac{d\mathbf{u}}{db} &= -\frac{3}{2}\frac{Q}{b}(\mathbf{u} - \mathbf{g}) \\ \nabla^2\psi &= \frac{\delta}{b} \end{aligned} \quad (1.46)$$

where

$$\begin{aligned} \mathbf{g} &\equiv -\nabla\psi = -\frac{2}{3H_0^2\Omega_{nr}} \left(\frac{a}{b} \right) \nabla\phi \\ Q &= \left(\frac{\bar{\rho}_{nr}}{\rho_c} \right) \left(\frac{\dot{a}\dot{b}}{ab} \right)^2 = \left(\frac{\bar{\rho}_{nr}}{\rho_c} \right) \frac{1}{f^2} \end{aligned} \quad (1.47)$$

and $\mathbf{u} \equiv d\mathbf{x}/db$ is the generalised velocity, ψ the generalised potential, \mathbf{g} the generalised force, and $f = d\ln(b)/d\ln(a)$. This form of casting the EOM is particularly useful since the generalised acceleration $d\mathbf{u}/db = 0$ in the linear regime and hence one can relate the

generalised velocity \mathbf{u} to the generalised force \mathbf{g} at early times. In an Einstein deSitter Universe, $a = b$ and $Q = 1$. Therefore the EOM reduces to:

$$\frac{d\mathbf{u}}{da} = -\frac{3}{2a}(\mathbf{u} - \mathbf{g}) \quad (1.48)$$

1.3 Statistical Measures of Clustering

There are *two general approaches to the empirical study of large scale matter distribution* ... *the botanical and the statistical* (Peebles, 1980). The former deals with studying and classifying objects on an individual basis while the latter deals with studying the gross properties of matter distribution using statistical methods. When dealing with vast amount of data one has to resort to statistical methods. In this section we outline some of the statistical measures used in studying clustering properties of matter.

1.3.1 Correlation Function and Power Spectra

Spatial properties of a statistically homogeneous set of points (be it galaxies and other objects in observations or simulation particles) are characterised by n -point correlation functions. The 2-point correlation function is defined as:

$$\xi(\mathbf{r}) = \langle \delta(\mathbf{x})\delta(\mathbf{x} + \mathbf{r}) \rangle \quad (1.49)$$

The angular brackets indicate an averaging extending over all space. Therefore

$$\xi(\mathbf{r}) = \frac{1}{V} \int d^3x \delta(\mathbf{x})\delta(\mathbf{x} + \mathbf{r}) \quad (1.50)$$

Let $\delta_{\mathbf{k}}$ be the Fourier transform of $\delta(\mathbf{r})$. Since $\delta(\mathbf{r})$ is a real quantity $\delta_{\mathbf{k}}$ satisfies the reality condition $\delta_{-\mathbf{k}} = \delta_{\mathbf{k}}^*$. We therefore get:

$$\begin{aligned}
\xi(\mathbf{r}) &= \frac{1}{V} \int d^3x \int \frac{d^3k}{(2\pi)^3} \delta_{\mathbf{k}} \exp[-\iota \mathbf{k} \cdot \mathbf{x}] \int \frac{d^3k'}{(2\pi)^3} \delta_{\mathbf{k}'} \exp[-\iota \mathbf{k}' \cdot (\mathbf{x} + \mathbf{r})] \\
&= \int \frac{d^3k}{(2\pi)^3} \delta_{\mathbf{k}} \int \frac{d^3k'}{(2\pi)^3} \delta_{\mathbf{k}'} \exp[-\iota \mathbf{k}' \cdot \mathbf{r}] \left[\frac{1}{V} \int d^3x \exp[-\iota (\mathbf{k}' + \mathbf{k}) \cdot \mathbf{x}] \right] \\
&= \int \frac{d^3k}{(2\pi)^3} \delta_{\mathbf{k}} \int \frac{d^3k'}{(2\pi)^3} \delta_{\mathbf{k}'} \exp[-\iota \mathbf{k}' \cdot \mathbf{r}] \delta_D(\mathbf{k}' + \mathbf{k}) \\
&= \int \frac{d^3k}{(2\pi)^3} |\delta_{\mathbf{k}}|^2 \exp[-\iota \mathbf{k} \cdot \mathbf{r}] \\
&= \int \frac{d^3k}{(2\pi)^3} P(\mathbf{k}) \exp[-\iota \mathbf{k} \cdot \mathbf{r}]
\end{aligned} \tag{1.51}$$

We define the power spectrum $P(\mathbf{k})$ as the Fourier transform of the 2-point correlation function.

In an isotropic Universe the perturbations cannot have a preferred direction, therefore we have the property, $\xi(\mathbf{r}) = \xi(r)$ and $P(\mathbf{k}) = P(k)$. The angular part of the k -space integral of eq. 1.51 can be performed easily and we obtain:

$$\begin{aligned}
\xi(r) &= \frac{1}{(2\pi)^3} \int P(k) \frac{\sin(kr)}{kr} 4\pi k^2 dk \int \frac{k^3 P(k)}{(2\pi^2)} \frac{\sin(kr)}{kr} \frac{dk}{k} \\
&= \int \Delta^2(k) \frac{\sin(kr)}{kr} d \ln k
\end{aligned} \tag{1.52}$$

Where the power spectrum has been expressed in dimensionless form

$$\Delta^2(k) = \frac{k^3 P(k)}{(2\pi^2)} \tag{1.53}$$

The meaning of $\Delta^2(k)$ is similar to the power spectrum, in that it is a measure of the fluctuations in density but in a logarithmic interval in k . It is the Fourier space counterpart of $\xi(r)$. Thus $\Delta^2(k) = 1$ means that density fluctuations have a typical amplitude equal to unity at scales around $1/k$.

If the density field is a Gaussian random field, then all higher order moments can be expressed in terms of the 2-point functions. In most cosmological models the initial density field is chosen to be a Gaussian random field.

Just as the 1-point function, the density contrast $\delta(r)$, is defined as the excess density over the average and can be thought of as the excess number of points (if one thinks of sampling the density field by random points), the 2-point function $\xi(r)$ can be interpreted as a measure, on the average, excess number of *pairs* separated by a distance r . If one chooses to sit on a given particle location¹ then $\xi(r)$ can be thought of as counting, on the average, the excess (over the mean) number of neighbours for a given particle within the interval $[r, r + dr]$. Thus if a point is chosen from a distribution then the average number of neighbours at a distance r in an infinitesimal volume δV is

$$\delta N_2 = \bar{n} \delta V [1 + \xi(r)] \quad (1.54)$$

Here \bar{n} is the number density of the distribution. Similarly the three-point correlation function can be defined in terms of pairs to complete a triangle with a randomly chosen point.

$$\delta N_3 = \bar{n}^2 \delta V_2 \delta V_3 [1 + \xi(r_{12}) + \xi(r_{13}) + \xi(r_{13}) + \zeta(r_{12}, r_{13}, r_{23})] \quad (1.55)$$

Here $r_{ij} = |\mathbf{r}_i - \mathbf{r}_j|; i, j = 1, 2, 3$ form the side of the triangle.

Usually pair counting is done in order to compute the correlation function. Higher order correlations are often estimated by their volume averages, the irreducible moments (cumulants) of counts in cells μ_N . The volume average of the correlation function $\bar{\xi}(r)$ is interpreted as the excess number of neighbours within a distance r of a given point.

$$\bar{\xi}(r) = \frac{3}{r^3} \int_0^r y^2 \xi(y) dy = 3 \int_0^\infty d \ln k \Delta^2(k) \left(\frac{\sin(kr) - kr \cos(kr)}{k^3 r^3} \right) \quad (1.56)$$

1.3.2 Mass variance

The next statistical indicator we consider is the root mean square (rms) fluctuation in mass at a scale r , $\sigma^2(r)$. This is a direct measure of fluctuations at the given scale r and unlike

¹Note however that unlike $\delta(\mathbf{r})$ which is a local quantity $\xi(r)$ is a statistical quantity

ξ and $\bar{\xi}$ it is positive definite by definition. It is defined as:

$$\sigma^2(r) = \frac{\langle(M - \langle M \rangle)^2\rangle}{\langle M \rangle^2} = \frac{\langle\delta M^2\rangle}{\langle M \rangle^2} = \frac{1}{2\pi^2} \int dk k^2 P(k) |W(k, r)|^2 \quad (1.57)$$

where $M \equiv V_W \rho$. V_W is the *effective volume* of the smoothing function W and for the spherical top hat smoothing function $V_W = 4\pi r^3/3$. For a spherical-top hat window $W(k, r)$ is given by

$$W(k, r) = 3 \left(\frac{\sin kr - kr \cos kr}{k^3 r^3} \right) \quad (1.58)$$

and in real space

$$W(|x - x'|, r) = \begin{cases} \frac{3}{4\pi r^3} & |x - x'| < r \\ 0 & \text{Otherwise} \end{cases} \quad (1.59)$$

It is more useful to express $\sigma^2(r)$ in the familiar form

$$\sigma^2(r) = \int \left(\frac{k^3 P(k)}{2\pi^2} \right) |W(k, r)|^2 d\ln k = \int \Delta^2(k) |W(k, r)|^2 d\ln k \quad (1.60)$$

For a power law model $P(k) \propto k^n$, we obtain;

$$\sigma^2(r) \propto r^{-(n+3)} \quad \text{and} \quad \sigma^2(M) \propto M^{-(n+3)/3} \quad (1.61)$$

or

$$\sigma^2(r) = \left(\frac{r}{r_{nl}} \right)^{-(n+3)} \quad \text{and} \quad \sigma^2(M) = \left(\frac{M}{M_{nl}} \right)^{-(n+3)/3} \quad (1.62)$$

Where the scale of nonlinearity r_{nl} is identified with the scale at which mass variance σ^2 becomes unity. Note that $\xi(r)$, $\bar{\xi}(r)$, $\sigma^2(r)$, eqs. 1.52, 1.56, 1.60 are similar quantities with a change only in the smoothing function. Therefore the scaling relations holds even for ξ and $\bar{\xi}$

1.3.3 The radial pair-velocity

The final statistical indicator that is of interest to us is the dimensionless radial pair velocity h_{pair} defined as:

$$h_{pair} = -\frac{\langle \mathbf{v}_p(\mathbf{r}, a) \cdot \mathbf{r} \rangle}{H r^2} \quad (1.63)$$

Where $\mathbf{v}_p(\mathbf{r}, a)$ is the relative velocity of pairs of objects separated by \mathbf{r} at epoch a . h_{pair} is the ratio of radial component of this velocity and the Hubble flow both evaluated at \mathbf{r} , hence it is a dimensionless quantity. In the linear regime $\bar{\xi} \ll 1$, $h = (2/3)\bar{\xi}$, in an Einstein deSitter Universe, (Peebles, 1980). In the non-linear regime if we can ignore the effect of mergers then we expect objects to be in virial equilibrium, hence these velocities should be equal and opposite in order to have a stable system (*stable clustering limit*). We expect $h \rightarrow 1$ as $\bar{\xi} \rightarrow \infty$.

1.4 Non-linear gravitational clustering

We have seen that modes of density perturbations grow independently in the linear regimes, eq. 1.41. With time the modes couple to each other and a simple analytical solution is not possible and one has to resort to numerical methods, namely N -body simulations. Nevertheless it is important to have some insight into the process of structure formation with the use of approximate analytical models. Here we outline some of them.

1.4.1 The Zeldovich approximation

The source term in Poisson's equation, eq. 1.46, $\delta/b(t)$ is constant in the linear regime, implying that the generalised force \mathbf{g} is constant in the linear regime. It can also be shown that the velocity \mathbf{u} is constant in the linear regime, which means that the generalised acceleration is zero

$$\frac{d\mathbf{u}}{db} = 0 \quad (1.64)$$

Hence

$$\mathbf{u}(\mathbf{x}, b) = \mathbf{u}(\mathbf{x}) = \mathbf{g}(\mathbf{x}, b) = \mathbf{g}(\mathbf{x}) \quad (1.65)$$

This is valid only in the linear regime, $\delta \ll 1$. However one can extrapolate this equation to a regime which is slightly non-linear.

In the Zeldovich approximation velocities are constant in Lagrangian space, the coordinate system attached to particles. Thus the velocity of each particle is constant and

equals its initial velocity

$$\mathbf{u}(\mathbf{x}, b) = \mathbf{u}(\mathbf{q}) = \mathbf{g}(\mathbf{q}) \quad (1.66)$$

where \mathbf{q} is the Lagrangian position of the particle, same as its initial position and \mathbf{x} is its Eulerian position. The particle trajectories evolve as

$$\mathbf{x} = \mathbf{q} + b\mathbf{g}(\mathbf{q}) \quad (1.67)$$

Particles move with a uniform velocity that is determined by its initial potential. The Zeldovich approximation is a one-step mapping between initial and final conditions. Approximate constancy of velocities results in the linear regime wherein timescales of expansion and collapse cancel each other. It is particularly useful in setting up initial conditions in N -body simulations where one evolves a linear density field to a weakly non-linear regime. Particles are displaced from a uniform grid according to the eq. 1.67. However one needs to generate the initial potential ψ in order to compute $\mathbf{g} = -\nabla\psi$. The power spectrum of density fluctuations relates it to the power spectrum of the potential through the Poisson equation.

$$P_\psi(k, a) = \frac{P_\delta(k, a)}{a^2 k^4} = \frac{P_\delta^{lin}(k, a=1)}{k^4} \quad (1.68)$$

Here $P_\delta^{lin}(k, a=1)$ is the linearly extrapolated power spectrum of the initial density fluctuation. Care must also be taken in choosing the size of the first step, since the Zeldovich approximation breaks down at shell crossing. The initial displacement should be such that shell crossing does not even in the most overdense region in the realization.

1.4.2 Spherical collapse

The spherical collapse model is one of the simplest models which qualitatively describes how a galaxy or a cluster collapses and forms by breaking away from the general expansion of the Universe. It is not an exact model but nevertheless serves as a reference for generic collapse. The densities of the overdense region and background should be evolved using Friedmann equations, however in what follows we solve this problem using Newtonian mechanics which also gives the same results.

If we consider that the total mass enclosed within a spherical shell is M (which does not change during collapse) and the radius at time t is $R(t)$ then

$$\ddot{R}(t) = -\frac{GM}{R^2(t)} \quad (1.69)$$

and so

$$\frac{\dot{R}^2(t)}{2} = \frac{GM}{R} + E \quad (1.70)$$

Here E is an integration constant which can be identified with the total energy of the shell. If we consider that the energy of the system is negative, as is required for formation of a bound system, then the above equation can be solved with the following parametric solution

$$R(\theta) = \frac{GM}{2|E|} (1 - \cos \theta) = A (1 - \cos \theta) = \frac{R_{max}}{2} (1 - \cos \theta) \quad (1.71)$$

$$t(\theta) = \frac{GM}{(2|E|)^{3/2}} (\theta - \sin \theta) = B (\theta - \sin \theta) = \frac{t_{max}}{\pi} (\theta - \sin \theta) \quad (1.72)$$

where $A^2 = 2|E|B^2$, $R_{max} = 2A$, $t_{max} = B\pi$.

Eq. 1.71 shows that due to gravitational attraction, the expansion rate of the over-dense regions slows down in comparison to the background. After reaching a maximum size R_{max} (called the turn-around radius) at time t_{max} , the overdense region stops expanding and begins to collapse. At turnaround:

$$E = -\frac{GM}{R_{max}} \Rightarrow R_{max} = \frac{GM}{|E|} = 2A \quad (1.73)$$

However we expect the overdense region to virialize instead of collapsing to $R = 0$. At virialization:

$$E = \frac{U}{2} = \frac{GM}{2R_{vir}} \Rightarrow R_{vir} = \frac{GM}{2|E|} = \frac{R_{max}}{2} \quad (1.74)$$

From equation (1.71) we can write an expression for the density of the overdense region

$$\rho(t) = \frac{3M}{4\pi R^3(t)} = \frac{3M}{4\pi A^3(1 - \cos \theta)^3} \quad (1.75)$$

If we model the expansion of background by the Einstein-de Sitter model then the average density $\bar{\rho}(t)$ evolves as

$$\bar{\rho}(t) = \frac{1}{6\pi G t^2} \quad (1.76)$$

From equation (1.75) and equation (1.76) we can write an expression for the nonlinear density contrast

$$1 + \delta(t) = \frac{\rho(t)}{\bar{\rho}(t)} = \frac{9}{2} \left(\frac{GMB^2}{A^3} \right) \frac{[\theta(t) - \sin \theta(t)]^2}{[1 - \cos \theta(t)]^3}$$

Using the fact that $A^2 = 2|E|B^2$, and $|E| = GM/2A$, we get

$$1 + \delta = \frac{9}{2} \frac{(\theta - \sin \theta)^2}{(1 - \cos \theta)^3} \quad (1.77)$$

In order to compare the nonlinear and linear density contrast we expand the above equation around $\theta = 0$

$$1 + \delta = \frac{9}{2} \frac{(\theta - \sin \theta)^2}{(1 - \cos \theta)^3} = \frac{9}{2} \frac{\left[\theta - \left(\theta - \frac{\theta^3}{6} + \frac{\theta^5}{120} - \dots \right) \right]^2}{\left[1 - \left(1 - \frac{\theta^2}{2} + \frac{\theta^4}{24} \right) \right]^3} \approx 1 + \frac{3}{20} \theta^2 \quad (1.78)$$

and so

$$\delta_l(\theta) = \frac{3}{20} \theta^2 \quad (1.79)$$

and in the linear limit

$$\theta(t) \approx \left(\frac{6\pi t}{t_{max}} \right)^{1/3} \quad \text{and} \quad R(t) \approx \frac{R_{max}}{4} \theta^2$$

and so

$$\delta_l(t) = \left(\frac{6\pi t}{t_{max}} \right)^{2/3} \quad \text{or} \quad \delta_l(t) \propto a(t) \quad (1.80)$$

Note that this is exactly the same result as is given by linear perturbation theory. From eq. (1.80) and (1.77) we can easily compute the linear and nonlinear density contrast respectively at the turn-around i.e., $\theta = \pi, t = t_{max}$

$$\delta_{turn} = \begin{cases} \frac{3(6\pi)^{2/3}}{20} \approx 1.06 & \text{linear} \\ \frac{9\pi^2}{16} - 1 \approx 4.6 & \text{nonlinear} \end{cases} \quad (1.81)$$

If we consider that the nonlinear density contrast at turn-around and virialization are δ_{turn} and δ_{vir} respectively and use the fact that $\rho \propto 1/R^3$, and $\bar{\rho} \propto 1/t^2$, then

$$\frac{1 + \delta_{vir}}{1 + \delta_{turn}} = \frac{\rho_{vir}/\bar{\rho}_{vir}}{\rho_{turn}/\bar{\rho}_{turn}} = \left(\frac{R_{max}}{R_{vir}} \right)^3 \left(\frac{t_{vir}}{t_{max}} \right)^2 \quad (1.82)$$

and so at the virialization i.e., $t_{vir} = 2t_{max}$, we get

$$\delta_{vir} = \begin{cases} \frac{3(12\pi)^{2/3}}{20} \approx 1.68 & \text{linear} \\ 32 \left[\frac{9\pi^2}{16} \right] - 1 \approx 176 & \text{nonlinear} \end{cases} \quad (1.83)$$

1.4.3 The Press-Schechter formalism

The Press-Schechter formalism (Press & Schechter, 1974) predicts the number density of objects of mass M in the Universe. It identifies peaks in the linear density field that collapse at a later time. The number density is estimated by identifying the fraction of mass $F(M)$ in collapsed objects at any time t , which have mass greater than M , with the fraction of the initial volume for which the density contrast is greater than a critical value i.e., $\delta > \delta_c$. Here M is the mass enclosed in a spherical volume of radius r and is related to the average density field $\bar{\rho}$ through $M = \frac{4}{3}\pi r^3 \bar{\rho}$. The critical density contrast δ_c is identified with the linearly extrapolated density contrast at time t , needed for virialization in spherical collapse model i.e., $\delta_c = 1.68$, for an Einstein-de Sitter model. The main results of the Press-Schechter formalism can be derived in the following way.

If we consider that the initial density field is a Gaussian random field, and smooth it at a scale r , using a spherical-top hat window function $W(x, r)$, then the probability of finding a spherical region with density contrast in range $[\delta, \delta + d\delta]$ is given by

$$P(\delta, r) = \frac{1}{\sqrt{2\pi\sigma(r)}} \exp\left(-\frac{\delta^2}{2\sigma^2(r)}\right) \quad (1.84)$$

where

$$\sigma^2(r) = \int \frac{dk}{k} \frac{k^3 P(k)}{2\pi^2} 9 \left(\frac{\sin kr - kr \cos kr}{(kr)^3} \right)^2 \quad (1.85)$$

In the Press-Schechter formalism the fraction of mass $F(M)$ in the collapsed objects with mass greater than M is identified with the fraction of the initial volume for which $\delta > \delta_c$.

$$F(M) = \int_{\delta_c}^{\infty} P(\delta, r) d\delta = \int_{\delta_c}^{\infty} \frac{1}{\sqrt{2\pi\sigma(r)}} \exp\left(-\frac{\delta^2}{2\sigma^2(r)}\right) d\delta = \frac{1}{2} \operatorname{Erfc}\left[\frac{\delta_c}{\sigma\sqrt{2}}\right] \quad (1.86)$$

Here $\operatorname{Erfc}(x)$ is the complimentary error function.

This formalism does not take into account the mass in underdense regions, which also collapses eventually. It underestimates the mass function $F(M)$ by a factor of two which is corrected by multiplying eq. 1.86 by two.

$$F(M) = \frac{2}{\sqrt{\pi}} \int_{\delta_c/\sigma\sqrt{2}}^{\infty} e^{-x^2} dx = \text{Erfc} \left[\frac{\delta_c}{\sigma\sqrt{2}} \right] = \text{Erfc} \left(\frac{\nu}{\sqrt{2}} \right) \quad (1.87)$$

where $\nu = \delta_c/\sigma$. However the excursion set formalism for mass functions (Bond et al., 1991) remedies this problem naturally. On the basis of eq. 1.87 we can also compute the fraction of mass $g(M)dM$, called the multiplicity function, in the objects which have mass in the range $[M, M + dM]$.

$$g(M)dM = \frac{\partial F(M)}{\partial M} dM = \sqrt{\frac{2}{\pi}} \left(\frac{\delta_c}{\sigma(M)} \right) \left(\frac{-1}{\sigma(M)} \frac{\partial \sigma(M)}{\partial M} \right) \exp \left(-\frac{\delta_c^2}{2\sigma^2(M)} \right) dM \quad (1.88)$$

or

$$g(M)dM = \sqrt{\frac{2}{\pi}} \left| \frac{d\ln\sigma}{dM} \right| \nu \exp(-\nu^2/2) dM \quad (1.89)$$

and the comoving number density of objects $N(M)dM^2$ in the mass range $[M, M + dM]$ is

$$N(M)dM = \frac{\bar{\rho}}{M} \times g(M)dM = \sqrt{\frac{2}{\pi}} \frac{\bar{\rho}}{M^2} \left| \frac{d\ln\sigma}{d\ln M} \right| \nu \exp(-\nu^2/2) dM \quad (1.90)$$

We will later (chapter 4) refer to the quantity $f(\nu)$ defined as:

$$g(M) = f(\nu) \left| \frac{d\ln\sigma}{dM} \right| \quad (1.91)$$

as the mass function. For the spherical collapse model

$$f(\nu) = \sqrt{\frac{2}{\pi}} \nu \exp(-\nu^2/2) \quad (1.92)$$

For the ellipsoidal collapse model (Sheth & Tormen, 1999; Sheth, Mo, & Tormen, 2001) the massfn $f(\nu)$ is given by

$$f(\nu) = A \sqrt{\frac{2q}{\pi}} [1 + (q\nu^2)^{-p}] \nu \exp(-q\nu^2/2). \quad (1.93)$$

²sometimes authors refer to $N(M)$ as $\frac{dn}{dM}$. We will use them interchangeably.

where A, p, q are constants. This is also known as the Sheth-Tormen mass function.

For a power law model i.e., $P(k) \propto k^n$

$$\sigma^2(M) = \left(\frac{M}{M_{nl}} \right)^{-(n+3)/3} \Rightarrow \left| \frac{d\ln\sigma}{d\ln M} \right| = \frac{(n+3)}{6} \quad (1.94)$$

and so for Press-Schechter theory

$$N_{PS}(M)dM = \frac{1}{\sqrt{2\pi}} \frac{\bar{\rho}}{M^2} \frac{(n+3)}{3} \left(\frac{M}{M_{nl}} \right)^{\frac{(n+3)}{6}} \exp \left[-\frac{1}{2} \left(\frac{M}{M_{nl}} \right)^{(n+3)/3} \right] dM \quad (1.95)$$

With the the Sheth-Tormen mass function we obtain:

$$\begin{aligned} N_{ST}(M)dM &= A \sqrt{\frac{q}{2\pi}} \frac{\bar{\rho}}{M^2} \frac{(n+3)}{3} \left[1 + \left(q \left(\frac{M}{M_{nl}} \right)^{\frac{(n+3)}{3}} \right)^{-p} \right] \\ &\times \left(\frac{M}{M_{nl}} \right)^{\frac{(n+3)}{6}} \exp \left[-\frac{1}{2} \left(\frac{M}{M_{nl}} \right)^{(n+3)/3} \right] dM \end{aligned} \quad (1.96)$$

In this chapter we have described the basic framework to study non-linear gravitational clustering in an expanding Universe. We have seen that in the linear regime it is possible to solve the evolution of density perturbations analytically because modes evolve independently. Analytical models such as the Zeldovich approximation can extend this to the quasi-linear regime. We have also seen how a simple model like that of Press-Schechter theory predicts the abundance of halos in the non-linear regime. However when modes of the density field start to couple with each other, eq. 1.41, it is impossible to solve for the evolution of density perturbations and numerical techniques such as N -body simulations have to be employed. N -body methods do not give the insight which analytical methods provide but they give an accurate evolution of the system which can, among the myriads of other applications, be used to test the limits of analytical predictions such the Zeldovich approximation and the Press-Schechter theory described here.

In the following two chapters our study will be aimed at improving on an existing N -body method, and developing a new N -body code.

Chapter 2

A Modified TreePM Code

2.1 Cosmological N-body simulations

In the last chapter we described the equations that describe the evolution of density perturbations in an expanding Universe. Once density contrast at relevant scales becomes comparable to unity, perturbations become non-linear and coupling with perturbations at other scales cannot be ignored. The equation for evolution of density perturbations cannot be solved for generic initial conditions in this regime. N-Body simulations (e.g., see (Efstathiou et al., 1985; Bertschinger, 1998; Bagla & Padmanabhan, 1997; Bagla, 2005)) are often used to study the evolution in this regime. Alternative approaches can be used if one requires only a limited amount of information and in such a case either quasi-linear approximation schemes (Bernardeau et al., 2002; Zel'Dovich, 1970; Gurbatov, Saichev, & Shandarin, 1989; Matarrese et al., 1992; Brainerd, Scherrer, & Villumsen, 1993; Bagla & Padmanabhan, 1994; Sahni & Coles, 1995; Hui & Bertschinger, 1996) or scaling relations (Davis & Peebles, 1977; Hamilton et al., 1991; Jain, Mo, & White, 1995; Kanekar, 2000; Ma, 1998; Nityananda & Padmanabhan, 1994; Padmanabhan et al., 1996; Peacock & Dodds, 1994; Padmanabhan, 1996; Peacock & Dodds, 1996; Smith et al., 2003) suffice. However, even the approximation schemes and scaling relations must be compared with simulations before these can be used with confidence.

Last three decades have seen a rapid development of techniques and computing power

for cosmological simulations and the results of these simulations have provided valuable insight into the study of structure formation. The state of the art simulations used less than 10^5 particles two decades ago (Efstathiou et al., 1988) and if the improvement had been due only to computing power then the largest simulation possible today should done with have been around 10^9 particles, whereas the largest simulations done till date used more than 10^{10} particles (Springel et al., 2005). Evidently, development of new methods and optimisations has also played a significant role in the evolution of simulation studies (Efstathiou et al., 1985; Barnes & Hut, 1986; Greengard & Rokhlin, 1987; Bouchet & Hernquist, 1988; Jernigan & Porter, 1989; Hernquist, 1990; Makino, 1990, 1991; Hernquist, Bouchet, & Suto, 1991; Couchman, 1991; Ebisuzaki et al., 1993; Theuns, 1994; Brieu, Summers, & Ostriker, 1995; Suisalu & Saar, 1995; Xu, 1995; Dubinski, 1996; Kravtsov, Klypin, & Khokhlov, 1997; Macfarland et al., 1998; Bode, Ostriker, & Xu, 2000; Brieu & Evrard, 2000; Dehnen, 2000; Knebe, Green, & Binney, 2001; Springel, Yoshida, & White, 2001; Kawai & Makino, 2001; Makino, 2002; Dehnen, 2002; Bagla, 2002; Bagla & Ray, 2003; Makino et al., 2003; Bode & Ostriker, 2003; Ray & Bagla, 2004; Dubinski et al., 2004; Makino, 2004; Springel, 2005; Merz, Pen, & Trac, 2005; Yoshikawa & Fukushige, 2005; Wadsley, Stadel, & Quinn, 2004; Thacker & Couchman, 2006) Along the way, code developers have also successfully met the challenge posed by the emergence of distributed parallel programming.

In this chapter, we discuss the performance characteristics of an optimisation for tree codes suggested by Barnes (1990). We do this in the context of the TreePM method (Bagla, 2002; Bagla & Ray, 2003) where the tree method is used for computing the short range force. The TreePM method brings in an additional scale into the problem, i.e., the scale up to which the short range force is computed and this leads to non-trivial variations in error in force.

This chapter is organised as follows: we introduce the TreePM method in §2.2, and discuss the optimisation scheme in §2.3. Performance of the optimisation scheme is discussed in §2.4, and we discuss combining this with individual time steps for particles in §2.5. We end with a discussion in §2.6.

2.2 The TreePM Algorithm

The TreePM (Bagla, 2002; Bagla & Ray, 2003) is a hybrid N-Body method which combines the BH-Tree method (Barnes & Hut, 1986) with the PM method (Bagla & Padmanabhan, 1997; Klypin & Shandarin, 1983; Miller, 1983; Bouchet & Kandrup, 1985; Bouchet, Adam, & Pellat, 1985; Hockney & Eastwood, 1988; Merz, Pen, & Trac, 2005).

The TreePM method explicitly breaks the potential into a short-range and a long-range component at a scale r_s . The PM method is used to calculate the long-range force and the short-range force is computed using the BH Tree method. Use of the BH Tree for short-range force calculation enhances the force resolution as compared to the PM method.

The gravitational force is divided into a long range and a short range part using partitioning of unity in the Poisson equation.

$$\begin{aligned}\phi_k &= -\frac{4\pi G \rho_k}{k^2} \\ &= -\frac{4\pi G \rho_k}{k^2} \exp(-k^2 r_s^2) - \frac{4\pi G \rho_k}{k^2} [1 - \exp(-k^2 r_s^2)] \\ &= \phi_k^{lr} + \phi_k^{sr} \\ \phi_k^{lr} &= -\frac{4\pi G \rho_k}{k^2} \exp(-k^2 r_s^2) \quad (2.1) \\ \phi_k^{sr} &= -\frac{4\pi G \rho_k}{k^2} [1 - \exp(-k^2 r_s^2)] \quad (2.2)\end{aligned}$$

Here ϕ_k^{sr} and ϕ_k^{lr} are the short-range and long-range potentials in Fourier space. ρ is the density, G is the gravitational coupling constant and r_s is the scale at which the splitting of the potential is done. The long-range force is solved in Fourier space with the PM method and the short-range force is solved in real space with the Tree method. The short range force in real space is:

$$\mathbf{F}^{sr}(\mathbf{r}) = -\frac{GM\mathbf{r}}{r^3} \left[\operatorname{erfc}\left(\frac{r}{2r_s}\right) + \frac{r}{r_s\sqrt{\pi}} \exp\left(-\frac{r^2}{4r_s^2}\right) \right] \quad (2.3)$$

Here erfc is the complementary error function.

The short range force is below 1% of the total force at $r \geq 5r_s$, therefore it is computed within a sphere of radius $r_{cut} \simeq 5r_s$ using the BH tree method. The tree structure is built

out of cells and particles. Cells may contain smaller cells (subcells) within them. Subcells can have even smaller cells within them, or they can contain a particle. In three dimensions, each cubic cell is divided into eight cubic subcells. Cells, as structures, have attributes like total mass, location of centre of mass and pointers to subcells. Particles, on the other hand have the usual attributes: position, velocity and mass.

Force on a particle is computed by adding contribution of other particles or of cells. A cell that is sufficiently far away can be considered as a single entity and we can add the force due to the total mass contained in the cell from its centre of mass. If the cell is not sufficiently far away then we must consider its constituents, subcells and particles. Whether a cell can be accepted as a single entity for force calculation is decided by the cell acceptance criterion (CAC). We compute the ratio of the size of the cell L_{cell} and the distance r from the particle in question to its centre of mass and compare it with a threshold value

$$\theta = \frac{L_{cell}}{r} \leq \theta_c \quad (2.4)$$

The error in force increases with θ_c . A poor choice of θ_c can lead to significant errors (Salmon & Warren, 1994). Many different approaches have been tried for the CAC in order to minimize error as well as CPU time usage (Salmon & Warren, 1994; Springel, Yoshida, & White, 2001). The tree code gains over direct summation as the number of contributions to the force is much smaller than the number of particles.

The TreePM method is characterised therefore by three parameters, r_s, r_{cut} and θ_c . For a discussion on the optimum choice of these parameters the reader is referred to (Bagla & Ray, 2003).

2.2.1 Moving particles

The EOM in comoving coordinates eq. 1.38 has a velocity dependant term proportional to the Hubble parameter, $H(t) = \dot{a}(t)/a(t)$. Numerical integration of such equations can be tricky and one has to generally employ an iterative procedure. We use a simple change of the time variable to transform the EOM into a form which does not contain this velocity

dependant term. The negative time (Klypin & Shandarin, 1983) variable θ defined as:

$$d\theta = \frac{H_0 dt}{a^2} \quad (2.5)$$

transforms the EOM 1.38

$$\begin{aligned} \ddot{\tilde{x}} &= -\frac{3}{2}\Omega_{nr}a\nabla_x\chi \\ \nabla_x^2\chi &= \delta \end{aligned} \quad (2.6)$$

Here $\ddot{\tilde{x}} \equiv \frac{d^2x}{d\theta^2}$ and $\phi = \frac{3}{2}\frac{\Omega_{nr}H_0^2}{a}\chi$. This form is familiar and we employ a 2nd order leap-frog integrator to integrate the EOM.

2.3 The scheme of groups

We first describe an optimization scheme due to (Barnes, 1990), given in the paper with a curious title *A modified tree code: Don't laugh, it runs*. This scheme can be used with any N-body algorithm that uses tree data structures to compute forces. The origin of the optimisation is in the realisation that the tree walk used for computing forces is computationally the most expensive component of a tree code. The idea is to have a common interaction list for a *group* of particles that is sufficiently small. Given that we are working with a tree code, it is natural to identify a cell in the tree structure as a group. One can then add the contribution of particles within the group using direct pair summation. The cell acceptance criterion (CAC) for the tree walk needs to be modified in order to take the finite size of the group into account. In our implementation of the TreePM method, we modified the standard CAC in the following manner:

$$L_{cell} \leq (r - r_m) \theta_c \quad (2.7)$$

where r_m is the distance between the centre of mass of the group, and the group member that is farthest from the centre of mass. This is calculated once before the force calculation and does not add much in terms of overhead.

The modified CAC can be thought of as the standard CAC with a distance dependent θ_c , with the value of θ_c decreasing at small r . As we require a larger number of operations

for smaller θ_c , each tree walk with the modified CAC is expected to require more CPU time than a tree walk with the standard CAC. However, as we do a tree walk for a group of particles in one go, CPU time is saved as the time taken for tree walk per particle comes down.

There is an overhead as there is a pair-wise force calculation within the group. The cost of this overhead increases as the square of the number of particles in the group. In order to keep the overhead small, one would like the group to be sufficiently small compared to the size of the N-Body simulation and hence a maximum size c_{max} and an upper bound on the number of particles in the group $n_{p_{max}}$ is used. An upper limit on the size of the group is pertinent because of the indirect effect through the change in the CAC. The effect of the additional parameter c_{max} with the modified CAC will be seen when we discuss errors in section 2.4. Our implementation of the modified method by using a different definition of groups, with the additional parameter c_{max} and the modified CAC (eq. 2.7) ensure that the short-range force is extremely accurate. This is different from previous implementations (Barnes, 1990; Makino, 1991; Yoshikawa & Fukushige, 2005; Wadsley, Stadel, & Quinn, 2004) where the group scheme was parametrized by just one parameter $n_{p_{max}}$ and the standard CAC (eq. 2.4) used for tree traversal. We note in passing that the modified CAC is crucial in order to limit errors. Indeed, we find that working with the standard CAC leads to errors in short range force *that are orders of magnitude larger*.

2.3.1 Estimating Speedup

We model the modified Tree/TreePM method with the aim of estimating the speedup that can be achieved. If N is the total number of particles, n_p the typical number of particles in a group and n_g the number of groups then clearly we expect $n_g \times n_p = N$. The total time required for force calculation is a sum of the time taken up by the tree walk and the time taken up by pair wise calculation within the group. Actual calculation of the force, once the interaction list has been prepared takes very little time and can be ignored in this estimate, as can the time taken to construct the tree structure. The time taken is:

$$T_g = \alpha n_g \ln N + \beta n_g n_p^2 = \alpha \frac{N}{n_p} \ln N + \beta N n_p \quad (2.8)$$

Here we have assumed that the time taken per tree walk scales as $\mathcal{O}(\ln N)$ even with the modified CAC¹. The time taken is smallest when

$$n_p = \left(\frac{\alpha \ln N}{\beta} \right)^{1/2} ; \quad T_{g_{min}} = 2\beta N n_p = 2\alpha \frac{N}{n_p} \ln N \quad (2.9)$$

Thus the optimum number of particles in the group scales weakly with the total number of particles. In the optimum situation, we expect the tree walk and the pair wise components to take the same amount of CPU time.

For comparison, the time taken for force calculation in the standard TreePM is:

$$T = \alpha N \ln N \quad (2.10)$$

and we make the simplifying assumption that α is same for the two cases. The expected speed up is then given by:

$$\frac{T}{T_{g_{min}}} = \frac{1}{2} \left(\frac{\alpha \ln N}{\beta} \right)^{1/2} . \quad (2.11)$$

The speedup for the optimum configuration scales in the same manner as the optimal number of particles per group. A more detailed analysis of this type can be found in Makino (1991).

The calculation we have presented above is approximate and ignores several factors, some of these have already been highlighted above. There are other subtleties like the role played by the finite range r_{cut} over which the short range force is calculated. The size of a group (c_{max}) cannot be varied continuously, and hence n_p is also restricted to a range of values. Further, the number of operations do not translate directly into CPU time as some calculations make optimal use of the capabilities of a CPU while others do not. For example, the pair wise calculation is likely to fare better on processors with a deep pipeline for execution whereas tree walk can not exploit this feature. The finite bandwidth of the CPU-memory connection also has an impact on the scaling with N for large N . In the following section, we discuss the implementation of the modified TreePM method and the timing of the code with different values of parameters.

¹This is an approximation as we expect the tree walk to depend on c_{max} , $n_{p_{max}}$ and θ_c as well. The finite size of groups should lead to deviations from the $\mathcal{O}(\ln N)$ variation and the deviation should scale as the ratio of the volume of the group and the volume of the simulation box. As this ratio becomes smaller for large simulation boxes, we feel that the approximation we have made is well motivated.

2.4 A Modified TreePM Algorithm

Tests of the TreePM method have shown that 95–98% of the time goes into the short-range force calculation. Keeping this in mind the scheme of groups was introduced to optimize the short-range force calculation in terms of speed. A welcome feature is more accurate force computation. Since the optimum set of TreePM parameters have been discussed in (Bagla & Ray, 2003), we now look for the optimum choice of the additional parameters, c_{max} and $n_{p_{max}}$, which describe the Modified TreePM algorithm. The analysis that follows is divided into two parts. First we look at the optimum values of c_{max} and $n_{p_{max}}$ which minimise the time for short range force computation. Second, we study errors in total and short range force with this new scheme.

2.4.1 Optimum Parameters of The Modified TreePM Algorithm

We choose $r_s = 1$, $r_{cut} = 5.2r_s$ and $\theta_c = 0.5$ for the discussion that follows. With this choice the error in force for 99% of the particles is less than a few percent (Bagla & Ray, 2003). We present analysis of performance of the modified TreePM for two different particle distributions taken from an N –body simulation, with $N = N_{box}^3 = 200^3$.

- An unclustered distribution that corresponds to the initial conditions of an N –body simulation.
- A clustered distribution taken again from the same N –body simulation. The scale of non-linearity for the clustered distribution is 8 grid lengths.

We have verified that the nature of results does not change significantly for simulations with the number of particles ranging from 32^3 to 256^3 .

In figure 2.1 we show the time taken for computing the the short-range force (solid line) and determine the values of $(c_{max}, n_{p_{max}})$ for which this timing is a minimum. Two leading contributions to the calculation of short range force are shown separately:

- Intra-group particle-particle contribution (dashed line).
- Time taken for tree-walk and the related force calculation (dot-dashed line).

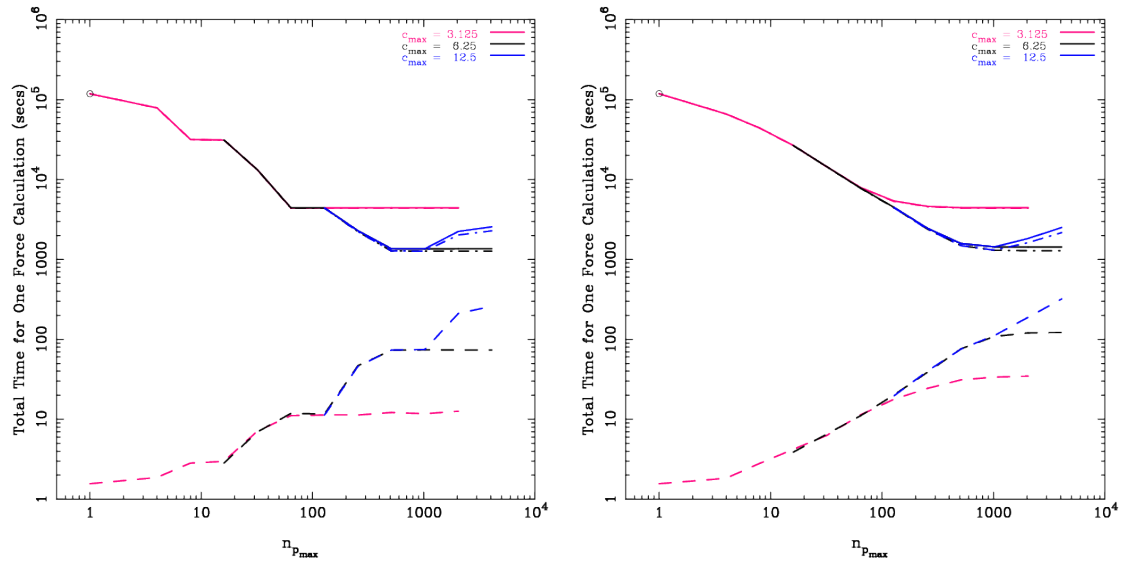


Figure 2.1: Time taken for computation of the short term force in the Modified TreePM method for an unclustered (left panel) and a clustered (right panel) distribution. Solid lines represent the time taken by a complete short-range force calculation. Dashed lines are the contribution to the force due to pairs within a group, the intra-group contribution. Dot-Dashed lines are the contributions to force due to tree walk. Purple, black and blue lines are for $c_{max} = 3.125, 6.25, 12.5$ respectively

Given that a group is a cell with maximum width

$$c_{max} = \frac{N_{box}}{2^m}, \quad (m \text{ is an integer}), \quad (2.12)$$

c_{max} can take discrete values. We choose to restrict up to $c_{max} \sim 2r_{cut}$ as for larger cells, the dominant contribution to force on a given particle arises from the intra-group particle-particle interaction and the time taken for this is a sensitive function of the amplitude of clustering.

The time taken for computing the short range force in both, unclustered (left panel) as well as clustered (right panel), distributions is qualitatively described by our model (see eq. 2.8). The pairwise force increases linearly with $n_{p_{max}}$, the maximum number of particles in a group, and, scales as n_p , the average number of particles in a group. The time taken for tree-walk decreases as $n_{p_{max}}^{-0.65}$, reaches a minimum and then increases with $n_{p_{max}}$ (blue line) for the largest c_{max} used here. For other values of c_{max} we see the timing levelling off near the minimum. The scaling $n_{p_{max}}^{-0.65}$ is different from $1/n_p$ we used in the analytical model and the reason for this is likely to be in the approximations we used. We find that the scaling approaches $1/n_{p_{max}}$ as we consider simulations with a larger number of particles. One crucial reason for different scaling is the modified CAC we use here. This effectively leads to a smaller θ_c for cells closer to the group and the number of such cells increases with c_{max} .

In both cases the total time is still dominated by the tree-walk. The plateaus in the plots often indicate that the number of particles in a group of maximum size c_{max} have saturated. At initial times where the fluctuations are small there is also a lower bound on the number of particles contained in a group. In the clustered distribution there is no such lower bound but an upper bound, larger than the corresponding upper bound in case of the unclustered distribution, exists and is dictated by the amplitude of clustering in the distribution of particles.

From figure 2.1 we see that the optimum values of $(c_{max}, n_{p_{max}}) = (12.5, 1024) \& (6.25, \geq 1024)$ given by the minima of the solid blue line and the plateau of the solid black line respectively. In the latter case the time taken does not change for $n_{p_{max}} \geq 1024$ and we consider this to be a useful feature that makes $c_{max} = 6.25$ a better choice as fine tuning of $n_{p_{max}}$ is not required. For the optimum $(c_{max}, n_{p_{max}})$ one can see that

Table 2.1: The following table lists the optimum values of $(c_{max}, n_{p_{max}})$ for simulations of various sizes but having the same TreePM parameters: $r_s = 1$, $r_{cut} = 5.2r_s$ $\theta_c = 0.5$.

$N_{box} = N^{1/3}$	c_{max}^{opt}	$n_{p_{max}}^{opt}$
64	4.0	≥ 1024
128	4.0	≥ 1024
160	5.0	≥ 1024
200	6.25	≥ 1000

force computation takes the same time for the clustered and the unclustered distributions. Table 2.1 lists optimum values for $(c_{max}, n_{p_{max}})$ for N-Body simulations with different number of particles. These numbers indicate that a good choice for c_{max} is one which is closest to r_{cut} , i.e. $c_{max} \sim r_{cut}$. The parameter $n_{p_{max}}$ can be taken to be $10^3 \leq n_{p_{max}}$ as we find little variation beyond this point.

One can get an estimate of the overheads for the group scheme by looking at the limit of $n_{p_{max}} \rightarrow 1$. Here we compare the performance of the TreePM with the modified code by plotting the time taken by the former as a large dot on the same panel where the time taken for the modified code is shown in the form of curves. The difference between these timings is around 0.1%.

The speedup for the optimal configuration of the modified TreePM, as compared with the base TreePM code is ~ 83 . This is a huge gain and has to do with better utilisation of the CPU cache. The speedup is less impressive for smaller simulations, and is larger for bigger simulations. This is shown in figure 2.2 where we plot the time taken for force calculation per particle per step as a function of the total number of particles in the simulation. This is shown for the TreePM as well as the modified TreePM codes. Performance on two different types of processors is shown here to demonstrate that the optimisation works equally well on these. One can see that the TreePM code becomes (CPU-Memory) bandwidth limited for simulations with more than 64^3 particles and the time taken increases more rapidly than $\mathcal{O}(\ln N)$. This does not happen in case of the

modified TreePM where the scaling is $\mathcal{O}(\ln N)$ throughout. There is a slight increase in time for the modified code at $N_{part} \sim 10^6$ which may be attributed to the finite size of the CPU cache but unlike the unmodified code the scaling of the code does not break down beyond this point. It is this difference that leads to impressive speedup for large simulations. For simulations with up to 64^3 particles we get a speedup by a factor of four.

2.4.2 Errors in Force

We now study errors in force for the modified TreePM force. Errors are calculated with respect to a reference force computed with very conservative values of TreePM parameters: $\theta_c = 0.01$, $r_s = 4.0$, $r_{cut} = 5.2r_s$. With these values the reference force is accurate to 0.1% (Bagla & Ray, 2003).

$$\epsilon = \frac{|\mathbf{F}_{ref} - \mathbf{F}|}{|\mathbf{F}_{ref}|} \quad (2.13)$$

Here ϵ , \mathbf{F}_{ref} , \mathbf{F} are the relative error, reference force and the typical force in a simulation. We calculate errors for two distributions of particles:

- A uniform (unclustered) distribution.
- A clustered distribution taken from an N -body simulation.

Both distributions have $N_{box}^3 = N = 128^3$ particles. The exercise we follow is similar to (Bagla & Ray, 2003) but now we wish to highlight the effect of groups on errors in force.

Figure 2.3 shows the distribution of errors for different values of θ_c . The results are shown for both the distributions being studied here: the unclustered distribution (left panels) and the clustered distribution (right panels). The top row is with $c_{max} = 2.0$ and the lower row is for $c_{max} = 4.0$. We used $r_s = 1.0$ and $r_{cut} = 5.2r_s$ for this figure. In the case of the unclustered distribution error decreases with θ_c but saturates at $\theta_c = 0.3$ and does not decrease as θ_c is decreased further. The situation is different for the clustered distribution where the errors are not sensitive to θ_c . This suggests that the errors are dominated by the long-range force. The unclustered distribution has larger errors than the clustered distribution. This is because the net force on each particle in the unclustered distribution is small, whereas force due to a cell with many particles is large and many

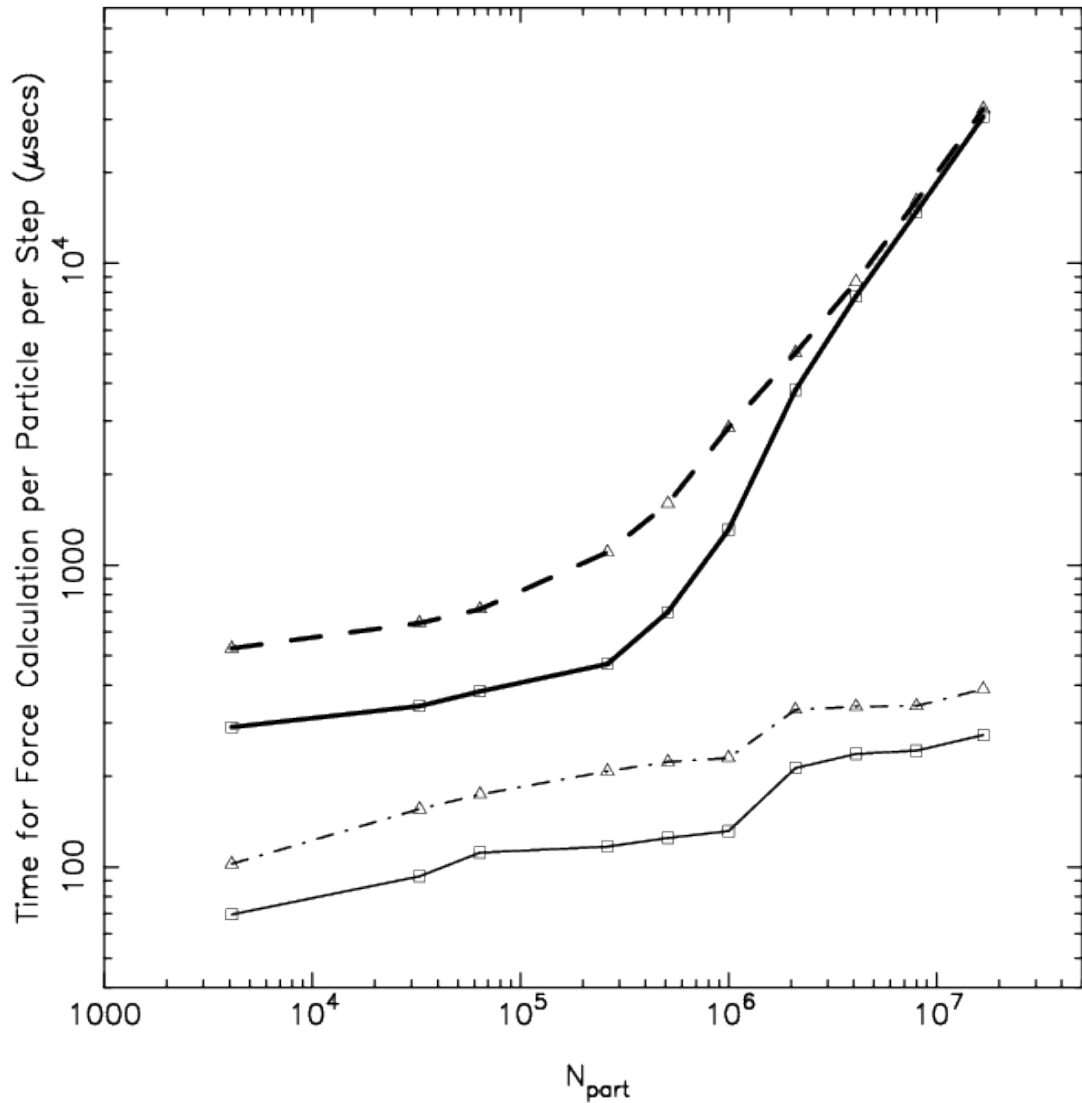


Figure 2.2: Time taken for short-range force calculation per particle per step for $N = 32^3$ to $N = 256^3$ for the TreePM (thick line) and the Modified TreePM (thin line). The solid line shows the performance of the codes on a single core of Intel 5160 (3.0 GHz) processor and the dashed line shows the performance on a single core of the AMD Barcelona (2.1 GHz) processor.

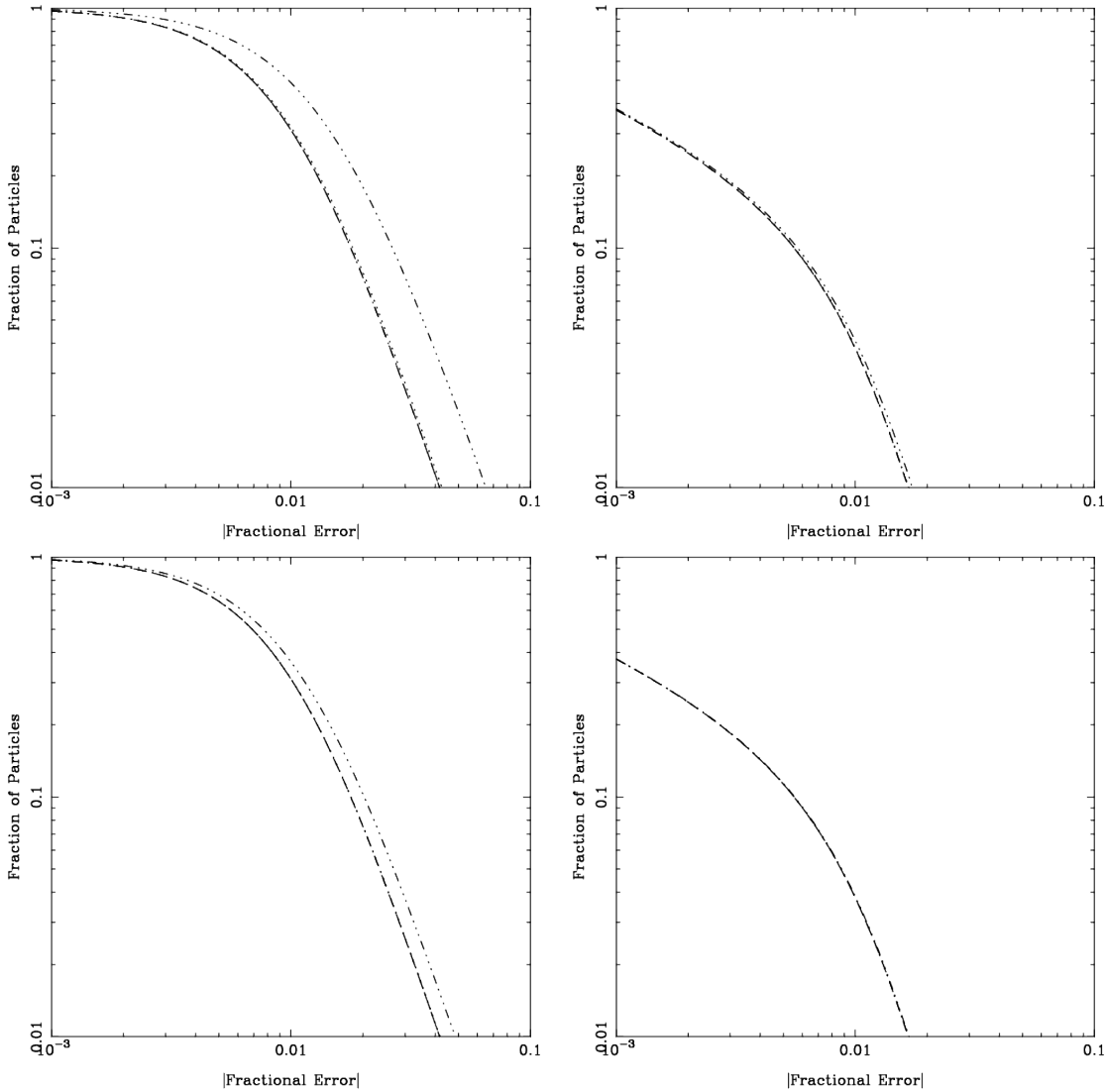


Figure 2.3: Distribution of errors in total force for different values of θ_c with $c_{max} = 2.0$ for unclustered (top left panel) and clustered (top right panel) distributions. Dashed, dot-dash-dot-dash, dotted, dash-dot-dot-dot lines are for $\theta_c = 0.1, 0.2, 0.3$ and 0.5 respectively. We used $r_s = 1.0, r_{cut} = 5.2r_s$ for these plots. The corresponding plots for $c_{max} = 4.0$ are shown in lower left and lower right panels.

such large contributions have to cancel out to give a small net force. Truncation errors in subtracting these large numbers seem to systematically give a net large error. Larger cells contribute for larger θ_c hence the variation with θ_c is more dramatic in the unclustered case. This effect is apparent in the discussion of the short-range force. With $\theta_c = 0.3$, 1% of particles have errors in total force greater than 4% in the unclustered case and 1.6% in clustered case.

The effect of the modified CAC (eq. 2.7) is seen by comparing the plots of figure 2.3 for the unclustered distribution. The modified CAC is more stringent for larger value of c_{max} and this is clearly seen in the error for $\theta_c = 0.5$. There is a lack of variation in errors with θ_c for $\theta_c < 0.5$ indicating that at this stage the dominant contribution to errors is from the long range force calculation. The short-range force is more accurate with a larger c_{max} due to two reasons:

- The modified CAC has an r dependent opening angle threshold and requires a smaller θ_c at small distances. This is likely to reduce errors.
- The number of particles in a group is larger for larger c_{max} . As the contribution of force from these particles is computed by a direct summation over pairs, the errors are negligible.

One may raise the concern that the errors in the present approach are likely to depend on location of a particle within the group. We have checked for anisotropies in error in force calculation in groups that may result and we do not find any noteworthy anisotropic component.

In figure 2.4, we plot the errors in short-range force for the same distributions (unclustered and clustered) of particles for various values of θ_c . The reference short-range force was computed with $\theta_c = 0.01$, $r_s = 1.0$, $r_{cut} = 5.2r_s$ and $c_{max} = 4.0$. We only varied θ_c and continued to use $r_s = 1.0$, $r_{cut} = 5.2r_s$, $c_{max} = 4.0$ for computing the short-range force and then the errors. For the purpose of computing errors in the short range force, we cannot vary r_s between the reference and the test model.

The effect of decreasing θ_c is more dramatic on errors in the short-range force. For the unclustered case the errors for 1% of the particles decreases by nearly 2.5 decades to

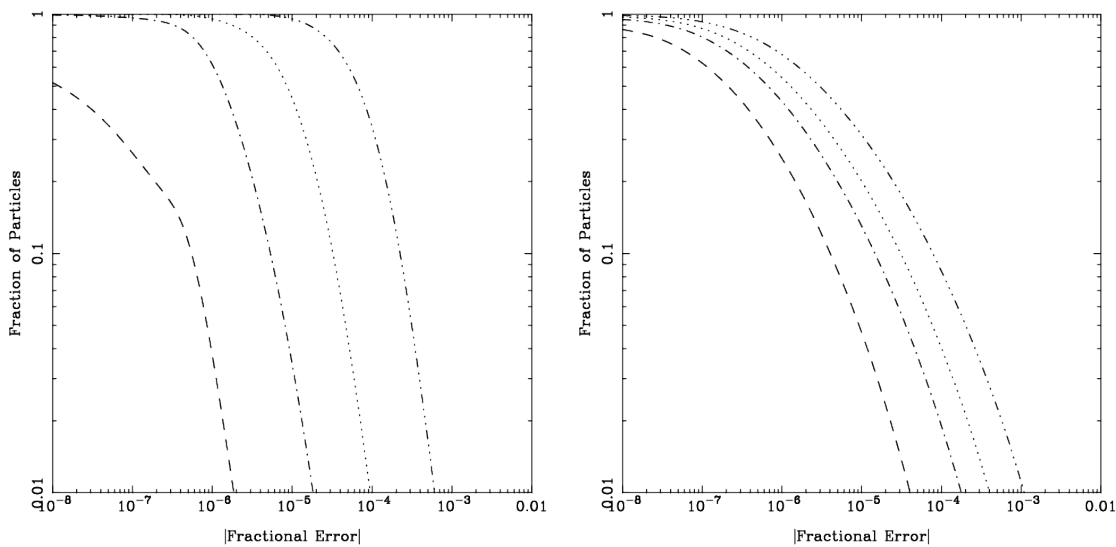


Figure 2.4: Distribution of errors in short range force for different values of θ_c for unclustered (left panel) and clustered (right panel) distributions. Dashed, dot-dash-dot-dash, dotted, dash-dot-dot-dot lines are for $\theta_c = 0.1, 0.2, 0.3$ and 0.5 respectively. $c_{max} = 4.0$, $r_s = 1.0$, $r_{cut} = 5.2r_s$ was used for these plots.

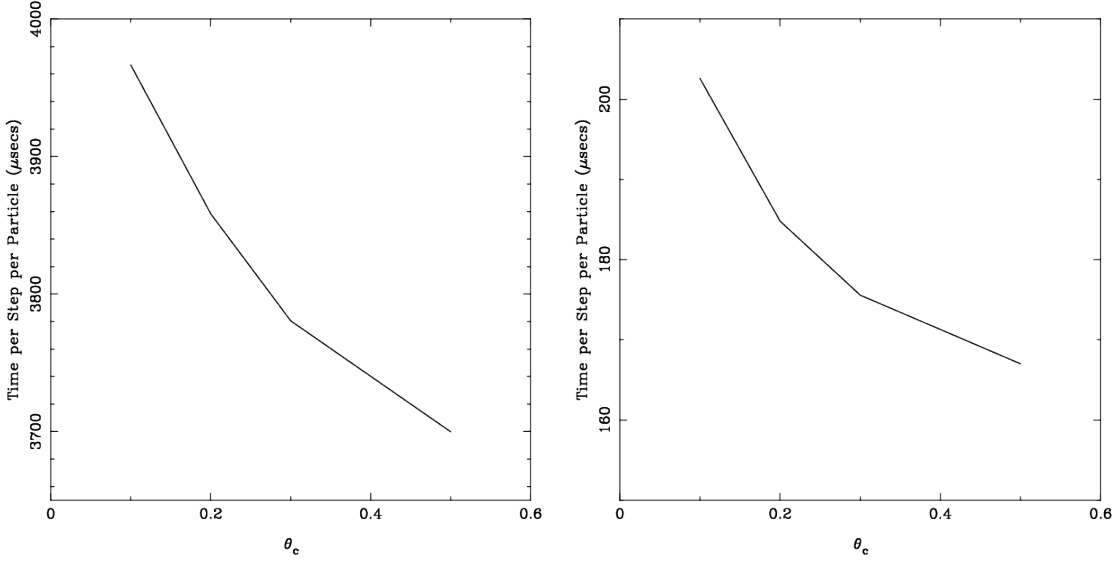


Figure 2.5: Scaling of the time taken for short-range force calculation with θ_c for the TreePM (left panel) and the modified TreePM (right panel).

$2 \times 10^{-4}\%$ for $\theta_c = 0.1$. In the clustered case the errors for 1% of the particles decrease by nearly 1.5 decades to $3.4 \times 10^{-2}\%$ for $\theta_c = 0.1$. One can obtain very high accuracy in short-range force by taking $\theta_c = 0.2$. As the short range force is the dominant one at small scales, the TreePM code can be used to follow the local dynamics fairly well by using a smaller θ_c . The impact of a small θ_c on CPU time remains to be seen though.

In figure 2.5 we look at how the CPU time for force calculation scales with θ_c for the TreePM (left panel) and the modified TreePM (right panel). We compute the time taken for short-range force calculation per particle per timestep. We have seen in figure 2.1 and the corresponding discussion that clustering does not seriously affect the performance of the TreePM code. We therefore do not repeat the exercise for distributions with different levels of clustering. We performed the short-range force timing on a clustered distribution taken from an N -body simulation with $N_{box}^3 = N = 128^3$. We used $r_s = 1.0$ and $r_{cut} = 5.2$ for the TreePM and the modified TreePM. In addition $c_{max} = 4.0$, $n_{p_{max}} = 1024$ were used for timing the modified TreePM. When θ_c is decreased from 0.5 to 0.2 the time for force computation per particle increases by 7.2% for the TreePM and 21% for the

modified TreePM, the fractional increase being larger for the modified code because of the modified CAC. However the modified code is around one order of magnitude faster than the unmodified one for this case and even more for a larger simulation, therefore this scaling with θ_c affects little the performance of the modified code. The speedup of the modified TreePM over the TreePM when θ_c is reduced from 0.5 to 0.2 decreases from 22.2 to 19.6, respectively. A nice feature of TreePM codes is that unlike tree codes, the CPU time taken by TreePM codes is less sensitive to θ_c ². Thus one can obtain much higher accuracy for the short range force with a TreePM code for a considerably smaller cost in terms of the CPU time.

2.5 A Hierarchy of Timesteps

Due to the existence of a large range of dynamical time scales in a simulation of large scale structures, computing forces for slowly moving particles at every timestep is not required. It is better to integrate the orbits of rapidly moving particles with a smaller timestep than those that move relatively slowly, this reduces the number of force calculations that are required. As force calculation is the most time consuming component of an N-Body code, this results in a significant reduction of the CPU time required. We have implemented a hierarchical time integrator similar to that used in GADGET-2 (Springel, 2005), in which particle trajectories are integrated with individual timesteps and synchronised with the largest timestep. As we allow the block time step³ to vary with time, we work with the so called KDK approach (Kick-Drift-Kick) in which velocities are updated in two half steps whereas position is updated in a full step. It can be shown that with a variable time step, KDK performs better than DKD (Drift-Kick-Drift) (see the GADGET-2 paper (Springel, 2005) for details.). In our implementation of the hierarchy of time steps, the smaller time steps differ by an integer power (n) of 2 from the largest, block time step. An array is then used to store the value n which determines the timestep of the particle. The code drifts all

²For example, the CPU time for a tree code increases by about 500% for the same change in θ_c for a simulation with $N \approx 10^4$, and the increase in CPU time is larger for simulations with a larger number of particles (Hernquist, 1987).

³Same as the largest time step.

Table 2.2: This table lists the time taken for a complete simulation run for the unoptimised TreePM, TreePM with hierarchical time steps, TreePM with the group scheme, and finally the TreePM with the group scheme as well as the hierarchical time steps and their speedup with respect to the base TreePM.

Run	Groups	Individual Timesteps	Time (secs)	Speedup w.r.t Run 1
1	No	No	401983	1.0
2	No	Yes	145240	2.77
3	Yes	No	67639	5.94
4	Yes	Yes	31612	12.72

the particles with the smallest timestep to the next time, where a force computation is done for particles that require an updating of velocity (Kick). We have tested the robustness of the hierarchical KDK integrator by successfully integrating the 3–body problem discussed by Szebehely & Peters (Szebehely & Peters, 1967).

Solving the equation of motion with a hierarchy of time steps can be combined with the group scheme. Since tree construction takes a small fraction of the total time, the tree structure can be reconstructed whenever particles require an updating of velocity. The groups that contain such particles can then be identified and particles within each group can be reordered into two disjoint sets: ones that need an updating of velocity and others that don’t. Force is computed only for particles in the first set. Since each group represents a very small fraction of the total number of particles, the overhead of reordering particles is negligible.

Table 2.2 lists the time taken for a complete simulation run for the unoptimised TreePM, TreePM with hierarchical time steps, TreePM with the group scheme, and finally the TreePM with the group scheme as well as the hierarchical time steps and their speedup with respect to the base TreePM. The model used for this comparison is a power law model with $n = -1.0$, $N_{box}^3 = N = 64^3$. We used $r_s = 1.0$, $r_{cut} = 5.2r_s$, $\theta_c = 0.5$ and $\epsilon = 0.2$ in all the runs. Here ϵ is the softening length. We used $c_{max} = 4.0$ and $n_{p_{max}} = 1024$ for the

modified TreePM.

We note that the hierarchical integrator gives a speedup of better than a factor 2, irrespective of whether the scheme of groups is used or not. The speedup is larger if the softening ϵ is smaller, as the number of levels in the hierarchy increases with decreasing ϵ . The scheme of groups on the other hand gives a speedup of 4 or better for small simulations, and a much larger speedup for bigger simulations. This speedup has little dependence on the TreePM parameters, i.e. θ_c , r_s , r_{cut} . The combination of two optimisations gives us a speedup of 10 or more even for small simulations.

2.6 Discussion

The scheme of groups when combined with a hierarchical integrator for the equation of motion guarantees a speedup of better than 10 for any N -body code which uses tree structures for computing forces. From the algorithmic point of view one does not expect a much larger speedup for larger N . However, as seen in figure 2.2, the scheme also allows us to make better use of the cache on CPUs and the effective speedup can be very impressive. We have demonstrated that memory overhead is negligible, and as was observed in (Barnes, 1990) this optimisation just takes around 200 extra lines of code. A welcome feature is more accurate force computation than the code without this modification. This modification in principle introduces two additional parameters (c_{max} , $n_{p_{max}}$), but these are not independent and we have found that $c_{max} \sim r_{cut}$ and $n_{p_{max}} \geq 10^3$ are good choices across a range of simulation sizes.

Our analysis of the optimisation has been restricted to fixed resolution simulations. In case of zoom-in simulations the range of time scales is much larger and a more complex approach for combining the group scheme with the hierarchy of time steps may be required. Relative efficacy of the two optimisations may be very different in such a case when compared with the example studied in the previous section.

In summary, we would like to point out that the scheme of groups leads to a significant optimisation of the TreePM method. The amount of CPU time saved is significant for small simulations, and cache optimisation leads to even more significant gains for large

simulations. We have shown in this paper, that it is possible to incorporate the scheme in a simple manner in any tree based code. The overall gain is very impressive as we are able to combine this with the use of a hierarchy of time steps. The possibility of combining the two optimisations has been explored in this work for the first time.

Chapter 3

The Adaptive TreePM Code

One of the limitations of most cosmological N-body codes stems from the use of a force softening length that is much smaller than the typical inter-particle separation. This leads to departures from collisionless evolution that is desired in these simulations. We propose a particle based method with an adaptive resolution where the force softening length is reduced in high density regions while ensuring that it remains well above the local inter-particle separation. The method, called the Adaptive TreePM, is based on the TreePM code. We present the mathematical model and an implementation of this code, and demonstrate that the results converge over a range of options for parameters introduced in generalizing the code from the TreePM code. We explicitly demonstrate that the evolution of density perturbations is collisionless in collapse of an oblique plane wave. We compare the code with the fixed resolution TreePM code and also an implementation that mimics adaptive mesh refinement methods and comment on the agreement, and disagreements in the results. We find that in most respects the ATreePM code performs at least as well as the fixed resolution TreePM in highly over-dense regions, from clustering and number density of haloes, to internal dynamics of haloes. We also show that the adaptive code is faster than the corresponding high resolution TreePM code.

3.1 Introduction

In modeling gravitational clustering, cosmological N-Body codes should ensure the following:

- The universe does not have a boundary. Therefore cosmological simulations need to be run with periodic boundary conditions¹. The simulation volume should be large enough for the effects of missing modes to be small (Bagla & Ray, 2005; Bagla & Prasad, 2006; Power & Knebe, 2006; Prasad, 2007; Bagla, Prasad, & Khandai, 2009).
- The mass of each particle in simulations should be much smaller than mass scales of interest in the simulation output. This is to ensure adequate mass resolution.
- Each particle in an N-Body simulation represents a very large number of particles/objects in the universe. Thus we must ensure that pair-wise interaction of N-Body particles is softened at scales comparable with the local inter-particle separation. If this is not ensured then the resulting two body collisions introduce errors in the resulting distribution of particles (Splinter et al., 1998; Binney & Knebe, 2002).

In spite of the vast improvement in computing power, simulators have often had to compromise on one or more of these points. Often, errors also creep in due to the approximate methods used for computing force in simulations. A large fraction of current cosmological N-Body codes suffer from collisionality or force biasing. Force is biased when softening lengths ϵ are much larger than the local mean inter-particle separation, \bar{r}_{ij} . Whereas a complementary effect, collisions, occur whenever $\epsilon \ll \bar{r}_{ij}$. The reader is referred to Dehnen (2001) for a detailed discussion on these two effects. Codes that adapt their softening lengths to local densities generally are mostly of the adaptive mesh refinement type. These use a grid for solving the Poisson equation and often have anisotropies in force at scales comparable to the size of a grid cell. Codes that use fixed softening lengths are not entirely collisionless, and, in highly over-dense regions force is biased. The TPM (Xu, 1995; Bode, Ostriker, & Xu, 2000; Bode & Ostriker, 2003) is a particle based code with a one step adaptive resolution. However, in this case the use of the unmodified PM approach for computing

¹An exception are simulations of large spherical volumes that do not suffer significant deformation during the course of evolution.

the long range force introduces significant errors at scales comparable to the grid. In this work we describe a code that addresses all three issues of force anisotropy, collisionality and force biasing by employing an adaptive softening formalism with the TreePM code.

The choice of the optimal softening length has been discussed at length (Merritt, 1996; Athanassoula et al., 2000; Dehnen, 2001; Price & Monaghan, 2007). These studies were carried out in the context of isolated haloes in dynamical equilibrium, e.g., Plummer and Hernquist profiles, therefore errors can be defined clearly. It is also possible to compare various physical quantities in simulations with analytical expressions derived from the distribution function. Dehnen (2001) derived analytical expressions for errors in the context of these profiles. This work suggested that the optimal softening length must adapt to the local inter-particle separation as a function of space and time. Price & Monaghan (2007) developed an energy-momentum conserving formalism with adaptive softening and demonstrated that it was superior to fixed softening. This code was developed for problems where expansion of the Universe is not relevant.

The evolution of perturbations at small scales depends strongly on the mass and force resolution. High force resolutions can lead to better modeling of dense haloes, but gives rise to two body collisions in regions where the softening length is smaller than the local inter particle separation (Splinter et al., 1998; Binney & Knebe, 2002; Diemand et al., 2004; Binney, 2004; El-Zant, 2006; Romeo et al., 2008). As all particles in very high density regions go through such a phase during evolution, any errors arising due to two body collisions can potentially effect the structure of high density haloes that form. A high force resolution without a corresponding mass resolution can also give misleading results as we cannot probe *shapes* of collapsed objects (Kuhlman, Melott, & Shandarin, 1996). In addition, discreteness and stochasticity also limit our ability to measure physical quantities in simulations, and these too need to be understood properly (Thiébaut et al., 2008; Romeo et al., 2008). In all such cases, the error in modeling is large at small scales. It is important to understand how such errors may spread to larger scales and affect physical quantities.

This work is organized as follows. In §3.2 we describe the formalism for adaptive softening in a cosmological N-body code. In §3.3 we describe how adaptive softening is implemented with the TreePM method. We briefly discuss the performance characteristics of ATreePM in §3.4. We discuss validation of the ATreePM code in §3.5 and conclude in

§3.6.

3.2 Adaptive Force Softening

3.2.1 Formalism

The aim of any collisionless N-body code is to self consistently evolve the phase-space distribution function (DF) $f(\mathbf{r}, \mathbf{v}, t)$ under its own gravitational force field $\mathbf{F}(\mathbf{r}, t)$:

$$\partial_t f + (\partial_{\mathbf{r}} f) \cdot \mathbf{v} + (\partial_{\mathbf{v}} f) \cdot \mathbf{F} = 0 \quad (3.1)$$

$$\mathbf{F}(\mathbf{r}, t) = -G \int \int d^3 \mathbf{r}' d^3 \mathbf{v} \frac{\mathbf{r} - \mathbf{r}'}{|\mathbf{r} - \mathbf{r}'|^3} f(\mathbf{r}', \mathbf{v}, t) \quad (3.2)$$

The approach that one takes is to sample the DF, by N phase-space points, $\{\mathbf{r}_i, \mathbf{v}_i\}_{t=t_i}$, at initial time $t = t_i$. Liouville's theorem then states that evolving the trajectories of these points to any time $t > t_i$ will be a representation of the DF at that time. Since the system is a collisionless one, one has to suppress artificial two-body collisions arising out of interactions between particles that are used for sampling the density field. One therefore assigns a finite size to N-Body particles which ensures softening of force at small scales, instead of assuming these to be point particles. The density field when sampled by point particles,

$$\rho(\mathbf{r}) = \int d^3 \mathbf{v} f(\mathbf{r}, \mathbf{v}, t) \equiv \sum_{j=1}^N m_j \delta_D^3(\mathbf{r} - \mathbf{r}_j) \quad (3.3)$$

is now smoothed at small scales if we assign a finite size ϵ to every particle:

$$\rho(\mathbf{r}) = \int d^3 \mathbf{v} f(\mathbf{r}, \mathbf{v}, t) \equiv \sum_{j=1}^N m_j W(|\mathbf{r} - \mathbf{r}_j|, \epsilon) \quad (3.4)$$

where $W(u, \epsilon)$ is known as the smoothing kernel and we have assumed that particles are spherical in shape. Here m_j is the mass of the j^{th} particle. We can now integrate the Poisson equation to obtain the expression for the kernel for computing force and potential. Both the quantities are softened at scales below the softening length ϵ . We choose to work with the cubic spline kernel (Monaghan & Lattanzio, 1985) whose expression is given below.

Complete expressions for the potential and force are given in the Appendix (See Eqn.(A1, A2)).

$$W(u, \epsilon) = \frac{8}{\pi \epsilon^3} \begin{cases} 1 - 6\left(\frac{u}{\epsilon}\right)^2 + 6\left(\frac{u}{\epsilon}\right)^3, & 0 \leq \frac{u}{\epsilon} < 0.5 \\ 2\left(1 - \frac{u}{\epsilon}\right)^3, & 0.5 \leq \frac{u}{\epsilon} < 1.0 \\ 0, & 1.0 \leq \frac{u}{\epsilon} \end{cases} \quad (3.5)$$

In the context of individual softening lengths the density at the location of the i^{th} particle is given by:

$$\rho(r_i) = \sum_{j=1}^N m_j W(r_{ij}, \epsilon_i) = \sum_{j=1}^{n_n} m_j W(r_{ij}, \epsilon_i) \quad (3.6)$$

where i, j indicate the particle indices, $r_{ij} = |\mathbf{r}_i - \mathbf{r}_j|$ and $\epsilon_i \equiv \epsilon(\mathbf{r}_i)$. The summation in principle can be extended upto infinity if the kernel is infinite in extent (e.g., plummer, gaussian kernels). But since such kernels tend to bias the force (Dehnen, 2001; Price & Monaghan, 2007) we work with kernels with a compact support, in particular the cubic spline kernel. Such kernels ensure that the force is $1/r^2$ beyond the softening scale. n_n is the number of the nearest neighbors within ϵ_i for the particle i . In the discussion that follows we assume that this number is fixed for every particle and sets the value of the softening length ϵ_i . We implicitly assume it in our summation. Integrating the Poisson equation we obtain the Green's function for the potential $\phi_{ij} \equiv \phi(r_{ij}, \epsilon_i)$, where the functional form for ϕ is given in the Appendix (See Eqn.(A1, A2)).

With the introduction of individual softening lengths for particles, the symmetry of the potential is lost and momentum conservation is violated. Since $\epsilon(\mathbf{r})$ is now a local quantity, the EOM is incomplete if one takes the expression of force with the fixed softening length ϵ replacing it by a local softening length $\epsilon(\mathbf{r})$. Hence energy conservation also gets violated. This is because the force is derived from the potential and with the introduction of a local softening length $\epsilon(\mathbf{r})$ in the potential, the gradient must also act on $\epsilon(\mathbf{r})$ giving us an extra term. Traditionally this *grad- ϵ* ($\nabla \epsilon$) term has been ignored since in typical applications these were found to be subdominant when compared to the usual force (Gingold & Monaghan, 1982; Evrard, 1988; Hernquist & Barnes, 1990; Monaghan, 1992). It has been shown recently (Price & Monaghan, 2007), that this term plays an important role in N-Body simulations. We study the impact of ignoring this term in Cosmological simulations.

A remedy for momentum non-conservation is to use a symmetrized softening length

$$\epsilon_{ij} = \frac{1}{2}(\epsilon_i + \epsilon_j) \quad (3.7)$$

and plug it into the expression for density to re-derive a symmetrized expression for the potential as $\phi(r_{ij}, \epsilon_{ij})$. This prescription changes the softening length and hence the neighborlist, which one has to recompute. Another disadvantage is that with this prescription for symmetrization, the number of neighbors is not fixed for every particle and hence errors in all smoothed estimates are not the same for every particle. An alternate method (Hernquist & Katz, 1989) is to symmetrize the kernel itself.

$$\begin{aligned} \widetilde{W}_{ij} &= \widetilde{W}_{ji} = \frac{1}{2} [W(r_{ij}, \epsilon_j) + W(r_{ij}, \epsilon_i)] \\ \widetilde{\phi}_{ij} &= \frac{1}{2} [\phi(r_{ij}, \epsilon_j) + \phi(r_{ij}, \epsilon_i)] \end{aligned} \quad (3.8)$$

The total potential is thus

$$\Phi_{tot} = \frac{1}{2} \sum_{i,j}^N \widetilde{\phi}_{ij} \quad (3.9)$$

We can use this to write a Lagrangian which is manifestly symmetric and this ensures momentum conservation. Energy is conserved only if the $\nabla\epsilon$ term is retained in the EOM.

$$L = \sum_i^N \frac{1}{2} m_i v_i^2 - \frac{G}{2} \sum_{i,j}^N m_i m_j \widetilde{\phi}_{ij} \quad (3.10)$$

The EOM of motion can be derived with this Lagrangian (the reader is referred to Price & Monaghan (2007) for details)

$$\begin{aligned} \frac{d\mathbf{v}_i}{dt} &= - G \sum_j m_j \widetilde{\phi}'_{ij} \frac{\mathbf{r}_i - \mathbf{r}_j}{|\mathbf{r}_i - \mathbf{r}_j|} \\ &\quad - \frac{G}{2} \sum_j m_j \left[\frac{\zeta_i}{\Omega_i} \frac{\partial W_{ij}(\epsilon_i)}{\partial \mathbf{r}_i} + \frac{\zeta_j}{\Omega_j} \frac{\partial W_{ij}(\epsilon_j)}{\partial \mathbf{r}_i} \right] \end{aligned} \quad (3.11)$$

Where the first term is the standard Newtonian force term (we refer to it as the $\nabla\phi$ term). The second is the energy conserving $\nabla\epsilon$ term which would be zero for fixed softening.

Notice that all terms are antisymmetric in i, j and hence the total momentum is conserved. Here ζ and Ω are defined as:

$$\zeta_i \equiv \frac{\partial \epsilon_i}{\partial \rho_i} \sum_j m_j \frac{\partial \phi(r_{ij}, \epsilon_i)}{\partial \epsilon_i} \quad (3.12)$$

$$\Omega_i = \left[1 - \frac{\partial \epsilon_i}{\partial \rho_i} \sum_j m_j \frac{\partial W_{ij}(\epsilon_i)}{\partial \epsilon_i} \right] \quad (3.13)$$

Expressions for $\frac{\partial W}{\partial \mathbf{r}}$, $\frac{\partial W}{\partial \epsilon}$ and $\frac{\partial \phi}{\partial \epsilon}$ are given in the Appendix (See A3,A4 and A5). As $\epsilon_i \propto \rho_i^{-\frac{1}{3}}$ we have $\frac{\partial \epsilon_i}{\partial \rho_i} = -\frac{\epsilon_i}{3\rho_i}$. The term Ω term ensures that the EOM is accurate to all orders in ϵ (Springel & Hernquist, 2002).

3.3 The Adaptive TreePM Method

We choose to implement adaptive softening with a modified TreePM code described in chapter 2. In principle one can also incorporate a similar formalism for treecodes (Springel, Yoshida, & White, 2001), P³M codes (Couchman, 1991; Couchman, Thomas, & Pearce, 1995) and other variants like TPM (Xu, 1995), TreePM (Bagla, 2002; Springel, 2005) and GOTPM (Dubinski et al., 2004). We shall discuss one advantage of using the TreePM code with the group optimizations below.

We rewrite the short range potential and force in real space:

$$\varphi^{sr}(\mathbf{r}, \epsilon) = Gm\phi(\mathbf{r}, \epsilon)\text{erfc}\left(\frac{r}{2r_s}\right) \quad (3.14)$$

$$\mathbf{F}^{sr}(\mathbf{r}, \epsilon) = Gm\mathbf{f}(\mathbf{r}, \epsilon)C\left(\frac{r}{r_s}\right) \quad (3.15)$$

$$C\left(\frac{r}{r_s}\right) = \left[\text{erfc}\left(\frac{r}{2r_s}\right) + \frac{r}{r_s\sqrt{\pi}} \exp\left(-\frac{r^2}{4r_s^2}\right) \right] \quad (3.16)$$

Here erfc is the complementary error function. $\phi(\mathbf{r}, \epsilon)$ and $\mathbf{f}(\mathbf{r}, \epsilon)$ are the usual potential and force kernels, respectively. $C(r/r_s)$ modifies the softened Newtonian force kernel $\mathbf{f}(\mathbf{r}, \epsilon)$ to the short-range force $\mathbf{F}^{sr}(\mathbf{r}, \epsilon)$. The expression for $\phi(\mathbf{r}, \epsilon)$ and $\mathbf{f}(\mathbf{r}, \epsilon)$ depend on the kernel $W(r, \epsilon)$ used for smoothing and are given for cubic spline in the Appendix. We find that

tabulating $\text{erfc}(u)$ and $C(u)$ and using interpolation to compute these functions is much more effective than calculating them every time.

The modified TreePM method is characterized therefore by effectively four parameters, r_s , r_{cut} , θ_c and $n_{p_{max}}$. For all our tests we choose conservative values $r_s = 1.0$, $r_{cut} = 5.2r_s$, $\theta_c = 0.3$ and $n_{p_{max}} = 2048$ which give errors below 1% in force. All lengths are specified in units of the PM grid, i.e., size of one cell of the PM grid = 1.

3.3.1 Estimating the Softening Length

Our first task is to get an estimate of the softening length for each particle. A natural way to extract a local length scale uses the numerical value of local density. The local number density is related to the softening length as:

$$\epsilon(\mathbf{r}) \sim \left(\frac{n_n}{n(\mathbf{r})} \right)^{\frac{1}{3}} \quad (3.17)$$

$n(\mathbf{r})$ is the number density at the location of the particle and we assume all particles have the same mass. Here, n_n is a reference number and we take it to be the number of neighbors used for estimation of the number density. The above equation is implicit and can be solved iteratively, see, e.g., Springel & Hernquist (2002); Springel (2005); Price & Monaghan (2007) for details. Price & Monaghan (2007) have shown that errors are not very sensitive to the exact value of n_n . We choose $n_n = 32$ in our simulations, and also comment on variation in results with this choice.

We are using the formalism developed by Price & Monaghan (2007) for achieving an adaptive resolution in gravitational interactions of particles. As the formalism was developed in the context of SPH codes, and some of the quantities required can be computed naturally using the SPH method. These methods were used even though the gravitational interaction is completely collisionless. We follow a similar implementation and use methods commonly used in SPH simulations, even though there are no hydrodynamical effects present in the gravitational interaction being studied here. For an overview of SPH methods, please see Lucy (1977); Gingold & Monaghan (1977).

The SPH methods assign values for functions like the density to particles by averaging over nearest neighbors. The construction of the list of nearest neighbors is an essential

requirement in these methods. All quantities ($\rho, \nabla\epsilon, \Omega, \zeta$ etc.) can be computed at runtime with this neighborlist once we have converged to a value for ϵ by solving Eqn.(3.17). We compute the neighborlist using linked lists (Hernquist & Katz, 1989).

We put bounds on the maximum softening length, ϵ_{max} and ϵ_{min} . A maximum bound is required so that force softening is restricted to the short-range force only, we choose $\epsilon_{max} = \frac{r_s}{2}$ in order to ensure that the long range force is of order 1% of the total force (or smaller) at scales where force softening is important. This ensures that any errors arising from non-modification of the long range force are smaller than 1%, if one puts a lower threshold on the maximum allowed error then the scale ϵ_{max} has to be lowered correspondingly. Alternatively, one can work with a larger r_s and then it becomes possible to allow a larger ϵ_{max} .

In our implementation a neighbor search is carried out only upto ϵ_{max} . Particles which do not have n_n neighbors within ϵ_{max} are assigned $\epsilon_i = \epsilon_{max}$ and the spherical top hat (STH) density is assigned with the number of neighbors within ϵ_{max} . For these particles we assign $\Omega = 1$ and $\zeta = 0$, which makes their $\nabla\epsilon_i = 0$. The $\nabla\epsilon$ term is calculated before the short-range force so that the individual softening lengths needed for short-range force calculation are also assigned in the process.

3.3.2 Memory Requirements

Even though we use two separate data structures, namely linked lists for $\nabla\epsilon$ and tree for $\nabla\phi$ in order to compute the total short-range force, additional memory requirements compared to TreePM are minimal: we require one additional array for storing the softening lengths. The $\nabla\epsilon$ term does not require an additional array since it is a component of the short-range force and it can be computed at run time. This is because the two data structures are never required at the same time. We require specification of the largest force softening length in a given cell (See the subsection on the cell acceptance criterion below.). This amounts to a single precision array of the same size as the number of cells in the tree.

An advantage of using an analytical splitting of force, in the manner TreePM does, is that computation of short-range force does not need global data structures. For example one can geometrically divide regions into smaller regions and construct local trees and

linked lists in them (just like one would go about doing it in a distributed code) and iterate through these regions for computing short-range force instead of constructing one global data structure for the entire simulation volume for computing the short-range force (Dubinski et al., 2004). This reduces memory usage significantly and the dominant part is taken up by the arrays required for computing the long range PM force.

3.3.3 Timestepping Criterion and Integration

We have implemented a hierarchical time integrator similar to that used in GADGET-2 Springel (2005), in which particle trajectories are integrated with individual timesteps and synchronized with the largest timestep. As we allow the block time step² to vary with time, we work with the so called KDK approach (Kick-Drift-Kick) in which velocities are updated in two half steps whereas position is updated in a full step. It can be shown that with a variable time step, KDK performs better than DKD (Drift-Kick-Drift) (see Springel (2005) for details.). We give separate PM (long range, global) kicks and Tree (short range, individual) kicks³. The block timestep Δt^{PM} is determined by the particle which has the maximum PM acceleration a_{max}^{PM} :

$$\Delta t^{PM} = \delta t \left(\frac{\epsilon_{max}}{a_{max}^{PM}} \right)^{1/2} \quad (3.18)$$

Here δt is the dimensionless accuracy parameter. In our implementation of the hierarchy of time steps, the smaller time steps differ by an integer power (n) of 2 from the largest, block time step. An array is then used to store the value n which determines the timestep of the particle. Individual timesteps Δt_i are first calculated:

$$\Delta t_i^{sr} = \delta t \left(\frac{\epsilon_i}{a_i^{sr}} \right)^{1/2} \quad (3.19)$$

and then the appropriate hierarchy n is chosen depending on this value. Here a_i^{sr} and ϵ_i are the moduli of the individual short-range acceleration (sum of the $\nabla\phi$ and $\nabla\epsilon$ terms) and the softening lengths respectively. TreePM has a similar time-stepping criterion with ϵ_i replaced by ϵ .

²Same as the largest time step.

³Tree kick includes the contribution of the $\nabla\epsilon$ term.

The code drifts all the particles with the smallest timestep to the next time, where a force computation is done for particles that require an updation of velocity (Kick). However the neighborlist and individual softening lengths ϵ_i are computed for all particles at every small timestep. This is because, even though some particles do not require a velocity update, their neighbors might require one for which they would contribute through their updated softening lengths. The $\nabla\epsilon$ term however is computed only for those particles requiring a velocity update.

Within a given block time step, the smaller time steps are constant for a given particle. The time smaller step changes across block time step and this brings in inaccuracies in evolution of trajectories. It is possible, in principle, to ensure that the second order accuracy is maintained here. However, we find that the time steps for particles change very slowly and this change does not affect trajectories in a significant manner.

The Courant condition is satisfied for the choice of δt we use. Indeed, we chose δt by requiring that two particles in a highly eccentric orbit around each other maintain the trajectory correctly for tens of orbits.

3.3.4 Cell Acceptance Criterion For ATreePM

The adaptive force resolution formalism requires us to symmetrize force between particles that are separated by a distance smaller than the larger of the two softening lengths. Without this, the momentum conservation cannot be ensured. For pairs of particles separated by larger distances, there is no need to explicitly symmetrize force as there is no dependence on the softening length at these scales⁴. Thus the cell acceptance criterion needs to be changed within the tree part of the code to ensure that for pairs of particles

⁴As an aside we would like to note that the Tree method does not conserve momentum explicitly. This is because the tree traversal approximates the force due to pairwise interactions, and in the process the pairwise symmetry is lost. In the modified Tree method (Barnes, 1990; Makino, 1991; Yoshikawa & Fukushige, 2005; Khandai & Bagla, 2009) explicit pairwise force is computed for particles within each *group*. Particles within a group have a common interaction list for force due to particles outside the group. Exact pairwise PP force is computed explicitly for intra-group particles and we have a pairwise symmetry for this component, but for interaction with particles outside the group there is no explicit pairwise symmetry and hence no explicit momentum conservation.

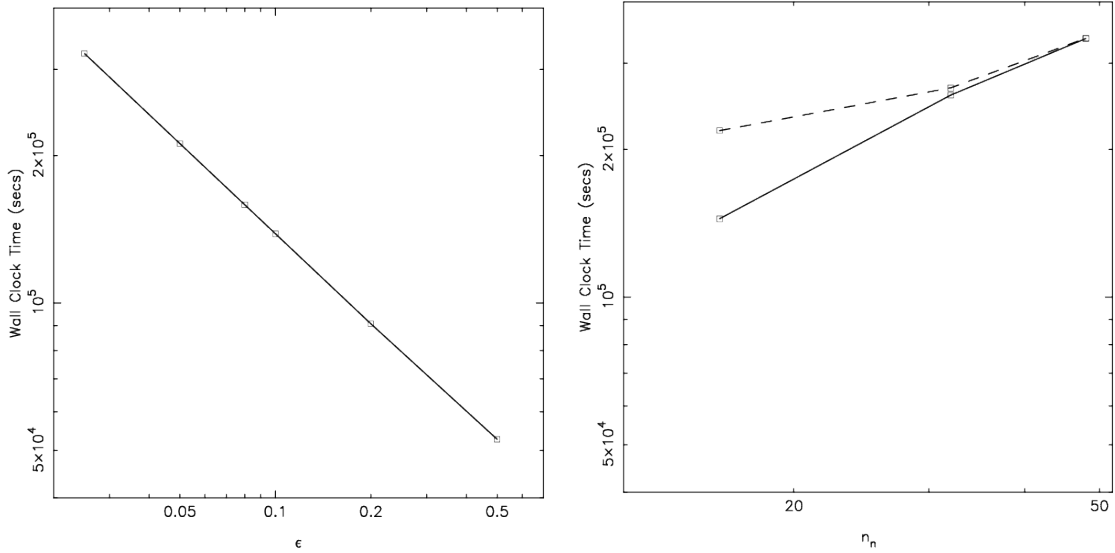


Figure 3.1: Wall clock timing for TreePM (left) as a function of ϵ and ATreePM (right) with $\nabla\epsilon$ (solid) and without $\nabla\epsilon$ (dashed) as a function of n_n

separated by the critical distance, forces are computed through pairwise particle-particle (PP) interaction. In our implementation, along with particles, cells (and hence groups) are assigned softening lengths corresponding to the particle contained within the cell that has the largest softening length. The CAC, that is modified when we go from the TreePM to the modified TreePM (Khandai & Bagla, 2009) has to be refined further to take into account the largest softening lengths for particles within cells and groups whose interaction is to be computed.

$$\frac{(L_{cell} + \epsilon_{cell}^{max})}{(r_{gcm} - L_{group} - \epsilon_{group}^{max})} \leq \theta_c \quad (3.20)$$

ϵ_{cell}^{max} , ϵ_{group}^{max} are the softening lengths of the cell and group (in the sense explained above) respectively. r_{gcm} is the distance separating the centers of mass of the group and the cell. L_{cell} is the size of the cell and L_{group} is the distance to the furthest particle from the center of mass of the group. This CAC ensures that the interaction of particles separated by less than the softening length is computed in a direct pairwise manner and hence can be explicitly symmetrized. These are also the pairs for which the $\nabla\epsilon$ term needs to be computed.

3.4 Performance characteristics

3.4.1 Timing

We now look at the wall clock time as a measure of performance between different codes. We studied evolution of a power law model with $n = -1$ using 128^3 particles up to the stage where the scale of non-linearity is 6 grid lengths. More details of the run are given in the section on validation of the ATreePM code. Figure 3.1 shows wall clock time as a function of softening length ϵ for TreePM (left panel) and the wall clock time as a function of n_n for the ATreePM codes.

We can qualitatively understand the slope for the TreePM curve by looking at the equivalent time-stepping criterion as Eqn.(3.19) for TreePM.

$$\Delta t_i^{sr} = \delta t \left(\frac{\epsilon}{a_i^{sr}} \right)^{1/2} \quad (3.21)$$

From here the naive expectation is that the time taken should scale as $\epsilon^{-0.5}$. The slope of the curve is in the range -0.55 to -0.65 . The reason for this small deviation lies in our use of a hierarchy of time steps, where trajectories of all the particles are not updated at every time step. However, positions of particles are updated at every time step and this operation as well as those related to creating the tree structure at every step add an overhead. This overhead becomes more and more important at small ϵ where we have many more levels of hierarchy realized in a simulation. This leads to steepening of the curve from the simple expectation given above.

For the ATreePM, we expect softening lengths to be larger for larger n_n . On the other hand, a larger n_n implies a larger neighborlist and the time taken for setting up the neighborlist increases. The second effect is the dominant one and we see that the time taken for Adaptive TreePM increases with n_n . We see that time taken by both variants of ATreePM is similar for $n_n = 32$ and 48 . This indicates that the time taken for calculation of the $\nabla\epsilon$ term is negligible. There is a difference between the timing for $n_n = 16$, as the code with the $\nabla\epsilon$ does not evolve the system correctly: this can be seen in all the indicators like the amplitude of clustering, mass function, etc., presented in the next section. We see that TreePM with $\epsilon = 0.025$ takes 50% more time than ATreePM with $n_n = 32$, whereas

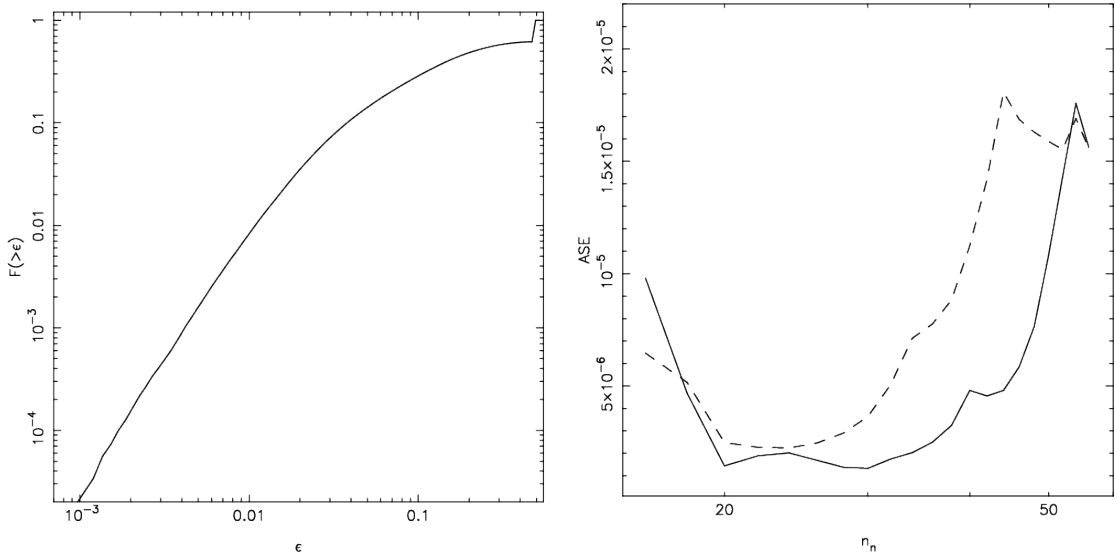


Figure 3.2: *Left:* Cumulative distribution of softening lengths at the final epoch of an N-Body simulation (See Figure 3.8 bottom-left). *Right:* Average square error (ASE) for ATreePM with $\nabla\epsilon$ (solid line) and ATreePM without $\nabla\epsilon$ (dashed line) as a function of n_n

the time taken is comparable with ATreePM with $n_n = 48$.

Since ϵ is assigned by hand in TreePM, the use of a small softening length means a considerable number of particles obtain a small timestep even though the acceleration for these particles is small and does not vary rapidly with time. In the hierarchical integrator that we use, this means that force computation is done more often within a block timestep. In ATreePM on the other hand a small softening is only assigned to particles in over-dense regions. This saves time in the under-dense and not so over-dense regions and the ATreePM code devotes more time to evolving trajectories in highly over-dense regions. This is illustrated in Figure 3.2 where we have plotted the cumulative distribution of softening lengths at the final epoch in one of the simulations used here (see lower-left panel of Figure 3.8). The softening length has been computed here for $n_n = 32$. We find that only 5% of the particles have a softening length smaller than the smallest softening length $\epsilon = 0.025$ used for the fixed resolution simulations. Even at this epoch where highly non-

linear clustering is seen, nearly half the particles have a softening length corresponding to the maximum value of 0.5. This shows how we are able to evolve the system in an ATreePM simulation with a lower computational cost while resolving highly over-dense regions.

3.4.2 Errors

In this section we discuss the dependence of errors on n_n . In cosmological simulations it is difficult to define errors when softening lengths are varied due to the lack of a reference setup. Nevertheless we can choose the optimal softening length such that one minimizes the globally averaged fluctuation in force as the softening lengths are varied. Following Price & Monaghan (2007), we define average square error:

$$ASE(n_n) = \frac{B}{N} \sum_i^N |\mathbf{f}_i(n_n) - \mathbf{f}_i(n_n + \Delta n_n)|^2 \quad (3.22)$$

N is the total number of particles. B is a normalization constant which is taken as $1/f_{max}^2$, with f_{max} being the largest value of force in either runs. Δn_n is the change in n_n and we choose this to be 8. The behaviour of errors with n_n remains qualitatively the same with other values of Δn_n . Figure 3.2 shows ASE as function of n_n for ATreePM with $\nabla\epsilon$ (solid line) and ATreePM without $\nabla\epsilon$ (dashed line). These are computed for the same clustered distribution of particles. The qualitative behavior of ASE here is same as seen in (Price & Monaghan, 2007). At small n_n ATreePM with $\nabla\epsilon$ has larger errors than ATreePM without $\nabla\epsilon$. This is also reflected in the poor evolution of density fluctuations with $n_n = 16$ for the ATreePM with $\nabla\epsilon$, discussed in the next section. Both variants have a minima, the value of error at the minima being lower for ATreePM with the $\nabla\epsilon$ term. Another interesting feature is that the region where errors are small is fairly broad for the ATreePM with the $\nabla\epsilon$ term. For larger n_n the error increases sharply for ATreePM without the $\nabla\epsilon$ term. Thus the optimal configuration is the one with the $\nabla\epsilon$ term and $20 \leq n_n \leq 32$.

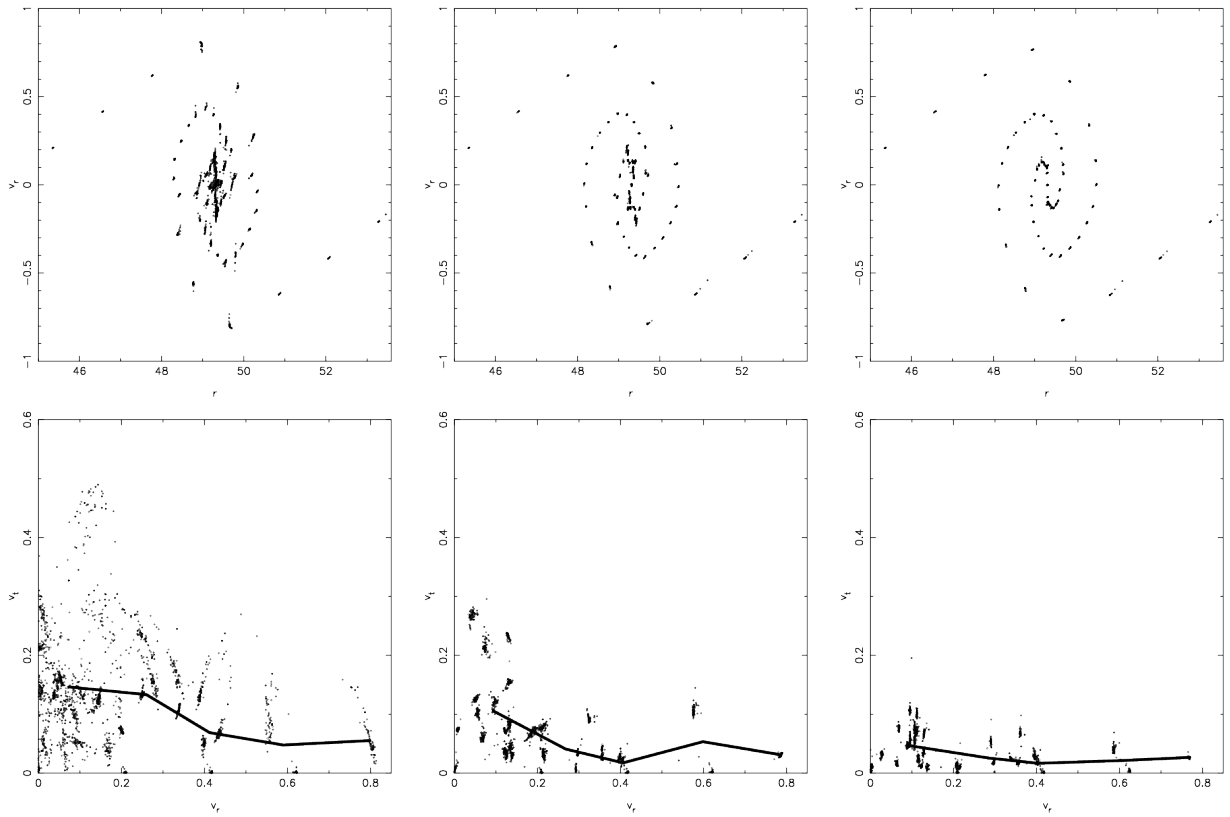


Figure 3.3: Top row: Phase plots of the normal (to one of the planes of collapse) component of the velocity vs normal component of particle displacement for TreePM with $\epsilon = \frac{r_s}{10}, \frac{r_s}{4}, \frac{r_s}{2}$ (columns 1-3 respectively). Bottom row: Transverse component of velocity along one of the planes of collapse for the above runs. The scatter plot shows this for a random subset of particles, whereas the line shows the average value in a few bins.

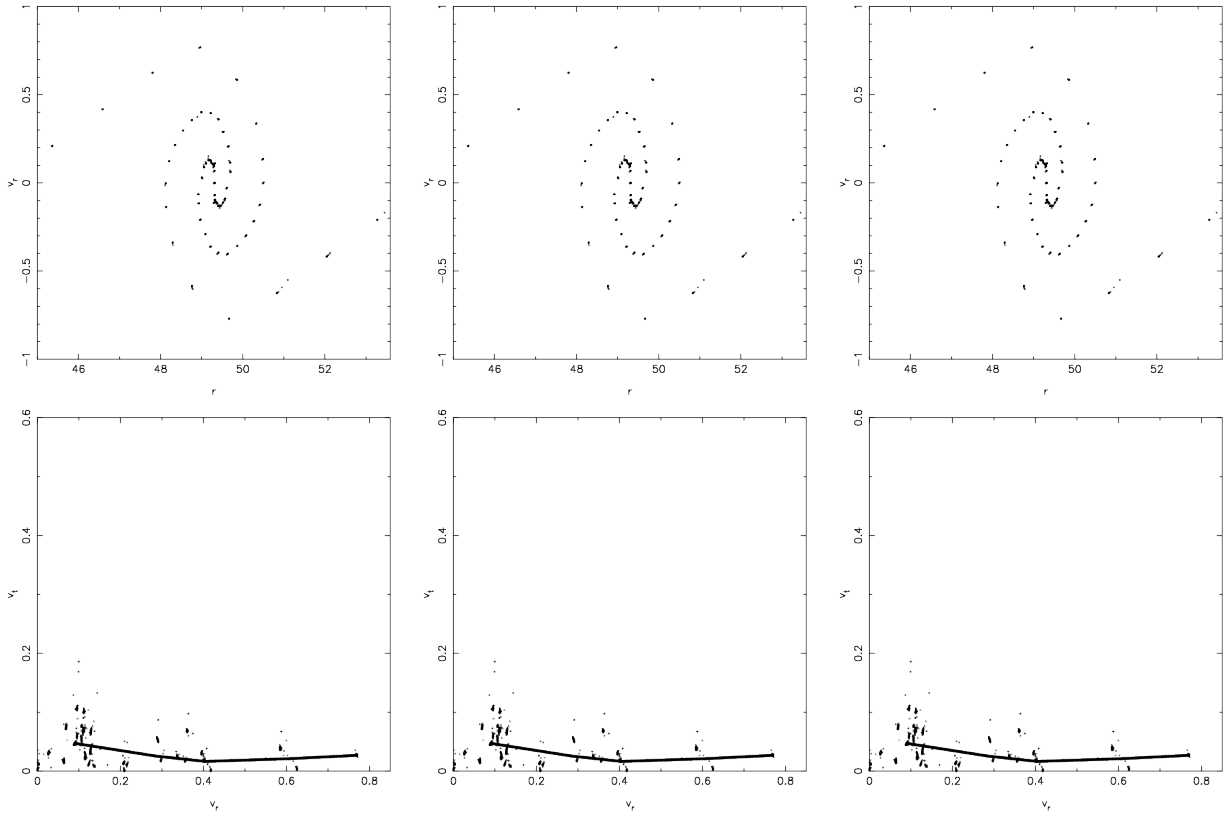


Figure 3.4: Top row: Phase plots of the normal component of particle displacement vs normal component of the velocity for ATreePM with $\epsilon_i \leq \frac{r_s}{2}$ for $n_n = 16$ without $\nabla\epsilon$, $n_n = 16$ with $\nabla\epsilon$ and $n_n = 32$ with $\nabla\epsilon$ (columns 1-3 respectively). Bottom row: Normal component of velocity vs Transverse component of velocity along one of the planes of collapse for the above runs. The scatter plot shows this for a random subset of particles, whereas the line shows the average value in a few bins.

3.5 Validation of the Adaptive TreePM code

Cosmological N-Body simulations lack the equivalent of equilibrium distribution functions for haloes, e.g., Plummer halo that may be used to validate a new code. Use of such equilibrium distributions allows one to quantify errors in a clean manner. However, given that the formalism we use is the same as that presented by Price & Monaghan (2007), and that their implementation works well with such tests gives us confidence in the formalism. In the following discussion, we will test the Adaptive TreePM code in a variety of ways and look for numerical convergence. We compare the performance of the Adaptive TreePM with the fixed resolution TreePM. We also study the role of the $\nabla\epsilon$ term and check if dropping this term leads to significant changes in the evolution of clustering. This last point is important as most AMR codes do not have an equivalent term in the equation of motion.

3.5.1 Two-body collisions: plane wave collapse

We start by checking whether the adaptive force softening suppresses two body collisions in the Adaptive TreePM code. We repeat a test recommended by Melott et al. (1997) where they study the collapse of an oblique plane wave. In this test, the collapse should not lead to any transverse motions if the evolution is collisionless. Melott et al. (1997) had shown that codes where the force softening length is much smaller than the inter-particle separation are collisional and lead to generation of significant transverse motions. Some authors (Heitmann et al., 2005) have stated that the failure to ensure planar symmetry may not have a one to one correspondence with collisionality. However, the test is nevertheless an important one and we present the results with the ATreePM code here.

We use exactly the same initial perturbations as used by Melott et al. (1997). The simulations are done with 64^3 particles and a 64^3 grid. We choose $r_s = 1$ grid length. Other simulation parameters are as described in the subsection §3.3 on the TreePM code. The output is studied at $a = 3$, following Melott et al. (1997).

We first conduct the test with the fixed resolution TreePM code. Top row of the Figure 3.3 shows the phase portrait along the direction of collapse for different choices of

the force softening length. The softening length varies between $0.1 \leq \epsilon \leq 0.5$ in units of the mean inter-particle separation. We see that the phase portrait in the multi-stream region is heavily distorted for the smallest force softening length but is correct for the largest force softening length used here. This reinforces the conclusions of Melott et al. (1997) that using a force softening length that is much smaller than the mean inter-particle separation leads to two body collisions. This point is presented again in the lower row of Figure 3.3 where we show a scatter plot of modulus of the transverse (to the direction of collapse) velocities and radial velocities. This is shown for a random sub-set of all particles. We see that transverse motions are significant for the simulation with the smallest force softening length, but are under control for the largest force softening length. Thick line in the lower panels connects the average modulus of the transverse velocities in bins of magnitude of radial velocity. The visual impression gathered from the scatter plot is reinforced in that with decreasing force softening length, we get larger transverse motions.

Figure 3.4 presents results of simulations with the same initial conditions carried out with the Adaptive TreePM code. We show the results for Adaptive TreePM without the $\nabla\epsilon$ term, $n_n = 16$ (left column); with the $\nabla\epsilon$ term, $n_n = 16$ (middle column), and, with the $\nabla\epsilon$ term, $n_n = 32$ (middle column). In general we do not recommend use of $n_n = 16$ due to reasons discussed in the preceding subsection on errors, discussion in the following subsections, and in Price & Monaghan (2007), but we nevertheless use it in order to look for early signs of two body collisions in a simulation with a relatively small number of particles. The phase portrait for all the three Adaptive TreePM runs is a faithful representation of the expectations. The transverse motions are suppressed strongly, almost to the same level as the TreePM simulation with a force softening of $\epsilon = 0.5$. One of the reasons for this is that the highest overdensities reached in this experiment do not lead to a considerable reduction in the force softening length. The other reason is that the adaptive nature of the code leads to presence of a sufficient number of neighbours within a force softening length and hence the anisotropy in the transverse force is reduced substantially.

Thick lines in the lower panels show the modulus of the average transverse velocities in a few bins of the modulus of the longitudinal velocity. We see that for TreePM, the magnitude of transverse motions drops rapidly as we increase the force softening length. We also note that for the adaptive TreePM, the magnitude of transverse motions is similar

to that seen with the TreePM when ϵ for the TreePM coincides with the ϵ_{max} for the ATreePM.

We conclude the discussion of this test by noting that our requirement of $\epsilon \gtrsim \bar{r}_{ij}$, where \bar{r}_{ij} is the local inter-particle separation, ensures collisionless behavior in evolution of the system.

3.5.2 Convergence with n_n and relevance of the $\nabla\epsilon$ term

For the following discussions we run a power-law model with index $n = -1.0$. The spectrum is normalized at a an epoch when the scale of non-linearity $r_{nl} = 6.0$ in grid units. The scale of non-linearity is defined as the scale at which the linearly extrapolated mass variance, defined using a top hat filter, is unity $\sigma(r_{nl}, z) = 1$. The simulations are done with 128^3 particles and a 128^3 grid. We choose $r_s = 1$ grid length. Other simulation parameters are as described in the subsection §3.3 on the TreePM code. We assume that the Einstein-de Sitter model describes the background universe. In this case self-similar evolution of quantities for power law models provides an additional test for simulation results.

Clustering Properties

We compute the volume averaged 2–point correlation function $\bar{\xi}$.

$$\bar{\xi}(r) = \frac{3}{r^3} \int_0^r \xi(x) x^2 dx \quad (3.23)$$

ξ is the two point correlation function (Peebles, 1980). To compute $\bar{\xi}$ from simulation output, we take 15 independent random subsets of 10^5 particles each. We then estimate the average value of $\bar{\xi}$ over these subsets. The maximum and the minimum values of $\bar{\xi}$ in these subsets are our estimate of the errors. Figure 3.5 shows $\bar{\xi}$ at an epoch when $r_{nl} = 6.0$. TreePM (left column) with $\epsilon = 0.025, 0.05, 0.1, 0.2, 0.5$ are shown in black, red, blue, ochre and magenta respectively. ATreePM with $\nabla\epsilon$ (middle column) and ATreePM without $\nabla\epsilon$ (right column) with $n_n = 16, 32, 48$ are shown in blue, red, black lines respectively. The lower row is a zoom-in of $\bar{\xi}$ so as to highlight the differences at small scales, due to the variation in ϵ and n_n in different runs.

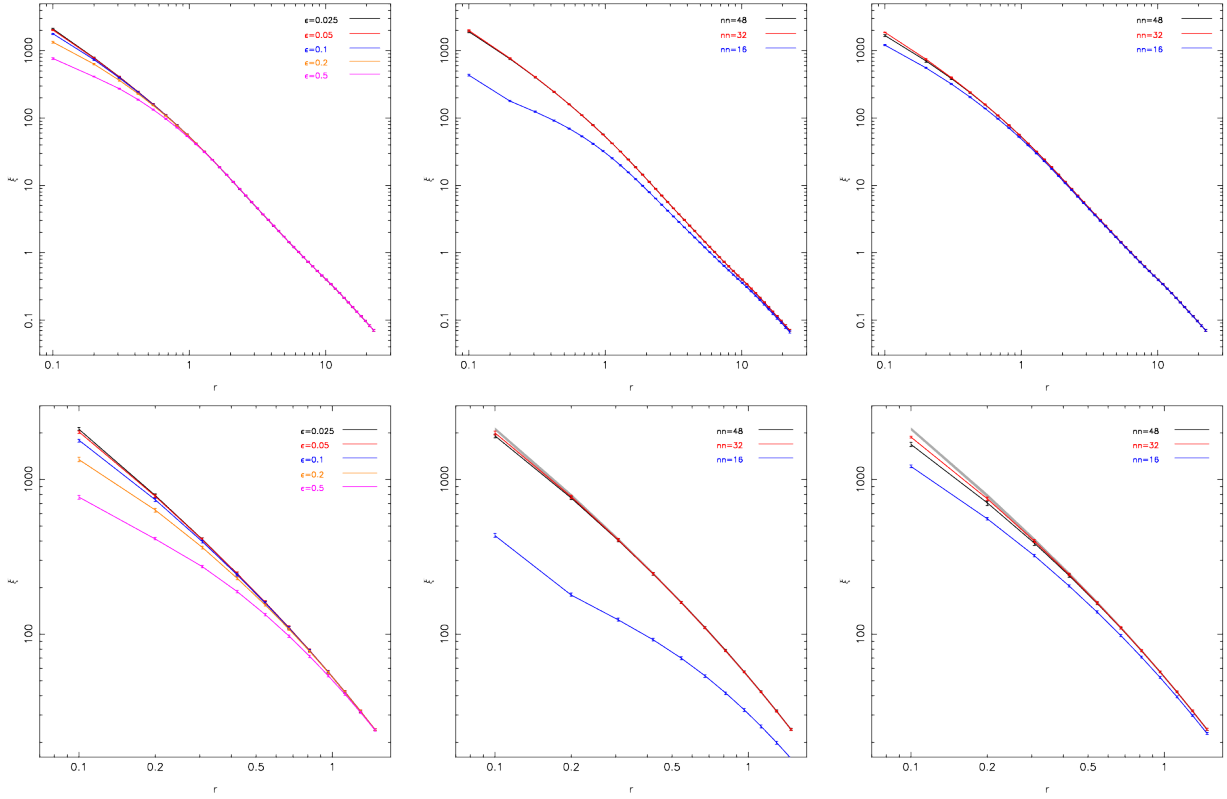


Figure 3.5: *Top Row:* This figure plots the volume averaged 2-point correlation function $\bar{\xi}$ as a function of scale at $r_{nl} = 6.0$ for TreePM (left) and ATreePM with $\nabla\epsilon$ (middle) and ATreePM without $\nabla\epsilon$ (right). The four curves (black, red, blue, ochre, mauve) for TreePM are for runs with softening lengths of $\epsilon = \frac{r_s}{40}, \frac{r_s}{20}, \frac{r_s}{10}, \frac{r_s}{5}, \frac{r_s}{2}$. For the ATreePM runs the three curves (black, red, blue) are for $n_n = 16, 32, 48$. *Bottom Row:* zoomed in plots of Top Row. Grey surface in the ATreePM plots is $\bar{\xi}$ bounded by error-bars for TreePM with $\epsilon = \frac{r_s}{40}$

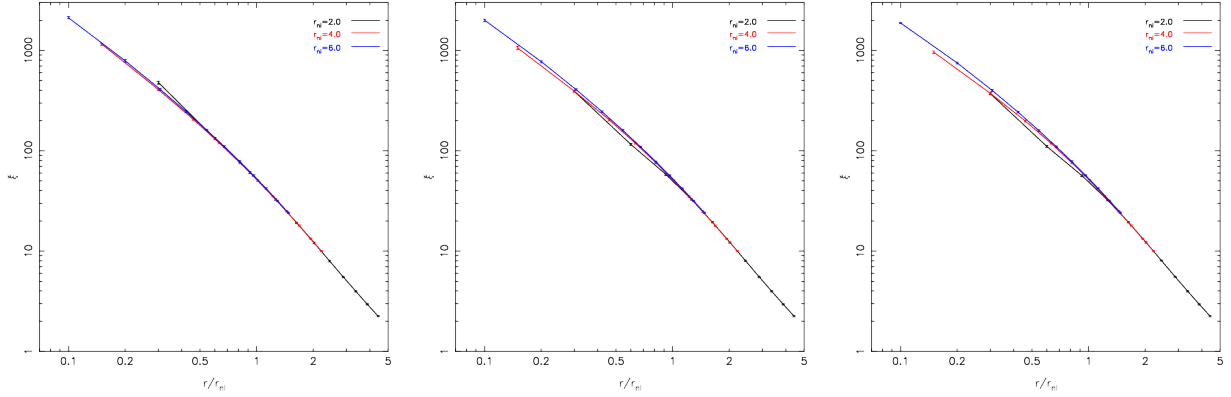


Figure 3.6: This figure tests self similar evolution of the scaled 2-point correlation function $\bar{\xi}(r/r_{nl})$ by plotting it at the epochs when $r_{nl} = 2.0, 4.0, 6.0$ (black, red, blue lines)for TreePM (left) ATreePM with $\nabla\epsilon$ (middle) , ATreePM without $\nabla\epsilon$

One can show that we require a minimum of 12 neighbors to solve for Eqn.(3.17). The $\nabla\epsilon$ term is important in over-dense regions where $\epsilon_i \ll \epsilon_{max}$, and is a rapidly varying function of density, one therefore requires a reasonably large n_n to compute it accurately. Use of a small n_n leads to a noisy estimate of $\nabla\epsilon$ and Figure 3.5 illustrates this point⁵. With $n_n = 16$, $\bar{\xi}$ deviates significantly from our expectations. Disagreement is worse for ATreePM with $\nabla\epsilon$, as this is the case where a poor estimate of the extra term leads to larger errors. If we use a larger n_n , we expect to see convergence at some point. Curves for $n_n = 32$ and 48 agree with each other (within error-bars) for ATreePM with $\nabla\epsilon$ indicating that evaluation of the extra term is stable. It also indicates that this extra term compensates for the use of a larger number of particles, otherwise typical softening length is expected to be larger for higher n_n and this should lead to lowering of the clustering amplitude at small scales. This is very clearly illustrated for TreePM (left column in Figure 3.5) where increasing ϵ reduces $\bar{\xi}$ monotonically. We also see this effect for ATreePM without the $\nabla\epsilon$ term where the amplitude of clustering is much smaller for $n_n = 48$ as compared to $n_n = 32$ and the difference between the two is more than twice that seen for ATreePM with the $\nabla\epsilon$ term. Such a behavior is expected, and has been seen by Price & Monaghan (2007)in a

⁵Also see Figure 3.2.

Table 3.1: The following table shows the variation of r_{con} and r_{ss} with time for TreePM and the two variants of ATreePM as a function of softening

Runs	r_{con} $r_{nl} = 6.0$	r_{con} $r_{nl} = 4.0$	r_{con} $r_{nl} = 2.0$	r_{ss} $r_{nl} = 6.0$	r_{ss} $r_{nl} = 4.0$
TreePM ($\epsilon = \frac{r_s}{2}$)	1.2	0.96	0.61	1.1	0.67
TreePM ($\epsilon = \frac{r_s}{5}$)	0.61	0.44	0.36	0.42	0.15
TreePM ($\epsilon = \frac{r_s}{10}$)	0.25	0.20	0.10	0.18	0.16
TreePM ($\epsilon = \frac{r_s}{20}$)	0.10	0.10	0.10	0.10	0.17
TreePM ($\epsilon = \frac{r_s}{40}$)	-	-	-	0.10	0.18
ATreePM ($\nabla\epsilon, n_n = 32$)	0.10	0.15	0.30	0.27	0.31
ATreePM ($\nabla\epsilon, n_n = 48$)	-	-	-	0.42	0.47
ATreePM ($n_n = 32$)	0.27	0.28	0.38	0.54	0.42
ATreePM ($n_n = 48$)	-	-	-	0.59	0.50

different context. They noted that the increase in force softening length with n_n leads to a bias in the force at small scales. The $\nabla\epsilon$ term corrects for this and biasing of force is less important. Since the distribution of particles gets more strongly clustered with time, we expect over-softening of the force field to degrade further evolution for the TreePM and the ATreePM without $\nabla\epsilon$, beyond a certain epoch.

We have plotted the scaled 2-point volume averaged correlation $\bar{\xi}(r/r_{nl})$ at small scales in Figure 3.6 for TreePM with $\epsilon = 0.025$ (left panel), ATreePM with the $\nabla\epsilon$ term (middle panel) and ATreePM without the $\nabla\epsilon$ term (right panel). We used simulations with $n_n = 32$ for both the ATreePM runs shown here. $\bar{\xi}$ has been computed at epochs when the scale of non-linearity $r_{nl} = 2, 4$ and 6 (black, red and blue lines respectively). Since the only scale in power-law models is the scale of non-linearity r_{nl} , introduced by gravity, one expects $\bar{\xi}$ to evolve in a self-similar manner. The scale of self-similarity, r_{ss} , for a given epoch is determined by finding the scale at which $\bar{\xi}$ matches with the $\bar{\xi}$ of the earlier epoch within the error bars computed in the manner described above.

We illustrate numerical convergence properties of the three codes in table 3.1. Here, we list the scale r_{con} and r_{ss} at different epochs. For ATreePM r_{con} is the scale beyond which $\bar{\xi}$ with the given n_n matches with a reference $\bar{\xi}$ with $n_n = 48$. For TreePM this is the scale where $\bar{\xi}$ with a given force softening length matches with the reference $\bar{\xi}$ with $\epsilon = 0.025$.

We find that both variants of ATreePM converge with time, the convergence being more rapid for ATreePM with $\nabla\epsilon$ as compared to ATreePM without $\nabla\epsilon$. The scale of convergence r_{con} is also smaller for ATreePM with $\nabla\epsilon$. On the other hand self-similar behavior is degraded with evolution for ATreePM without $\nabla\epsilon$ as r_{ss} increases with time, whereas for ATreePM with the $\nabla\epsilon$ term the evolution is self-similar over a larger range of scales.

Thus we may conclude that the ATreePM with the $\nabla\epsilon$ has well defined numerical convergence as we vary n_n , and the evolution of power law models for this code is self-similar over a wide range of scales. This sets it apart from the ATreePM without the $\nabla\epsilon$ term, where the convergence with n_n is not well defined and the evolution of a power law model is self-similar over a smaller range of scales. Better match with the fixed resolution TreePM code is an added positive feature for the code with the $\nabla\epsilon$ term. This raises obvious questions about AMR codes, where no such term is taken into account as we increase the resolution of the code. We comment on this issue in the Discussion section.

We briefly comment on the convergence and self-similar evolution in the fixed resolution TreePM code. As seen in Table 3.1, we find that at early times the scale above which we have self-similar evolution is almost the same for $\epsilon \leq 0.2$. This may indicate discreteness noise, or it may be due to two body collisions during early collapse (Splinter et al., 1998; Melott et al., 1997; Joyce, Marcos, & Baertschiger, 2008; Romeo et al., 2008). At late times, the scale above which evolution is self-similar is $r_{ss} \sim 2\epsilon$. This indicates that any transients introduced at early times by discreteness, etc. have been washed out by the transfer of power from large scales to small scales (Little, Weinberg, & Park, 1991; Evrard & Crone, 1992; Bagla & Padmanabhan, 1997; Bagla & Prasad, 2008). Thus one gets an improved self-similar evolution at late times in the fixed resolution TreePM with the use of a smaller softening length.

On the other hand we see that for TreePM, r_{con} increases with time. As defined

above, this is the scale at which $\bar{\xi}$ obtained with a given value of ϵ matches with the value obtained using $\epsilon = 0.025$. We find that at the last epoch $r_{con} \geq 2\epsilon$, whereas at early times the limit is $r_{con} \geq \epsilon$. This trend is contrary to that seen with the ATreePM for which r_{con} decreases with time, the rate at which it comes down being faster for the ATreePM with the $\nabla\epsilon$. We would like to point out that we do not probe $\bar{\xi}$ for scales $r < 0.1$ as the number of pairs with a smaller separation is often too small to get reliable estimates of $\bar{\xi}$.

Another remarkable fact is that for the TreePM code, $r_{ss} \leq r_{con}$. Thus we have the desired behavior in terms of evolution even though we are yet to achieve numerical convergence at the relevant scales. Such a problem does not exist for the ATreePM code.

Lastly, as we show below, the ATreePM code is very good at resolving highly over-dense regions very well. This would appear to be in contradiction with the slightly lower two point correlation function. The reason for the slightly lower correlation function is that the ATreePM code does not resolve small haloes, in particular those with fewer than n_n particles (see the discussion of mass function of collapsed haloes). Indeed, the number density of small haloes is severely under-estimated in the ATreePM simulations and we believe that this is the main reason for a weaker two point correlation function.

Collapsed Haloes

We now look at another global indicator, namely the mass function of collapsed haloes, to compare the performance of the TreePM and the ATreePM codes. The number density of haloes $N(M)dM$ in the mass range $(M, M + dM)$ is plotted in Figure 3.7. Haloes were identified using the Friends-Of-Friends algorithm with a linking length $l_l = 0.1$ in grid units and haloes with at least 8 particles were considered.

For TreePM we see that as we increase the force softening length there is a clear change in the mass function. The mass function converges for all masses with $\epsilon \leq 0.2$. However, the mass function for $\epsilon = 0.5$ shows fewer haloes of up to about 10^2 particles. Thus the effect of a large softening length and hence biasing in force is seen in mass function up to fairly large mass scales. This qualitative behavior is insensitive to the choice of linking length, though the scale of convergence is smaller if we choose a larger linking length.

The ATreePM does not sample the haloes with fewer than n_n members properly. This

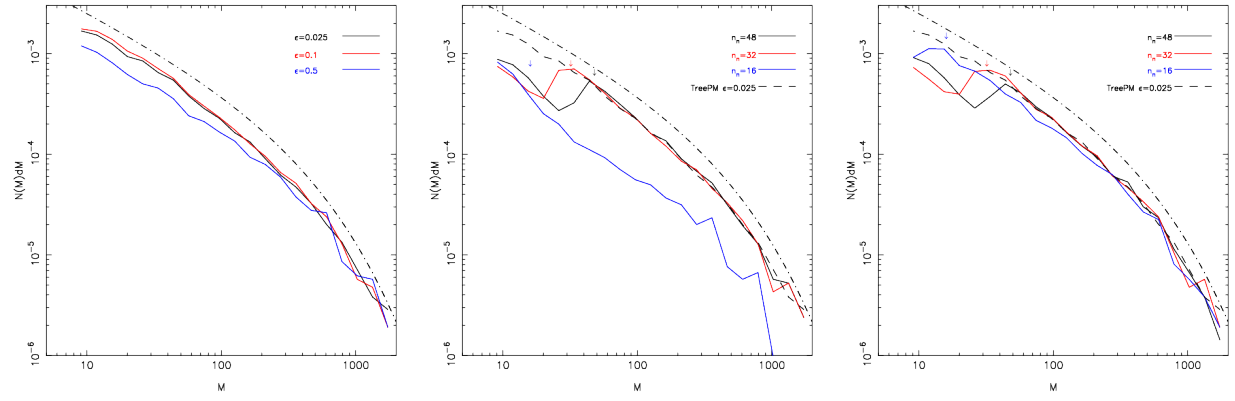


Figure 3.7: Mass function for TreePM (left), ATreePM with $\nabla\epsilon$ (middle) and ATreePM without $\nabla\epsilon$ (right). For TreePM $\epsilon = \frac{r_s}{40}, \frac{r_s}{10}, \frac{r_s}{2}$ are drawn in black, red, blue lines respectively. $n_n = 32, 48$ are drawn in black and red lines for ATreePM. The arrows represent n_n in mass units. The black dot-dashed curve on every plot is the Press-Schechter mass function, shifted vertically by multiplying by a factor of 1.5. The black dashed line in ATreePM is for TreePM with $\epsilon = \frac{r_s}{40}$

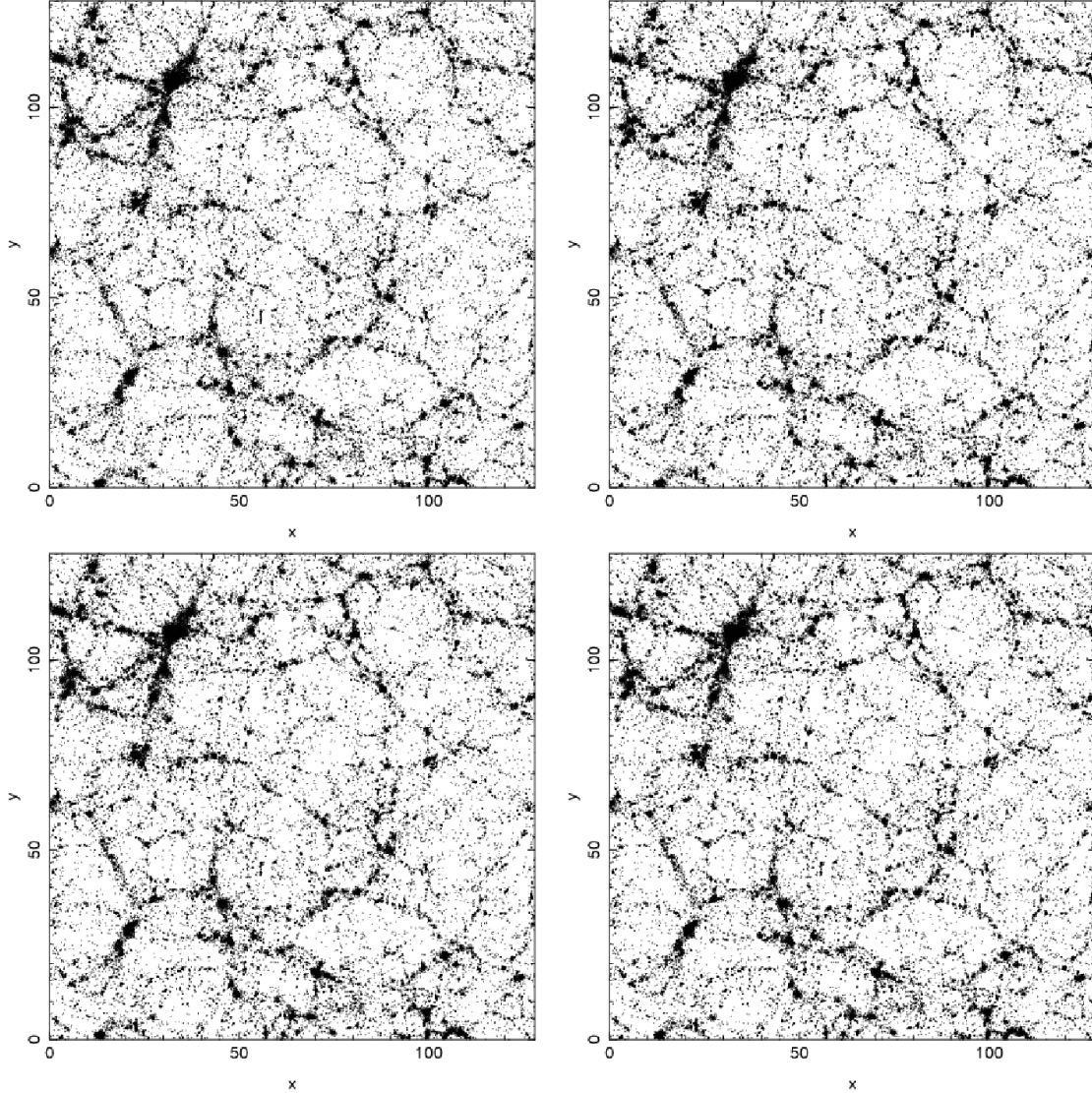


Figure 3.8: This figure shows a slice from simulation where the most massive halo resides (see top left corner). Top panel is for TreePM with $\epsilon = \frac{r_s}{40}$ (left) and ATreePM with $\epsilon = \frac{r_s}{2}$. Bottom panel is for ATreePM with $\nabla\epsilon$ (left) and ATreePM without $\nabla\epsilon$ (right). $n_n = 32$ was taken for ATreePM.

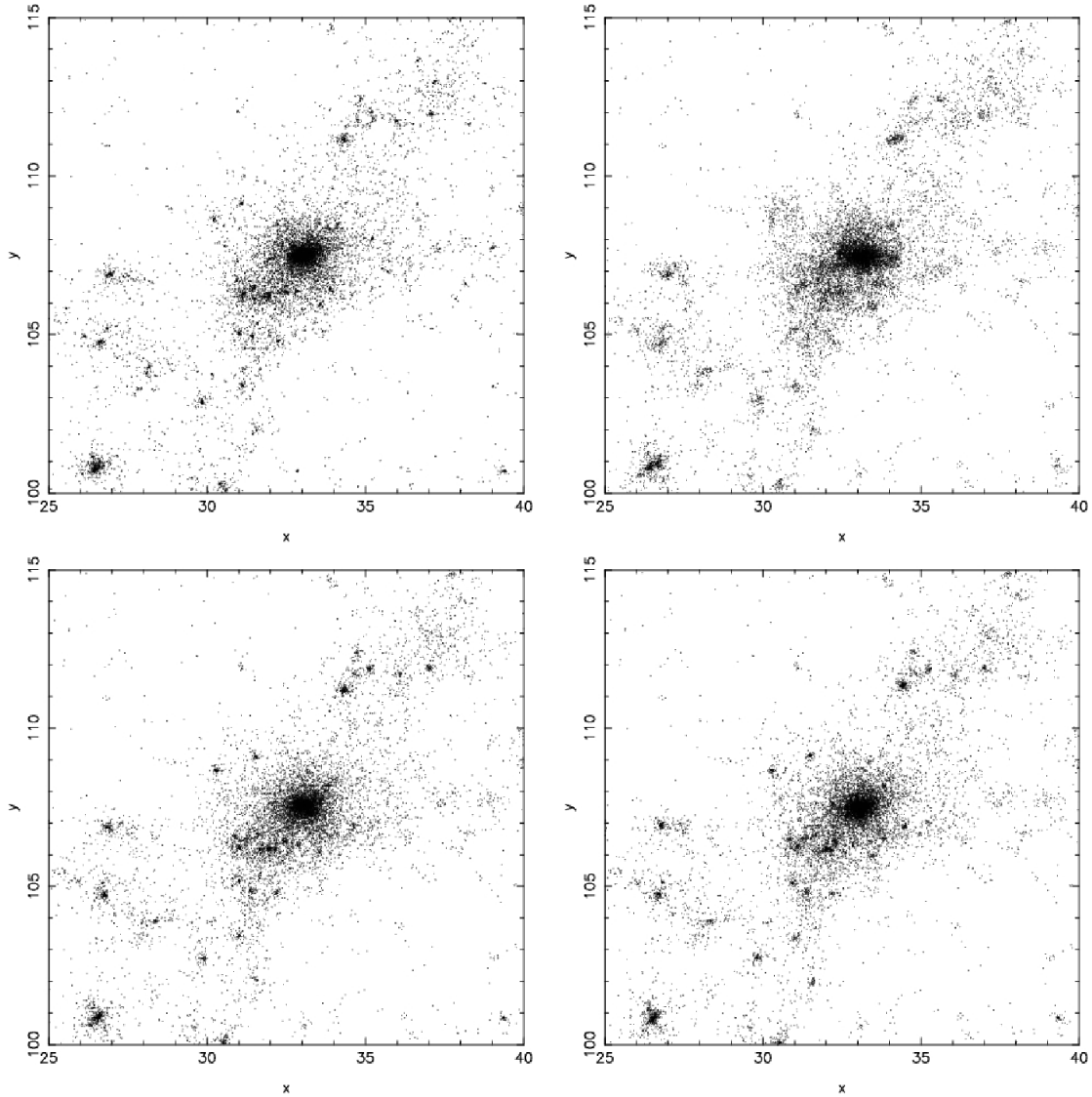


Figure 3.9: This figure is a zoom in of Fig. 3.8 and shows the region of simulation where the most massive halo resides (see top left corner of Fig. 3.8). Top panel is for TreePM with $\epsilon = \frac{r_s}{40}$ (left) and ATreePM with $\epsilon = \frac{r_s}{2}$. Bottom panel is for ATreePM with $\nabla\epsilon$ (left) and ATreePM without $\nabla\epsilon$ (right). $n_n = 32$ was taken for ATreePM.

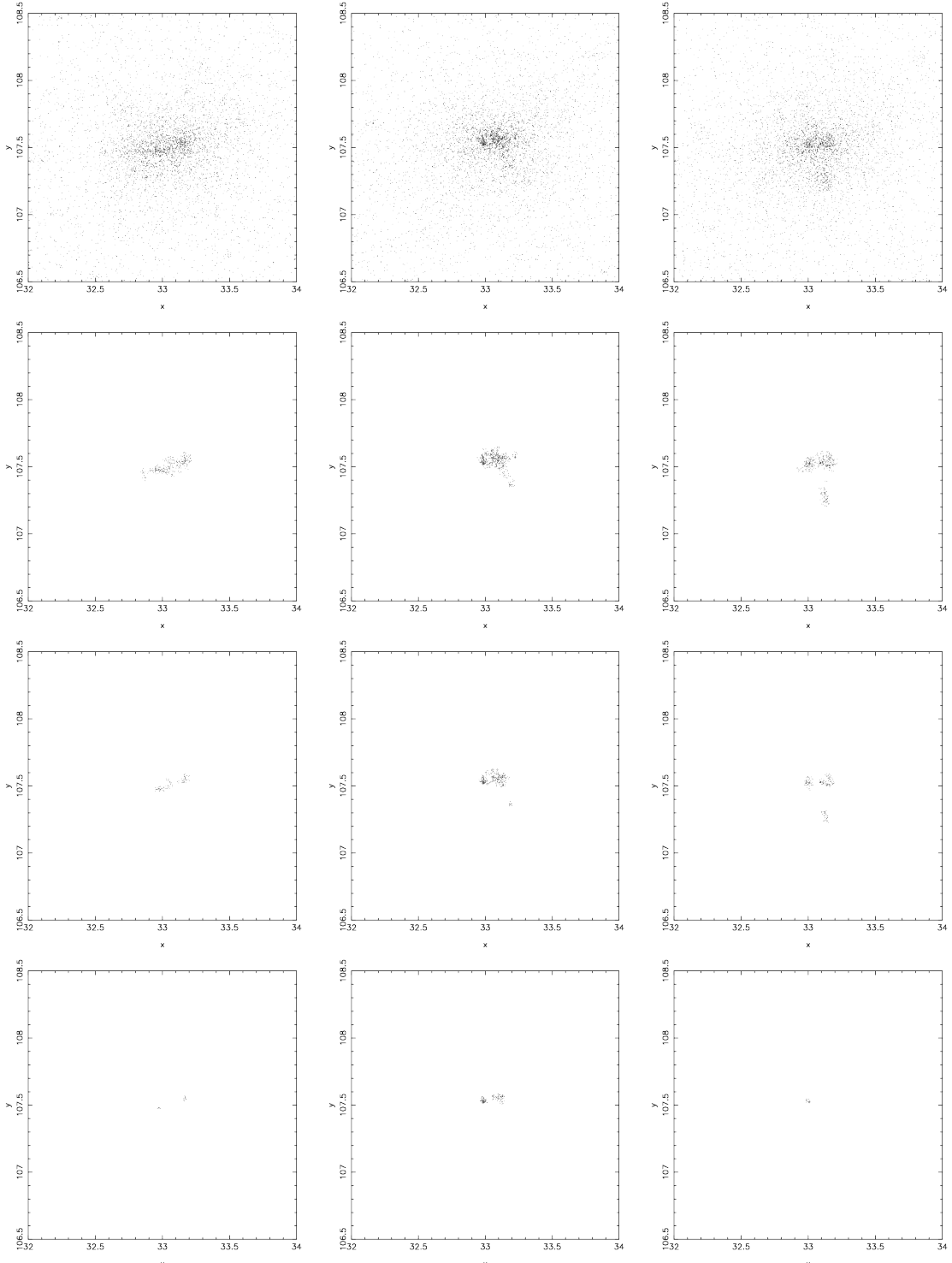


Figure 3.10: This figure shows the largest halo at $r_{nl} = 6.0$ for TreePM with $\epsilon = \frac{r_s}{40}$ (left column), ATreePM with $\nabla\epsilon$ and $n_n = 32$ (middle column) and ATreePM without $\nabla\epsilon$ and $n_n = 32$ (right column). The first row contains all the particles in the halo. The second, third and forth rows represent particles in the halo which have a density greater than 5×10^4 , 10^5 and 2×10^5 respectively.

is expected as such over-densities are not sufficient to reduce the softening length from ϵ_{max} . At larger scales we have a convergence for $n_n = 32$ and $n_n = 48$, where the mass function agrees with that for TreePM with $\epsilon = 0.025$. Mass function for $n_n = 16$ deviates significantly from the other two for ATreePM, deviation being larger for the ATreePM with the $\nabla\epsilon$ term. We believe that this is due to the noisy estimation of the force softening length and the $\nabla\epsilon$ term, and resulting errors in force.

As a reference the Press-Schechter mass function is also plotted in all three panels (black dot-dashed line). However it has been shifted up vertically by multiplying $N(M)dM$ by a factor of 1.5 for ease of comparison.

Distribution of particles in a simulation is a useful representation for comparing large scale features. The distribution of particles in a thin slice is shown in Figure 3.8. We have shown the distribution for four simulations: TreePM with $\epsilon = 0.025$ (top-left), TreePM with $\epsilon = 0.5$ (top-right), ATreePM with the $\nabla\epsilon$ term and $n_n = 32$ (lower-left) and ATreePM without the $\nabla\epsilon$ term and $n_n = 32$ (lower-right). The distribution of particles is for the last epoch, corresponding to $r_{nl} = 6$ grid lengths. This slice contains the largest halo in our simulation on the top left corner. We note that the large scale distribution is the same in all cases, indicating that the Adaptive TreePM is not changing anything at large scales.

We zoom in on the region around the largest halo in Figure 3.9, where the distribution of particles is shown from the set of simulations used in Figure 3.8. Distribution of mass at scales larger than a grid length is the same in all simulations but at small scales we begin to see some differences between the distribution of particles in different simulations. TreePM with $\epsilon = 0.5$ differs most from the other three, in that it does not resolve small scale structures. This happens due to the relatively large force softening length that inhibits collapse if the expected size of the collapsed halo is smaller than ϵ . The notable differences between the TreePM ($\epsilon = 0.025$) and the ATreePM slices are as follows:

- Small haloes in the region away from the large haloes are more compact for TreePM than for ATreePM. This is perhaps caused by the ATreePM not having a constant ϵ and it is likely that in these clumps the local value of ϵ is larger than 0.025 that is used in the TreePM.
- Location of sub-structure in the central halo differs somewhat between the different

simulations.

Figure 3.10 shows the inner regions of the halo seen in Figure 3.9. We show the inner parts of the halo in the four cases (TreePM ($\epsilon = 0.025$), ATreePM with the $\nabla\epsilon$ term ($n_n = 32$), ATreePM without the $\nabla\epsilon$ term ($n_n = 32$). The top row shows all the particles in the inner parts of the halo. The second row shows all the particles with an SPH over-density estimate (computed with $n_n = 32$ and using the kernel specified in Eqn. 3.5) of greater than 5×10^4 , the third row shows the particles with an over-density of greater than 10^5 , and, the last row shows particles with an overdensity larger than 2×10^5 . We see that the ATreePM with the $\nabla\epsilon$ term shows the most pronounced central part of the halo in the top panel, and this impression gains strength as we move to lower panels. Table 3.2 gives us the number of particles in the various panels of Fig. 3.10. TreePM with $\epsilon = 0.025$ manages to trace some of the highly over-dense substructure seen in the ATreePM simulations, though with a much smaller number of particles in these clumps. The ATreePM with the $\nabla\epsilon$ term does better than the one without, particularly at the highest over-densities used here. Indeed ATreePM with the $\nabla\epsilon$ term retains nearly 7 times as many particles in the halo core as compared to TreePM and ATreePM without the $\nabla\epsilon$ term. The same thing is also reflected in Figure 3.5 where the ATreePM without the $\nabla\epsilon$ term is seen to underestimate clustering at small scales. It is noteworthy that the size of highly over-dense structures in the core of this halo are much bigger than the force softening length for the TreePM.

It is notable that the ATreePM is able to resolve highly over-dense regions while taking much less time than the fixed resolution TreePM. Thus we have the added performance at the cost of fewer resources.

Dynamics within Collapsed Haloes

The equation of motion for the adaptive code has the additional $\nabla\epsilon$ term, and it is important to test whether this term leads to a change in dynamics in highly overdense regions. We test this by studying the dynamics in central cores of the largest haloes in the simulation. We study the ratio $\langle 2T \rangle / \langle U \rangle$ at a scale corresponding to $r_{200}/5$, with the averaging done around the centre of mass of the halo. We chose the reference scale in this manner as the density profiles for haloes with different softening length differ considerably and using

Table 3.2: This table shows the number of particles n_{part} above a density threshold (as in Figure 3.10) retained in the core of the most massive halo

Runs	n_{part} $\rho \geq 5 \times 10^4$	n_{part} $\rho \geq 10^5$	n_{part} $\rho \geq 2 \times 10^5$
TreePM ($\epsilon = \frac{r_s}{40}$)	320	106	18
ATreePM ($\nabla\epsilon, n_n = 32$)	568	297	125
ATreePM ($n_n = 32$)	374	169	18

a high density contour to define the radius leads to very different physical scales. Figure 11 shows $\langle 2T \rangle / \langle U \rangle$ as a function of softening length ϵ for the fixed resolution TreePM simulations. This has been done for the five largest haloes in the simulation. We see that as we go to a larger softening length, the ratio becomes larger than unity, indeed for $\epsilon = 0.5$ the ratio is closer to two for one of the haloes. This is likely to happen if the size of the over-dense core is comparable to the softening length, and indeed this is the case for some of the haloes used for this plot. The same plot shows the ratio as seen in the adaptive code (with the $\nabla\epsilon$ term) with empty squares, and as filled triangles for the adaptive code without the $\nabla\epsilon$ term. These circles are plotted at small values of ϵ , not used for TreePM runs. The values of ϵ used for positioning these symbols in the plot has no relevance to the simulation, and this has been done purely for the purpose of plotting the values. We see that the values for the ratio in both the adaptive codes correspond closely to the values of the ratio seen in fixed resolution TreePM simulations with a small ϵ . Thus we may conclude that the additional term in the Adaptive code is not leading to any significant changes in the dynamics, as compared to the fixed resolution codes.

3.6 Discussion

In this chapter we have introduced the first cosmological N-Body code that has a continuously varying force resolution. This is based on a well defined formalism that ensures energy

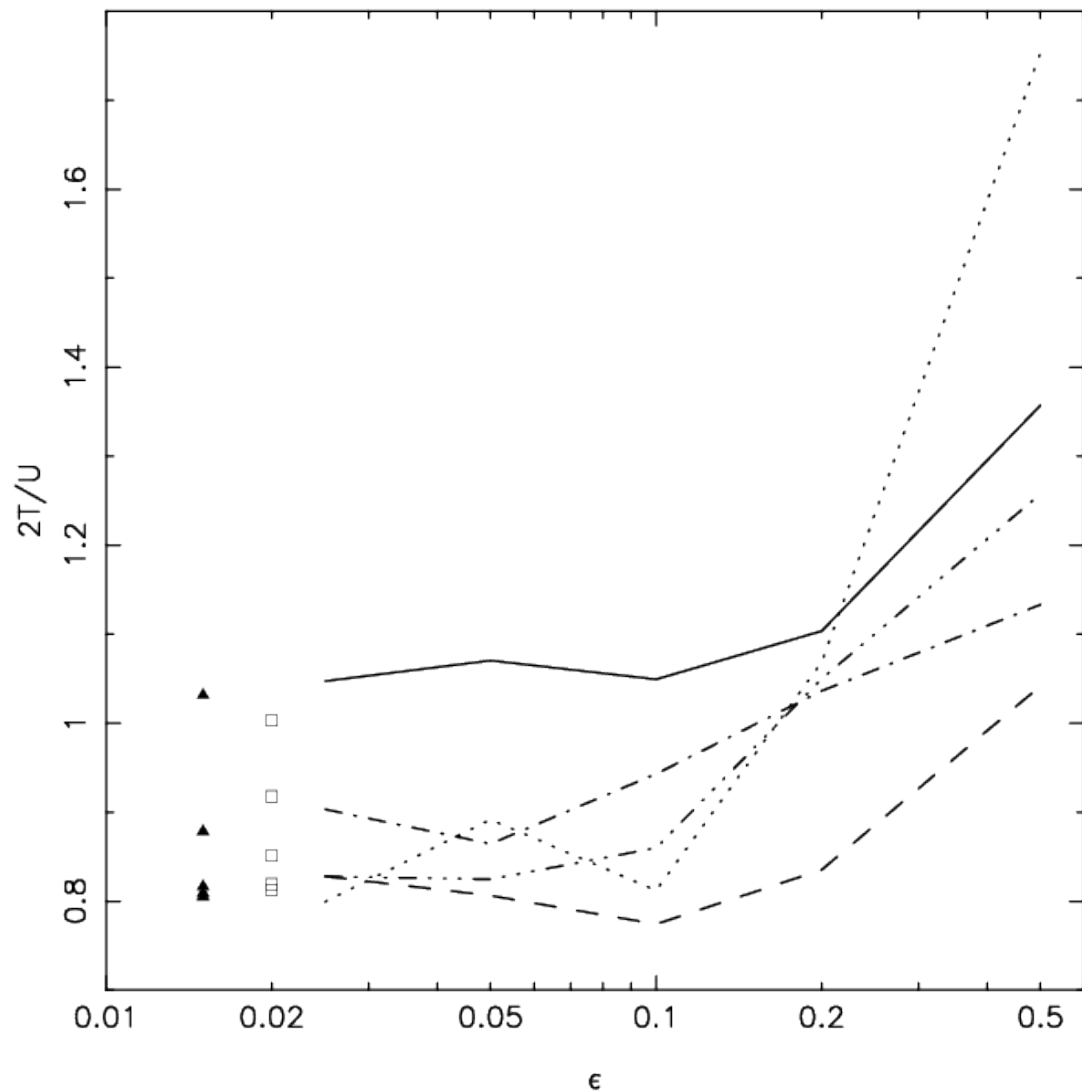


Figure 3.11: Ratio of two times the kinetic energy and the potential energy, $2T/U$, for the 5 largest haloes as a function of softening length for TreePM (black lines). Open squares and filled triangles are for ATreePM with and without $\nabla\epsilon$ respectively.

and momentum conservation. An important aspect of this formalism is that it modifies the equation of motion at scales below the force softening length. Our implementation of the formalism uses methods developed for SPH codes, this is required as we need to assign quantities like density to particles. We have described our implementation of the code in detail here. We have given a brief summary of errors in force for the Adaptive TreePM code with the new parameter n_n . Given that this code is based on the TreePM code, it inherits the errors in force with respect to all the other parameters. As we have seen in earlier work (Bagla, 2002; Bagla & Ray, 2003; Khandai & Bagla, 2009), errors in force can be minimised to a fairly low level for the TreePM with a judicious choice of parameters.

We find that the time taken by the Adaptive TreePM (for $n_n = 32$) is comparable to that taken by the fixed resolution TreePM code if the latter uses a force softening length that is about 1/20 of the mean inter-particle separation.

One of the key reasons for considering adaptive resolution is to avoid two body collisions. Cosmological simulations require collisionless evolution. We test the Adaptive TreePM by simulating collapse of an oblique plane-wave. We find that unlike the fixed resolution TreePM code that leads to large transverse motions, a clear sign of two body collisions, the Adaptive TreePM code does not have any significant transverse motions. (See Figures 3.3, 3.4)

We have compared the performance of the Adaptive TreePM with that of the fixed resolution TreePM code for power law initial conditions. We used a power law model and the Einstein-de Sitter background as it allows us to test codes by requiring self-similar evolution of the correlation function. We find that for $n_n = 32$, the resulting density distribution in the Adaptive TreePM is comparable to that seen in the highest resolution TreePM in many respects. The correlation function for the two match at all scales and the mass function of collapsed haloes matches for haloes with more than n_n particles. The Adaptive TreePM with the $\nabla\epsilon$ term in the equation of motion does much better than the TreePM as well as the Adaptive TreePM without the extra term in resolving highly over-dense cores of massive haloes. It is noteworthy that the Adaptive code takes less time than the TreePM it has been compared with (see fig. 3.1).

We have tested the codes by looking for convergence in results as we modify the key parameters that describe the force resolution. We find that the fixed resolution TreePM

code converges slower than expected from, for example, self-similar evolution of clustering. The Adaptive TreePM code with the $\nabla\epsilon$ term converges fairly quickly and offers an effective dynamical range that is slightly smaller than the fixed resolution TreePM that takes almost the same time to run.

Given our analysis of errors, and the comparison of the performance of the ATreePM code with and without the extra term in the equation of motion, the natural conclusion is that we require the extra term in order to obtain low errors and numerical convergence. This raises the obvious question about the AMR codes where no such extra term is used. Further, in most AMR codes, resolution is increased when there are of order 10 particles in the lower resolution elements. We find that the errors are minimized when this number is around 20 even when the extra term is not taken into account. It is not clear how serious these issues are, given that AMR codes have been developed and tested in a variety of ways over the last three decades, but it is a concern⁶.

We have established in this chapter that an adaptive resolution code for evolution of perturbations in collisionless dark matter can give reliable results for a range of indicators from clustering properties to mass function of collapsed haloes and even get the internal dynamics of collapsed haloes tight. Further, we show that such a code is efficient in that it is faster than fixed resolution codes that give us comparable force resolution in highly over dense regions. Such a code is very useful as it allows us to probe clustering at small scales in a reliable manner. Studies of box-size effects have shown that large simulation boxes are required in order to limit the effect of perturbations at larger scales that are not taken into account (Bagla & Prasad, 2006; Bagla, Prasad, & Khandai, 2009). In such a situation an adaptive code provides us with a reasonable range of scales over which the results can be trusted. We expect to use this code to address several issues related to gravitational clustering in an expanding universe. We also plan to revisit issues related to density profiles of collapsed haloes.

Given the conclusions listed above, we feel that the Adaptive TreePM methods rep-

⁶One aspect where AMR codes do relatively poorly is in getting the halo mass function at the low mass end (O’Shea et al., 2005; Heitmann et al., 2008). As one can see in figures in the papers cited here, the shortfall is often spread over a decade in mass of haloes. We do not see any gradual decline in the number density of haloes in ATreePM up to the cutoff set by n_n .

resents an exciting development where we can set aside worries about the impact of collisionality. The relative speed of the adaptive code also makes this a more pragmatic option.

Chapter 4

Mass function of haloes: scale invariant models

Press-Schechter theory gives a simple, approximate functional form of the mass function of dark matter haloes. Sheth and Tormen (ST) refined this mass function to give an improved analytical fit to results of N -body simulations. These forms of the halo mass function are universal (independent of cosmology and power spectrum) when scaled in suitable variables. Using large suites of LCDM N -body simulations, studies in the last few years have shown that this universality is only approximate. We explore whether some of the deviations from universality can be attributed to the power spectrum by computing the mass function in N -body simulations of various scale-free models in an Einstein-de Sitter cosmology. This choice of cosmology does not introduce any scale into the problem. These models have the advantage of being self-similar, hence stringent checks can be imposed while running these simulations. This set of numerical experiments is designed to isolate any power spectrum dependent departures from universality of mass functions. We show explicitly that the best fit ST parameters have a clear dependence on power spectrum. Our results also indicate that an improved analytical theory with more parameters is required in order to provide better fits to the mass function.

4.1 Introduction

The halo mass function describes number density of dark matter haloes of a given mass in a given cosmology, and is an essential input for a diverse set of tools used for making theoretical predictions. The halo model of large scale structure, for example, is based on the theory of mass functions (Cooray & Sheth, 2002). Accurate knowledge of the mass function is important for several cosmological applications, including semi-analytic theories of galaxy formation (White & Frenk, 1991); constraints on cosmological parameters using galaxy cluster abundance (Majumdar & Mohr, 2003), gravitational lensing (Bartelmann et al., 1998) and constraints on non-Gaussianity in the primordial power spectrum (Bartolo, Matarrese, & Riotto, 2005) of matter perturbation.

It is possible to develop the theory of mass functions in a manner that makes no reference to the details of the cosmological model or the power spectrum of fluctuations. That is, we expect the mass function to take a universal form, when scaled appropriately. Simple theoretical arguments have been used to obtain this universal functional form of the mass function (Press & Schechter, 1974; Bond et al., 1991; Sheth, Mo, & Tormen, 2001). Bond et al. (1991) and Sheth, Mo, & Tormen (2001) used the excursion set theory to derive the mass function. Much work has also been done to determine the extent to which this form is consistent with results from N-body simulations (Jenkins et al., 2001; White, 2002; Reed et al., 2003; Warren et al., 2006; Reed et al., 2007; Lukić et al., 2007; Cohn & White, 2008; Tinker et al., 2008) with the conclusion that the agreement is fairly good. Recent comparisons with very large N-Body simulations also provide hints that the form of the mass function is not universal.

The Press-Schechter mass function (Press & Schechter, 1974) is based on the spherical collapse model (Gunn & Gott, 1972) and the ansatz that the mass in collapsed objects is related to the volume with density above a certain threshold. The shape of the mass function agrees with numerical results qualitatively: at a quantitative level there are deviations at the low mass and the high mass ends (Efstathiou et al., 1988; Jenkins et al., 2001). Improvements to the Press-Schechter mass function have been made to overcome this limitation. In particular, the Sheth-Tormen mass function is based on the more realistic ellipsoidal collapse model (Sheth & Tormen, 1999; Sheth, Mo, & Tormen, 2001) and

it fits numerical results better. These mass functions relate the abundance of haloes to the initial density field in a universal manner, independent of cosmology and power spectrum. Many fitting functions with three or four fitting parameters have been proposed. These are based on results of simulations of the LCDM model (Jenkins et al., 2001; Reed et al., 2003; Warren et al., 2006).

In the last few years, large N-Body simulations of the LCDM model have demonstrated that the mass function is not universal (White, 2002), and epoch dependent fitting functions have been given for this model (Reed et al., 2007; Tinker et al., 2008). The results of Lacey & Cole (1994) also show a small dependence of the mass function on the power spectrum but given the size of simulations these deviations are small. These studies show non-universality by noting variations in the form of mass function with redshift or cosmology in successively larger simulations that explore a large range in mass. Much of the numerical work in this area during the last decade has focused on the LCDM model, it being the model favored by observations.

It is expected that this non-universality is a result of variation of mass function parameters either with cosmology or with the power spectrum or both. Cosmology dependence is introduced by the variation in the threshold density for collapse (Barrow & Saich, 1993). The CDM class of models have a power spectrum of density fluctuations with a gradually varying slope or the spectral index, $n(k)$, which decreases with decreasing scale (increasing wavenumber k). As perturbations at smaller scales collapse earlier, the effective index of the power spectrum is small at early times and increases towards late times. The threshold overdensity for collapse also changes as the cosmological constant becomes more important at late times. Thus the variation in mass function may be due to the shape of the power spectrum, or cosmology, or both. This makes the published results difficult to interpret in terms of a theoretical model. It is then hard to discern any trends in non-universality that will potentially provide a physical understanding. Given the number of applications of the theory of mass function like computation of merger rates, halo formation rates, etc., it is essential to develop a clear understanding of the origin of non-universality. The only other option is to work with fitting functions for each of these quantities derived from N-Body simulations.

The problem of an unclear origin of deviations of universality can be partially ad-

dressed by studying a wider variety of models in the CDM class of models. This approach has been taken by, for example, Neistein, Maccio, & Dekel (2009) in the context of universality in halo mergers. The effect of perturbations at larger scales in terms of the tidal field, which is relevant for ellipsoidal collapse, also changes with time due to the variation in the slope of the power spectrum with scale. Given that the tidal field is generated by larger scales, it is not very clear whether a prescription based on the local index of the power spectrum alone can provide a detailed explanation for the mass function. Since the CDM spectra lack the simplicity of the scale-free spectra, we approach this problem differently. We specifically look for departures from non-universality in the mass function for scale-free power spectra of initial fluctuations with an Einstein-de Sitter background to check if the non-universal description can be attributed to a spectrum dependence. Our choice of cosmology does not introduce any scale in the problem and the threshold overdensity does not vary with time in any non-trivial manner. Thus we can isolate the non-universality of mass functions arising from the slope of the power spectrum. We provide spectrum dependent fits for the parameters in the Sheth-Tormen mass function, and show that this allows us to fit simulation data much better.

We start with a discussion of the basic framework of mass functions in §4.2, where we also set up the notation. Our numerical simulations are described in §4.3. We present our analysis of the data in §4.4 along with the results. A discussion of their implications appears in §4.5 and we summarize our conclusions in §4.6.

4.2 The Mass Function

In chapter 1 we had introduced the mass function which is described by the following function in the Press-Schechter formalism:

$$f(\nu) = \sqrt{\frac{2}{\pi}} \nu \exp(-\nu^2/2) \quad (4.1)$$

where $\nu = \delta_c / (\sigma(M)D_+(z))$. Here δ_c is the threshold overdensity for a spherically symmetric perturbation, above which it collapses and forms a virialised halo. It has only a weak dependence on cosmology and its value is 1.69 for $\Omega_0 = 1$ (Gunn & Gott, 1972; Peebles,

1980). Fitting functions that describe the dependence of δ_c on cosmology are available (Barrow & Saich, 1993; Eke, Cole, & Frenk, 1996; Navarro, Frenk, & White, 1996; Nakamura & Suto, 1997; Bryan & Norman, 1998; Henry, 2000). We take the value of 1.686 throughout our analysis as we are working with the Einstein-de Sitter cosmology.

The *rms* fluctuations of the linearly evolved density field at present is denoted by $\sigma(M)$, smoothed with a spherical top hat filter enclosing mass m and is calculated by convolving the linear density power spectrum $P(k)$, extrapolated to the current epoch, with the filter $W(k, M)$. In what follows we modify our notation slightly from those introduced in chapter 1, we will treat the arguments r and M interchangeably in the mass variance, i.e. $\sigma(r) \equiv \sigma(M)$.

$$\sigma^2(M) = \int_0^\infty \frac{dk}{k} \frac{k^3 P(k)}{2\pi^2} W^2(k, M). \quad (4.2)$$

$D_+(z)$ is the growth function (Heath, 1977). All mass is contained in haloes in this formalism, this provides the normalization:

$$\int_0^\infty \frac{1}{\nu} f(\nu) d\nu = 1 \quad (4.3)$$

This mass function is related to the number of haloes of a given mass per unit comoving volume by

$$\frac{dn}{d \ln M} = \frac{\bar{\rho}}{M} \frac{d \ln \sigma^{-1}}{d \ln M} f(\nu). \quad (4.4)$$

The dependence on cosmology and power spectrum is absorbed in ν , and the theory of mass functions can be developed without reference to the detailed dependence of ν on the power spectrum or cosmology, so we expect the form of Equation (4.1) to be universal.

The Sheth-Tormen mass function is a modification to the Press-Schechter model and is based on ellipsoidal collapse instead of spherical collapse. It has been shown to reproduce simulation results better.

$$f(\nu) = A \sqrt{\frac{2q}{\pi}} [1 + (q\nu^2)^{-p}] \nu \exp(-q\nu^2/2). \quad (4.5)$$

Clearly, this is also a universal form.

Table 4.1: Details of N -body simulations used in this work.

n	N_{box}	N_{part}	r_{nl}^i	r_{nl}^f	r_{nl}^{\max}	z_i
-2.5	512^3	512^3	0.2	1.0	0.1	36.21
-2.2	512^3	512^3	0.5	2.0	2.0	51.23
-2.0	512^3	512^3	1.0	4.5	4.2	62.80
-1.8	512^3	512^3	2.5	9.0	8.5	78.82
-1.5	400^3	400^3	2.5	12.0	10.0	103.38
-1.0	400^3	400^3	2.5	10.0	22.2	171.52
-0.5	256^3	256^3	2.5	12.0	18.2	291.53
+0.0	256^3	256^3	2.5	12.0	21.2	470.81

4.3 Numerical Simulations

We run a suite of models with a power law power spectrum ($P(k) = Ak^n$) of initial fluctuations, in the range $-2.5 \leq n \leq 0.0$. We use the Einstein-de Sitter cosmological background where the growing mode of perturbations $D_+(t)$ is the same as the scale factor $a(t)$. We used the TreePM code (Khandai & Bagla, 2009) for these simulations. The TreePM (Bagla, 2002; Bagla & Ray, 2003) is a hybrid N-Body method which improves the accuracy and performance of the Barnes-Hut (BH) Tree method (Barnes & Hut, 1986) by combining it with the PM method (Miller, 1983; Klypin & Shandarin, 1983; Bouchet, Adam, & Pellat, 1985; Bouchet & Kandrup, 1985; Hockney & Eastwood, 1988; Bagla & Padmanabhan, 1997; Merz, Pen, & Trac, 2005). The TreePM method explicitly breaks the potential into a short-range and a long-range component at a scale r_s : the PM method is used to calculate long-range force and the short-range force is computed using the BH Tree method. Use of the BH Tree for short-range force calculation enhances the force resolution as compared to the PM method.

The mean interparticle separation between particles in the simulations used here is $l_{\text{mean}} = 1.0$ in units of the grid-size used for the PM part of the force calculation. In our

notation this is also cube root of the ratio of simulation volume N_{box}^3 to the total number of particles N_{part} .

Power law models do not have any intrinsic scale apart from the scale of non-linearity introduced by gravity. We can therefore identify an epoch in terms of the scale of non-linearity r_{nl} . This is defined as the scale for which the linearly extrapolated value of the mass variance at a given epoch $\sigma_L(a, r_{nl})$ is unity. All simulations are normalized such that $\sigma^2(a = 1.0, r_{nl} = 8.0) = 1.0$. The softening length in grid units is $\epsilon = 0.03$ in all runs.

Simulations introduce an inner and an outer scale in the problem and in most cases we work with simulation results where $L_{\text{box}} \gg r_{nl} \geq L_{\text{grid}}$, where L_{grid} , the size of a grid cell is the inner scale in the problem. L_{box} is the size of the simulation and represents the outer scale.

Finite volume effects can lead to significant errors in N-Body simulations since modes greater than the size of the box are ignored while generating initial conditions and during evolution (Bagla & Ray, 2005; Bagla & Prasad, 2006; Power & Knebe, 2006; Bagla, Prasad, & Khandai, 2009). The errors in the mass variance and hence most descriptors of clustering can become arbitrarily large as the index of the power spectrum n approaches -3.0 . The prescription provided by Bagla & Prasad (2006) and Bagla, Prasad, & Khandai (2009) can be used to find the regime where the results of a simulation are reliable at a given level of tolerance. We require that the error in σ^2 be less than 3% at the scale of non-linearity. This requirement severely restricts the level of non-linearity that can be probed in simulations with indices $n = -2.5, -2.2$ and -2.0 amongst the set of models we use here. We will use these simulations mainly to illustrate the severity of finite box size effects and compare the mass function obtained in the simulations with our expectations, but we do not use these simulations for an explicit determination of the mass function. In Table (5.2) we list the power law models simulated for the present study. We list the index of the power spectrum n (column 1), size of the simulation box N_{box} (column 2), number of particles N_{part} (column 3), the scale of non-linearity at the earliest epoch used in this study (column 4), and, the maximum scale of non-linearity, r_{nl}^{\max} (column 6) given our tolerance level of 3% error in the mass variance at this scale. For some models with very negative indices we have run the simulations beyond this epoch. This can be seen in column 5 where we list the actual scale of non-linearity for the last epoch.

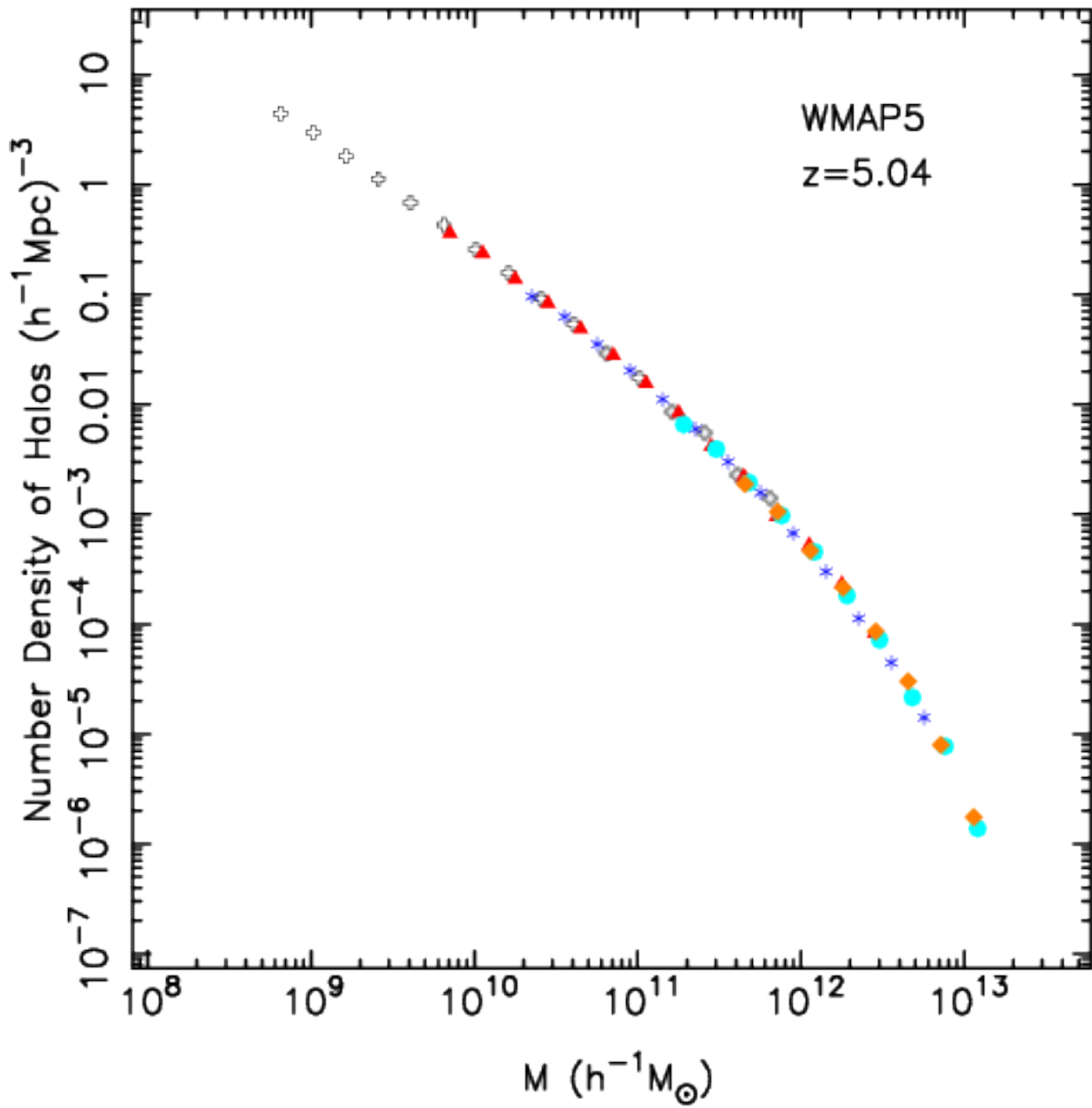


Figure 4.1: Mass functions at $z = 5.04$ from our LCDM (WMAP5) simulations for different simulation boxes. Black, red, blue, pale blue and ochre are for $L_{box} = 23.04, 51.2, 76.8, 153.6, 204.8 h^{-1}\text{Mpc}$ respectively.

In the next section we describe a procedure to put an upper limit on the high mass bins since in these haloes counts are reduced due to finite boxsize considerations, especially at late times. The counts of haloes in low mass bins are relatively unaffected by finite box considerations. We therefore limit errors in the mass function by running the simulation up to r_{nl}^{max} . Column 7 lists the starting redshift of the simulations for every model.

Models with a large slope of the power spectrum have more power at small scales and the relative amplitude of fluctuations at small scales is large. Care is required for running simulations of these models as small scales become non-linear at early times the r_{nl} grows very slowly with the scale factor. A very large number of time steps are required in order to evolve the system to epochs with a large r_{nl} . We require that the evolution of the two point correlation function $\bar{\xi}$ (Peebles, 1980) be strictly self-similar in the range of epochs where we use the simulation data. This allows us to verify the correctness of evolution. As a test of our simulation code we have run a set of LCDM (WMAP5) simulations for different boxes. We have computed the number density of haloes in our simulations at redshift $z = 5.04$. This is shown in figure 4.1. We find that the points from different boxes lie on a single curve, as expected.

4.4 Analysis and Results

We use the Friends-of-Friends (FOF) (Davis et al., 1985) algorithm with a linking length $l = 0.2$ to identify haloes and construct a halo catalog. In order to avoid spurious identification of haloes and also discreteness noise, we do not use haloes with a small number of particles — only haloes with more than 60 particles are used in our analysis.

Given the halo catalog one can compute the mass function by first binning the haloes in mass bins. We constructed logarithmic bins in mass with size $\Delta \log m = 0.2$. Given the halo count per logarithmic mass bin $dn/d\log m$ and using the fact that $\bar{\rho} = 1$, we write Equation 4.4

$$f(\nu) = \frac{6}{n+3} \frac{M}{\bar{\rho}} \frac{dn}{d\ln M} \quad (4.6)$$

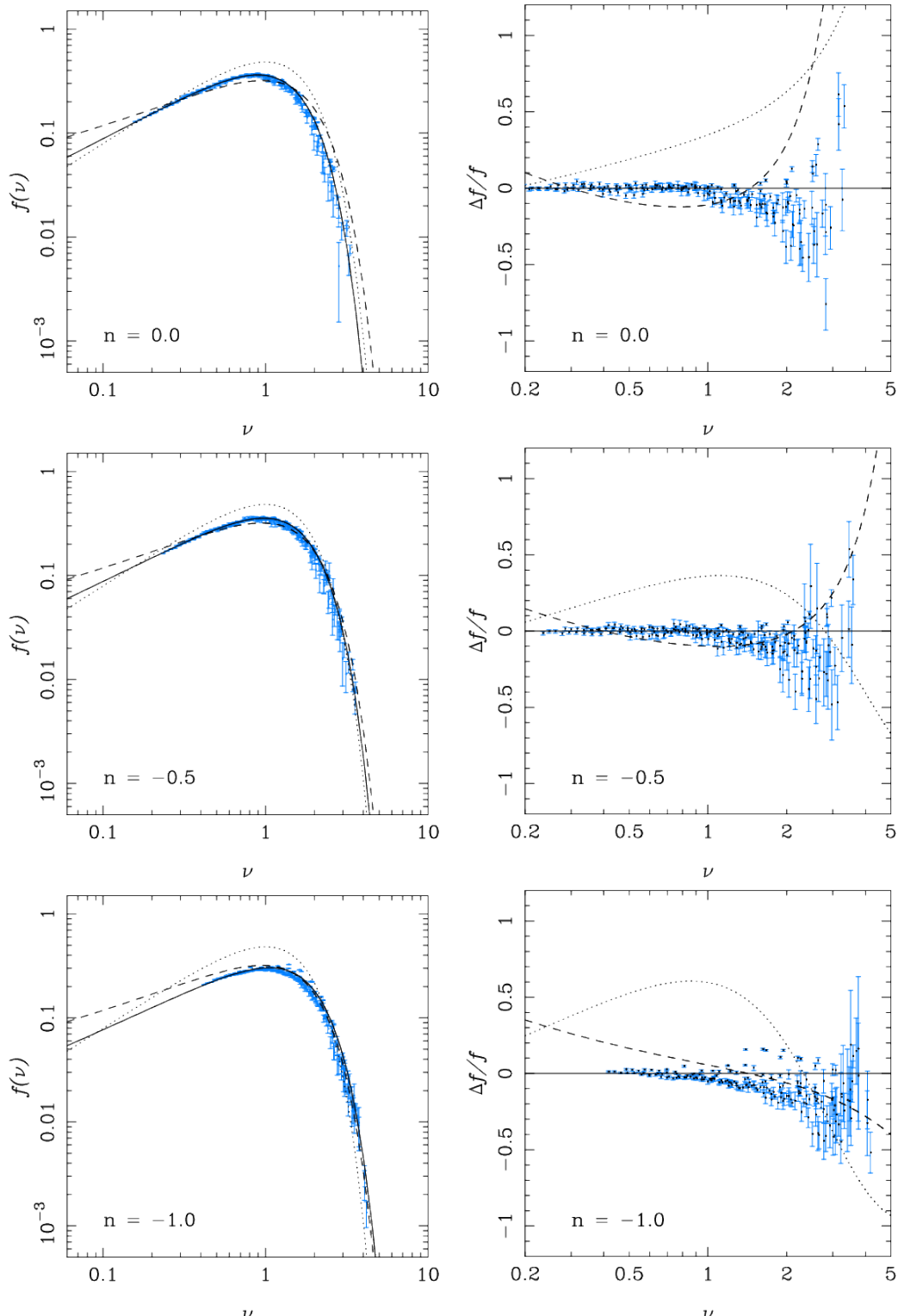


Figure 4.2: Mass functions from our simulations (left column) and their residuals after fitting a ST form (right column). Rows 1, 2 and 3 are for indices $n = 0.0, -0.5, -1.0$. Solid black line is our best fit ST curve. Dashed line and dotted line show the standard ST and PS curves respectively.

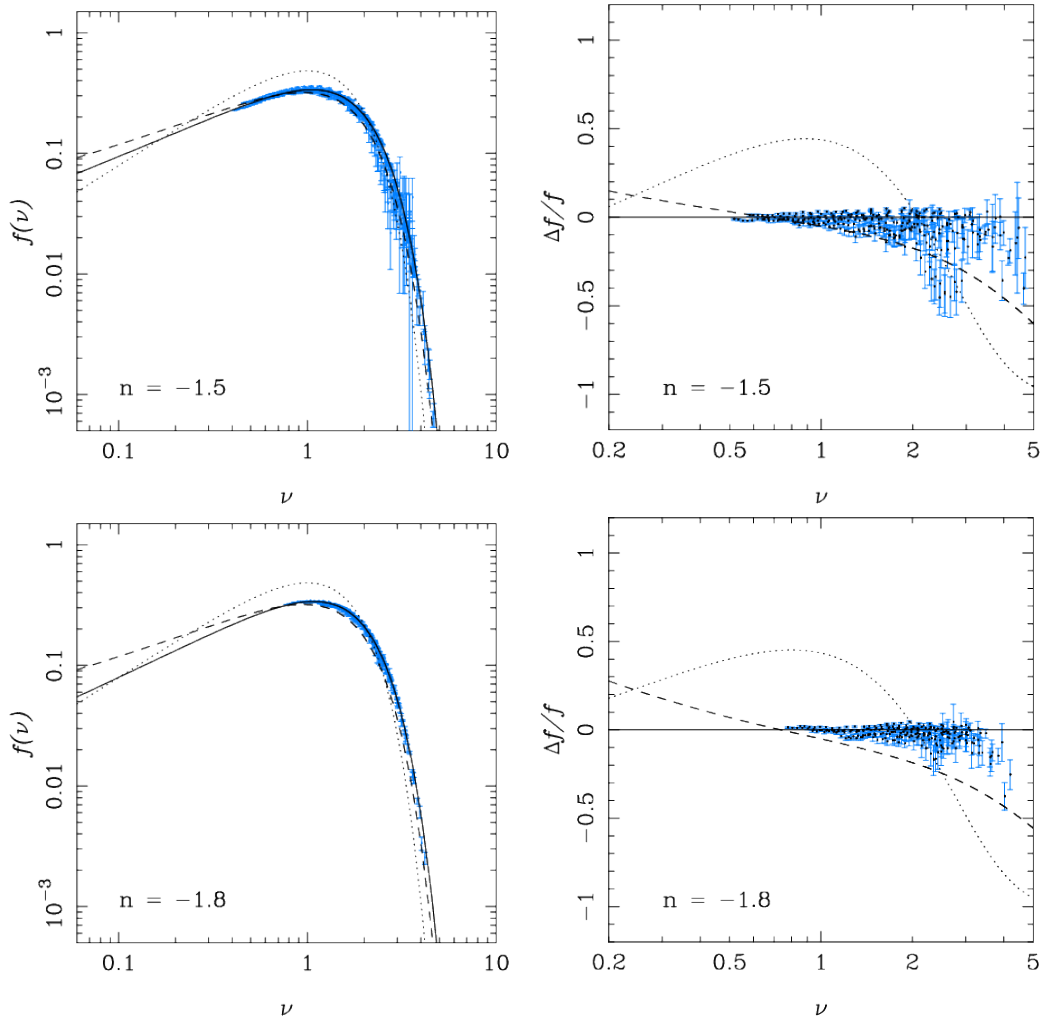


Figure 4.3: Same as Figure (4.2) for indices $n = 1.5$ (top), and -1.8 (bottom).

with $\nu = \delta_c/a\sigma(M)$. For a power law power spectrum, we have

$$\sigma(M) = \left(\frac{M}{M_{nl}}\right)^{-(n+3)/6} \quad (4.7)$$

where $m = 4\pi r^3/3$, and we take $r_{nl}(z=0) \equiv 8.0$. Note that Equation (4.7) tells us that it is much easier to probe the small ν end of the mass function with larger indices. The scale of non-linearity evolves as $r_{nl} \propto D_+^{2/(n+3)} = a^{2/(n+3)}$, where the second equality follows for the Einstein-de Sitter universe.

We choose to fit the Sheth-Tormen mass function of Equation (4.5) to our data by the method of χ^2 minimization. The correspondence with the mass function for ellipsoidal collapse makes the Sheth-Tormen mass function physically motivated. The usefulness of this approach is that the best fit values can potentially be used to compute merger rates, etc. This however may not be the best choice of the functional form of the mass function and we comment on it in the following discussion. The ST mass function has two free parameters, which we denote by p and q . The condition that all mass must be in haloes provides normalization for this function (Equation (4.4)). This gives

$$A = 1 + \frac{2^{-p}\Gamma(0.5-p)}{\sqrt{\pi}} \quad (4.8)$$

as a function of p (Cooray & Sheth, 2002).

We assume Poisson errors for counts of haloes in a mass bin. As discussed before, the effect of a finite volume simulation volume suppresses the count of haloes in the large mass end. One can either correct it (Reed et al., 2007, 2009) or remove these points from the χ^2 analysis. Correcting for these points is a tricky issue since it assumes an a priori knowledge of the mass function, the quantity which is being constructed. One can however follow an iterative procedure by first starting out with the standard ST mass function or the Press-Schechter mass function, then use it to correct the counts at the large mass end of the mass function and then do the χ^2 analysis to compute a better ST mass function and repeat the exercise all over again until one obtains a reasonable convergence in the fit. As we shall see, the dispersion and the goodness of fit does not warrant this approach and in this paper we choose to remove points affected by more than 10% in counts (as estimated for PS counts) due to box size effects.

Table 4.2: Best fit parameters of Sheth-Tormen mass function

n	p	q	χ^2_{red}	p^{new}	q^{new}	$\chi^2_{\text{red}}^{(\text{new})}$
0.0	0.141	1.065	4.933	—	—	—
-0.5	0.172	0.861	3.24	—	—	—
-1.0	0.201	0.712	31.31	—	—	—
-1.5	0.199	0.698	4.87	0.232	0.684	5.64
-1.8	0.181	0.698	4.760	0.250	0.677	6.23
-2.0	—	—	—	0.262	0.677	3.94
-2.2	—	—	—	0.274	0.698	4.56

We begin by fitting the ST mass function to the indices $n = 0.0, -0.5, -1.0, -1.5$ and -1.8 . The raw mass function, i.e., data points, and the best fit ST curve is plotted in the left column of Figures (4.2) and (4.3). The right hand column shows the residuals with respect to the best fit mass function. We also show the PS and the standard ST mass functions in each panel. Table (4.2) shows the best fit values of p and q and the reduced χ^2_{red} .

4.5 Discussion

At the outset a visual inspection of Figure (4.2) shows a clear trend in the shape of the mass function with index n of the power spectrum. We also see that the evolution is self-similar across different epochs for all indices. This is as expected for power law models in Einstein-de Sitter background.

In Figures (4.2) and (4.3) we find that for the more negative indices $n = -1.8, -1.5, -1.0$ we have a smaller dynamic range in ν as compared to $n = -0.5, 0.0$. This is expected given that we have not evolved simulations with these indices over large range of epochs due to finite boxsize considerations. Since the slope of $f(\nu)$ at the small ν end is related

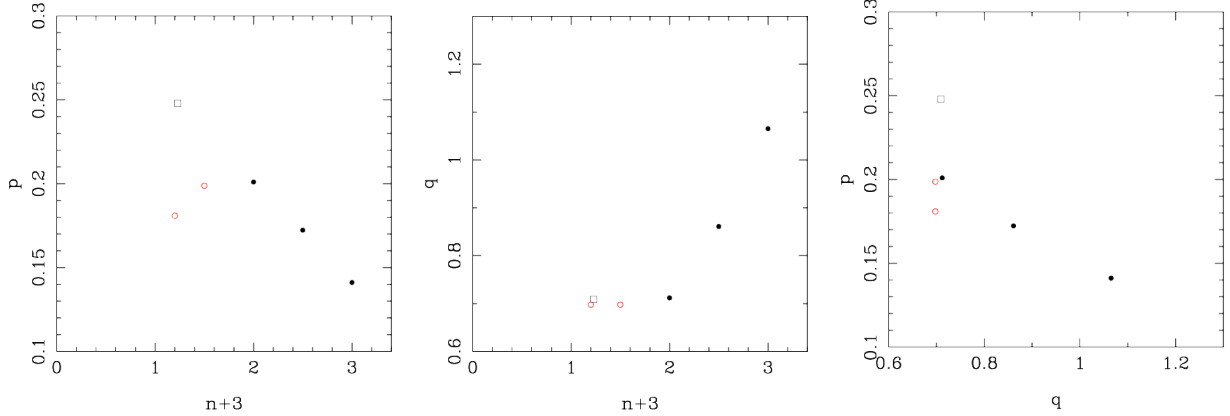


Figure 4.4: Relation between Sheth-Tormen parameters and the index n of the power law power spectrum. Red circles denote data with smaller range in ν . The square denotes the value of Manera, Sheth, & Scoccimarro (2009). See text for details.

to p — it is $f(\nu) \propto \nu^{1-2p}$ as $\nu \rightarrow 0$ — one cannot trust these results as much as the results with $n = -0.5$ and 0.0 which probe $f(\nu)$ out to much smaller values in ν . The best fit values of (p, q) and χ^2_{red} are shown in columns 2, 3 and 4 of Table 4.2 for every model (column 1). Surprisingly χ^2_{red} is relatively low for all indices as compared to the index $n = -1.0$. Part of this is due to several outliers for the $n = -1.0$ spectrum which have more than 10σ deviations. Removing these points we find that $\chi^2_{red} = 11.3$ from the original value of $\chi^2_{red} = 31.6$. The corresponding values of (p, q) changes to $(p, q) = (0.22, 0.73)$ from $(p, q) = (0.20, 0.71)$. In Figure (4.4) we also add the best fit value of p and q from the recent work of Manera, Sheth, & Scoccimarro (2009), which used 49 realizations of an LCDM simulation with 640^3 particles in a box of side $L_{\text{box}} = 1280h^{-1}\text{Mpc}$. We identify the effective index at $z = 0$, by computing

$$\left. \frac{d \log \sigma(M)}{d \log M} \right|_{\sigma=1} = -\frac{(n_{eff} + 3)}{6} \quad (4.9)$$

Next we look at the dependence of the two ST parameters (p, q) on the index of the spectrum n and also their interdependence. In Figure (4.4) we find that all the trends seen between p, q and n (n_{eff} for LCDM) are smooth when one considers the LCDM model and the power law models with indices $n = 0.0, -0.5, -1.0$. We find that the relation between

p and n is approximately

$$p(n) \simeq -0.0605 n + 0.141 \quad (4.10)$$

The trends in these parameters show deviations when one adds the models $n = -1.5$ and -1.8 , especially in the values of p ; deviations in q are not as drastic. However if we use Equation (4.10) and fix p for the indices $n = -1.5, -1.8$ and redo the χ^2 analysis to fit q then the χ^2 does not change much, thereby corroborating our argument that the values of p for the models $n = -1.5, -1.8$ are unreliable due to the small range in ν . The new values of $p^{\text{new}}, q^{\text{new}}, \chi_{\text{red}}^{2(\text{new})}$ are listed in columns 5-7 of Table (4.2). Figures (4.5 and 4.6) plots the best fit ST curve using the extrapolated value of p for the models $n = -1.5, -1.8, n = -2.0$ and -2.2 . Since we have not probed highly non-linear scales for these models the range of ν is even more limited, so much so that a full χ^2 minimization for (p, q) is futile. We therefore do not list the best fit values of (p, q) in Table (4.2) and proceed to do a similar fitting using Equation (4.10) for the models $n = -2.0, -2.2$ and find that $\chi_{\text{red}}^{2(\text{new})}$ is in the same range as for other models. The values $p^{\text{new}}, q^{\text{new}}, \chi_{\text{red}}^{2(\text{new})}$ for these models are given in columns 5-7 of Table (4.2). Again we find that the $\chi_{\text{red}}^{2(\text{new})}$ is reasonable giving credence to the extrapolation of Equation (4.10).

However the trend between p, q and n_{eff} is reversed when we compare with the LCDM runs of Manera, Sheth, & Scoccimarro (2009). Here p decreases and q increases with increasing redshift (increasing n_{eff}), at $z = 0.5$. However at this redshift, Ω_Λ has a dominant role thereby making a simple interpretation difficult. We are carrying out a series of numerical experiments where we simulate power law models in a background cosmology with a cosmological constant to develop further understanding of this issue.

Warren et al. (2006) reported a reduced $\chi_{\text{red}}^2 \sim 5$ for the Sheth-Tormen mass function with their data. Our values of χ_{red}^2 are similar and confirm that the Sheth-Tormen mass function is inadequate in fitting the data in power law models.

The Sheth-Tormen parameters also show a clear dependence on the index of the spectrum. One approach of alleviating this problem would be to better model barrier shape using simple models like the ones we have here. These can then be used to construct and compare with more complicated barriers arising due to different cosmology and a scale dependant index like the CDM class of models. The other approach can be purely phenomenological: one can use results from simpler models like those studied here and under-

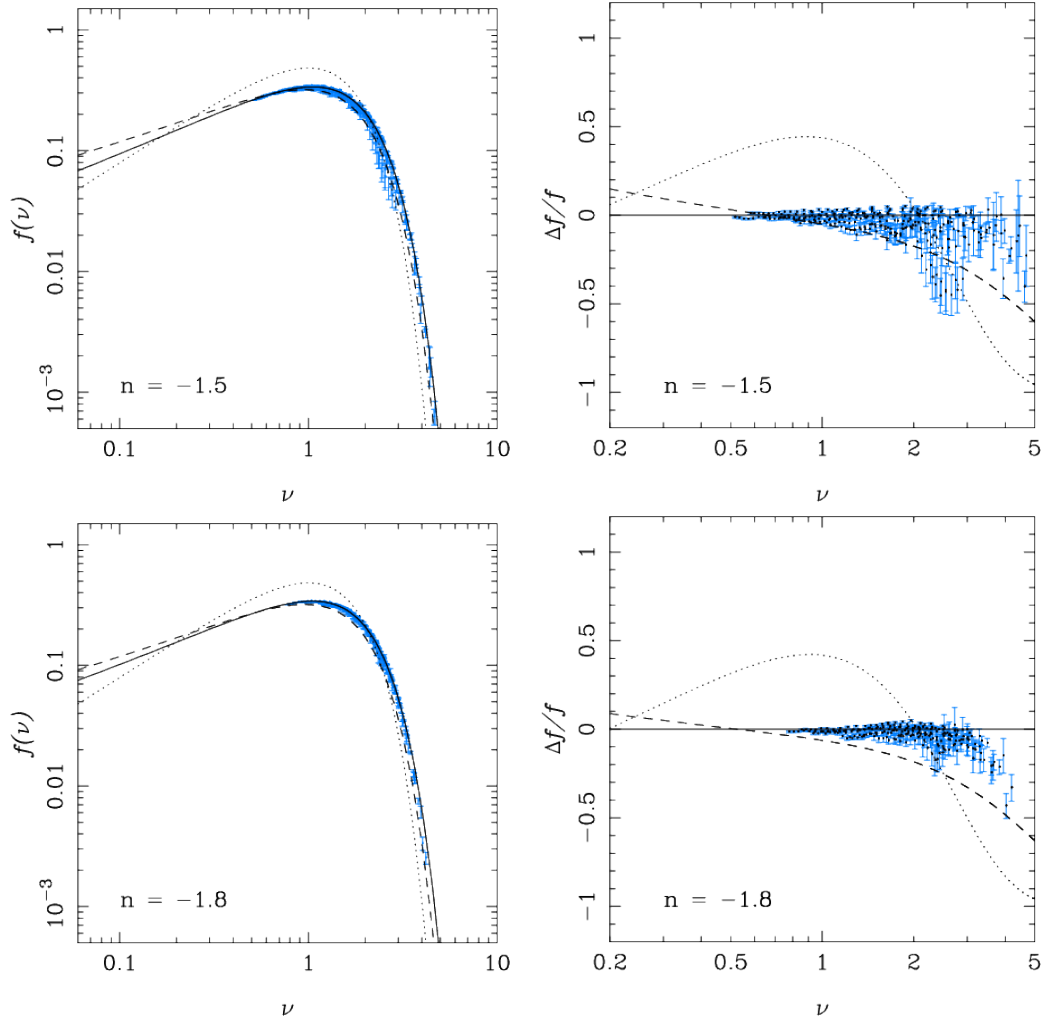


Figure 4.5: Same as Figure (4.3), except that the solid black line here indicates Sheth-Tormen mass function with parameters obtained by extrapolating $p(n)$ and $q(n)$ from $-1 \leq n \leq 0$ as shown in Figure (4.4).

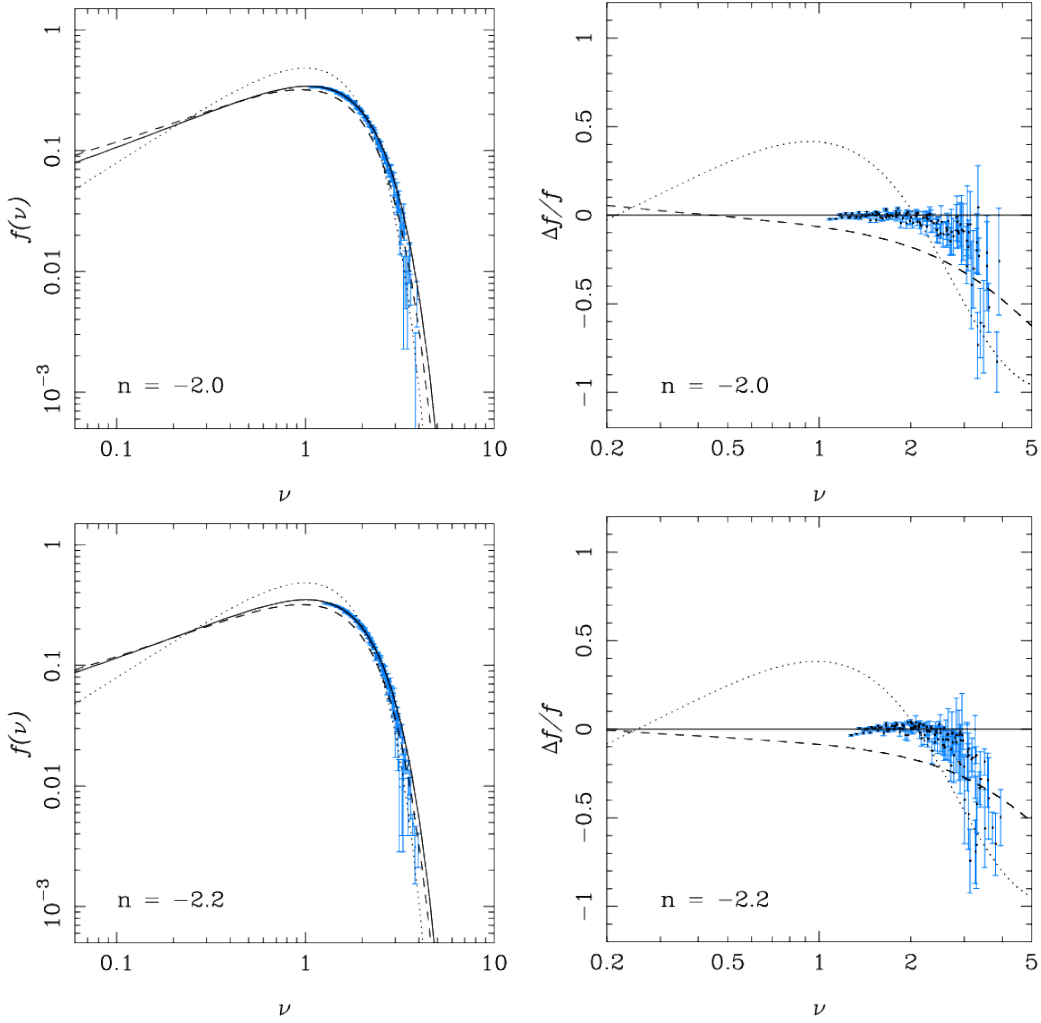


Figure 4.6: Same as Figure (4.3), except that the solid black line here indicates Sheth-Tormen mass function with parameters obtained by extrapolating $p(n)$ and $q(n)$ from $-1 \leq n \leq 0$ as shown in Figure (4.4).

stand how further complications in the model, like running index and different cosmologies, affect the shape of the mass function.

Our focus has been on demonstrating that the mass function has a dependence on the slope of the power spectrum. In this study we have not looked at how a change in the definition of the halo—for example, change in the linking length in FOF halo finder or using the SO halo finder instead of FOF (Lacey & Cole, 1994; Tinker et al., 2008)—affects the mass function. Indeed one expects that the halo definition changes the amplitude of the mass function (Cohn & White, 2008; White, 2002; Tinker et al., 2008) but we do not expect it to affect our results in a significant manner.

4.6 Conclusions

We summarize the conclusions of the present study here.

- We find that the mass function is not universal and has an explicit dependence on the power spectrum.
- The Sheth-Tormen parameters show a systematic trend with index of the power law power spectrum. We also find that there is a correlation between these parameters.
- Evolution of the mass function $f(\nu)$ in power law models in an Einstein de Sitter background is self-similar, i.e., the functional form does not change with time for a given power law model. We do not expect this in the CDM class of spectra since the effective index, n_{eff} , changes with redshift. However, the spectrum dependence of p and q is not very strong, and the range over which n_{eff} varies is not very large, hence the usual ST parameters are an adequate first approximation. Variation of ST parameters becomes relevant if we require a very precise description of the mass function.
- Our χ^2 analysis shows that Sheth-Tormen mass function is inadequate and that better modeling of collapse with more parameters is needed.

- Finite box size considerations impose serious limitations on running simulations with large negative indices of the power spectrum. This end of the spectrum probes the mass function of high redshift objects. The way out would be to run orders of magnitude larger simulations for indices with $n \rightarrow -3$. This is a challenge and would be overcome only in the next generation of simulations.
- For models with $n \gg -3$, the rate of growth for r_{nl} with time is very slow and as a result a large number of time steps are required for evolving the system. The Adaptive TreePM (Bagla & Khandai, 2009) may be useful for running such simulations.

Chapter 5

HI as a Probe of the Large Scale Structure in the Post-Reionization Universe: Power Spectrum and its Evolution.

Until now we have only studied the clustering of dark matter using N -body simulations simulations. Unfortunately direct detection of dark matter is not possible since it is very weakly interacting. However most observations probe the Universe through visible matter or baryons by targeting specific windows of the electromagnetic spectrum. In the next two chapters we focus on one such window, the redshifted 21cm line of neutral Hydrogen (HI hereafter). We model the distribution of HI in the post-reionization universe. This model uses gravity only N-Body simulations and an ansatz to assign HI to dark matter haloes that is consistent with observational constraints and theoretical models. We then compute the smoothed one point probability distribution function and the power spectrum of fluctuations in HI. This is compared with other predictions that have been made using different techniques. We highlight the significantly high bias for the HI distribution at small scales. This aspect has not been discussed before and it implies that a statistical detection of HI at large scales and direct detection of the brightest regions at moderate

redshifts requires comparable integration time using existing telescopes.

5.1 Introduction

Dark matter responds mainly to gravitational forces, and by virtue of larger density than baryonic matter, assembly of matter into haloes and large scale structure is driven by gravitational instability of initial perturbations. Galaxies are believed to form when gas in highly over-dense haloes cools and collapses to form stars in significant numbers (Hoyle, 1953; Rees & Ostriker, 1977; Silk, 1977; Binney, 1977). The formation of first stars (McKee & Ostriker, 2007; Zinnecker & Yorke, 2007; Bromm & Larson, 2004) in turn leads to emission of UV radiation that starts to ionize the inter-galactic medium (IGM). The period of transition of the IGM from a completely neutral to a completely ionized state is known as the epoch of reionization (EoR), e.g., see Loeb & Barkana (2001). Observations indicate that the process of reionization was completed before $z \sim 6$ (Fan, Carilli, & Keating, 2006; Becker et al., 2001; Fan et al., 2006). Many possible sources of ionizing radiation have been considered, although stellar sources are believed to be the most plausible candidates, see, e.g., Bagla, Kulkarni, & Padmanabhan (2009).

Prior to the EoR, almost all the Hydrogen in the universe is in atomic form. Through the EoR Hydrogen is ionized till we are left with almost no HI in the inter-galactic medium and almost all the HI resides in the inter stellar medium (ISM) of galaxies. We focus on the post-reionization era in this work and our aim is to make predictions about the distribution of HI in this regime. It had been proposed by Sunyaev & Zeldovich (1972, 1975) that the hyperfine transition of Hydrogen may be used to probe primordial galaxies. This problem has been approached in past from the perspective of making specific predictions for instruments like the GMRT (Subramanian & Padmanabhan, 1993; Kumar, Padmanabhan, & Subramanian, 1995; Bagla, Nath, & Padmanabhan, 1997; Bagla, 1999; Bharadwaj, Nath, & Sethi, 2001; Bharadwaj & Sethi, 2001; Bagla & White, 2003; Bharadwaj & Srikant, 2004; Bharadwaj & Ali, 2005), or upcoming instruments like the the MWA¹, ASKAP² and SKA³,

¹The Murchison Widefield Array (MWA). See <http://www.mwatelescope.org/> for details.

²The Australian SKA Pathfinder. <http://www.atnf.csiro.au/projects/askap/> for details.

³The Square Kilometer Array (SKA). See <http://www.skatelescope.org/> for details.

e.g., see Wyithe, Loeb, & Geil (2008). Much work in the last decade has focused on making predictions for the power spectrum of fluctuations in HI, with an implicit assumption that it is easier to make a statistical detection than a direct detection. Most of the instruments are sensitive to the power spectrum of fluctuations at large scales, certainly larger than the scale of non-linearity at the relevant epoch, and hence a significant fraction of the work done in terms of making predictions is based on linear theory or approximations that work well in the linear and quasi-linear regime. The halo model has also been used for predicting the spectrum of fluctuations in the post-reionization universe.

In this study we revisit the issue of predicting fluctuations and use high resolution N-Body simulations. This allows us to study fluctuations at scales comparable to, or even smaller than the scale of non-linearity. We use dark matter simulations along with simple ansatz for assigning neutral Hydrogen in order to make predictions of fluctuations in surface brightness temperature. Our model is discussed in detail in §2. In §2.1 we summarize our knowledge of the HI distribution at high redshifts and motivate the assignment schemes we use in this work in §2.2. The N-Body simulations used by us are described in §2.3. Results and discussion follow in §3 and we conclude in §4.

5.2 Modeling the HI distribution

In this section we describe our model of the HI distribution at high redshifts.

Our knowledge of the HI distribution in the universe is derived mainly from QSO absorption spectra, where the gas absorbs in the Lyman- α transition of the Hydrogen atom. We know from observations of these absorption spectra that much of the inter-galactic medium (IGM) is highly ionized and does not contain a significant amount of neutral Hydrogen. Most of the neutral Hydrogen resides in relatively rare damped Lyman- α systems (DLAS) (Wolfe, Gawiser, & Prochaska, 2005). DLAS and other high column density absorption features are believed to arise due to gas within galaxies (Haehnelt, Steinmetz, & Rauch, 2000; Gardner et al., 2001). It is possible to make a quantitative estimate of the total neutral Hydrogen content in DLAS and study the evolution of the total neutral Hydrogen content of the universe (Storrie-Lombardi, McMahon, & Irwin, 1996; Rao &

Turnshek, 2000; Péroux et al., 2005). These observations indicate that at $1 \leq z \leq 5$, the neutral Hydrogen content of the universe is almost constant with a density parameter of $\Omega_{HI} \simeq 0.001$.

At low redshifts, the HI content can be estimated more directly through emission in the Hyperfine transition. Observations in the local universe indicate a much lower neutral Hydrogen content than seen at $z \geq 1$ (Zwaan et al., 2005). The neutral gas fraction in galaxies at intermediate redshifts appears to be much higher than in galaxies in the local universe (Lah et al., 2007, 2009).

The spin temperature couples to the gas temperature through collisions of atoms with other atoms, electrons, ions and also the Wouthuysen-Field effect (Purcell & Field, 1956; Field, 1958, 1959; Wouthuysen, 1952a,b; Furlanetto, Oh, & Briggs, 2006). Observations of 21 cm absorption by DLAS indicate that the spin temperature is orders of magnitude higher than the temperature of the cosmic microwave background radiation (CMBR) at the corresponding redshifts (Chengalur & Kanekar, 2000; Kanekar et al., 2009). This implies that the emission in the 21 cm hyperfine transition can be safely assumed to be proportional to the density of neutral Hydrogen, see, e.g., Furlanetto, Oh, & Briggs (2006).

$$\begin{aligned} \delta T_b(z) &= 4.6 \text{ mK} \left(1 - \frac{T_{cmb}}{T_s}\right) (1+z)^2 \frac{H_0}{H(z)} \\ &\quad \times x_{HI} (1+\delta) \left[\frac{H(z)}{(1+z)(dv_{\parallel}/dr_{\parallel})} \right] \\ &\simeq 7.26 \text{ mK} (1+z)^2 \frac{H_0}{H(z)} \frac{M_{HI}}{10^{10} M_{\odot}} \left(\frac{L}{1 \text{ Mpc}} \right)^{-3} \\ &\quad \times \left[\frac{H(z)}{(1+z)(dv_{\parallel}/dr_{\parallel})} \right] \end{aligned} \quad (5.1)$$

where x_{HI} is the fraction of Hydrogen in neutral form, δ is the density contrast of the gas distribution, T_{cmb} is the temperature of the CMBR T_s is the spin temperature defined using the relative occupation of the two levels for the hyperfine transition:

$$\frac{n_1}{n_0} = \frac{g_1}{g_0} \exp \left\{ -\frac{T_{\star}}{T_s} \right\}, \quad (5.2)$$

where subscripts 1 and 0 correspond to the excited and ground state levels of the hyperfine

transition, $T_\star = h\nu/k_B = 68$ mK is the temperature corresponding to the transition energy, and $g_1/g_0 = 3$ is the ratio of the spin degeneracy factors of the levels.

Observations indicate that neutral gas is found only in galaxies in the post reionization universe. Further, we know that galaxies in groups and clusters do not contain much neutral gas. As cold gas is associated with galaxies, we may assume that it exists only in haloes that are more massive than the Jeans mass. Further, we assume that neutral gas is predominantly found in galaxies and not in larger haloes that may contain several large galaxies. Jeans mass for haloes in a photo-ionizing UV background depends on the shape of the spectrum of the ionizing radiation, typically we expect gas in haloes with a circular velocity in excess of 60 km/s to cool, fragment and form stars. The mass within the virial radius is related to the circular velocity and the collapse redshift as:

$$M_{vir} \simeq 10^{10} M_\odot \left(\frac{v_{circ}}{60 \text{ km/s}} \right)^3 \left(\frac{1+z_c}{4} \right)^{-3/2} \quad (5.3)$$

Simulation studies show that DLAS can reside in haloes with even lower circular velocities (Pontzen et al., 2008), i.e., haloes with mass lower than the expected Jeans mass can contain significant amount of neutral Hydrogen. The gas in these haloes is able to self shield and maintain a significant amount of HI even though the amount of gas is insufficient for sustaining star formation⁴. We use this input and impose a lower cutoff in circular velocity of 30 km/s, i.e., haloes with a lower circular velocity are not assigned any HI. Pontzen et al. (2008) also found that haloes much more massive than a few times $10^{11} M_\odot$ do not host significant amount of HI. This is consistent with observations in the local universe where galaxies in groups and clusters of galaxies contain very little HI. Some observations suggest that the neutral fraction in galaxies in outer parts of clusters of galaxies may be high compared to corresponding galaxies in the local universe (Lah et al., 2009). Assignment for HI in more massive haloes is done in such a way as to ensure that very massive haloes have a zero or negligible fraction of the total gas in neutral form. The transition scale for the higher masses is chosen to coincide with 200 km/s. Given that it is easier to estimate

⁴Haloes that collapse much earlier may have hosted star formation, indeed the ISM of such galaxies may have been blown away due to feedback. However, few haloes with a low circular velocity that collapse very early are likely to survive without merger well into the post-reionization era. Errors arising out of HI assignment to low circular velocity haloes should not lead to significant changes in our calculations.

Table 5.1: The table lists the minimum mass of haloes M_{min} that hosts HI in the simulated HI distribution. The first column lists the redshift where simulated maps are constructed, the second column lists M_{min} we get by assuming a lower bound of 30 km/s on the circular velocity of haloes, and column 4 lists the actual minimum halo mass used in construction of the simulated maps. All masses are given in units of solar mass M_\odot . Column 3 lists the characteristic maximum mass of haloes computed using an upper bound on circular velocity of 200 km/s and Column 5 shows the actual upper bound used while making simulated maps. Column 6 lists the HI fraction of the total baryonic mass if we use the first HI assignment scheme (see Eqn.(5.4)).

z	M_{min}	M_{max}	M_{min}^{sim}	M_{max}^{sim}	$F_1 \Omega_{nr}/\Omega_b$
5.1	$10^{8.83}$	$10^{11.30}$	$10^{8.81}$	$10^{11.30}$	0.24
3.4	$10^{9.04}$	$10^{11.52}$	$10^{9.02}$	$10^{11.50}$	0.15
1.3	$10^{9.43}$	$10^{11.92}$	$10^{9.43}$	$10^{11.90}$	0.11

mass than circular velocity for haloes identified in simulations, in particular for haloes with a small number of particles, we choose to translate the threshold in circular velocity to a threshold in mass assuming the collapse redshift and the redshift at which the system is being observed to be the same, i.e., $z_c = z$. While this may lead to inaccuracies regarding inclusion of haloes close to the low mass end, we do not expect it to influence the results. The minimum and the maximum masses for the redshifts considered here are listed in Table 5.1.

Given a halo of mass M , all particles in it are assigned an equal HI mass which is a fraction of their total mass. We describe three kinds of mass assignments here.

$$F_1(M) = f_1 \quad (M_{min} \leq M \leq M_{max}) \quad (5.4)$$

$$F_2(M) = \frac{f_2}{1 + \left(\frac{M}{M_{max}}\right)^2} \quad (M_{min} \leq M \leq M_{max}) \quad (5.5)$$

$$F_3(M) = \frac{f_3}{1 + \left(\frac{M}{M_{max}}\right)} \quad (M_{min} \leq M \leq M_{max}) \quad (5.6)$$

Here $F_k(M)$ is the mass fraction of HI in a given halo. The fraction of baryons that is in the form of neutral Hydrogen is given by $F_k(M)\Omega_{nr}/\Omega_b$, where Ω_b is the density parameter of Baryons and Ω_{nr} is the density parameter for non-relativistic matter. For the best fit model for WMAP-5 (Komatsu et al., 2009) the ratio has the value $\Omega_b/\Omega_{nr} \simeq 0.17 \simeq 1/6$.

In all three cases the constant f_k is determined by normalizing the HI mass in the simulation volume to $\Omega_{HI} = 0.001$, the density parameter of HI indicated by observations at relevant redshifts (Péroux et al., 2005). It is noteworthy that this normalization requires a significant fraction of gas in haloes in the mass range between M_{min} and M_{max} be neutral at high redshifts. In the assignment scheme with the sharp cutoff (scheme 1, Eqn. 5.4), the HI fraction is the same in all haloes with mass between M_{min} and M_{max} . In the second assignment scheme the HI fraction in a halo decreases monotonically with increasing halo mass, and for large halo masses the HI mass goes to zero. This scheme applies to the physical situation where very large haloes do not have any neutral Hydrogen. In scheme 3, the HI fraction decreases monotonically with increasing halo mass but the HI mass goes to a constant value. The motivation of this scheme is to allow for some neutral Hydrogen surviving in massive haloes in galaxies that are in the process of falling in. In the following section, we compare the resulting distribution of HI with the three assignment schemes described above. The present work is the first one where mass resolution of simulations is adequate for resolving the smallest haloes that may host HI and the simulation volume is also sufficient to make statements about the large scale distribution. We also ensure that the finite size of the simulation volume does not affect the results presented here.

5.2.1 *N*-Body Simulations

We use gravity only simulations run with the TreePM code (Bagla, 2002; Bagla & Ray, 2003; Khandai & Bagla, 2009). The suite of simulations used here is described in the Table 5.2. The cosmological model and the power spectrum of fluctuations corresponds to the best fit model for WMAP-5: $\Omega_{nr} = 0.26$, $\Omega_\Lambda = 0.74$, $n_s = 0.96$, $\sigma_8 = 0.79$, $h = 0.72$, $\Omega_b h^2 = 0.02273$ (Komatsu et al., 2009).

We use the Friends-of-Friends (FOF) (Davis et al., 1985) algorithm with a linking length $l = 0.2$ to identify haloes and construct a halo catalog. The HI assignment schemes

Table 5.2: Columns 1 and 2 list the size of the box and the number of particles used in the simulations. Columns 3 and 4 give the mass and force resolution of the simulations, while columns 5 and 6 tell us the redshift at which the simulations were terminated and the redshifts for which the analysis were done

L_{box} ($h^{-1}Mpc$)	N_{part}	m_{part} ($h^{-1}M_\odot$)	ϵ ($h^{-1}kpc$)	z_f	z_{out}
23.04	512^3	6.7×10^6	1.35	5.0	5.04
51.20	512^3	7×10^7	3.00	3.0	3.34
76.80	512^3	2.3×10^8	4.50	1.0	1.33

are then used to obtain the distribution of neutral Hydrogen.

Several existing and upcoming instruments can probe the post-reionization universe using redshifted HI emission. The Giant Meterwave Radio Telescope⁵ (GMRT) can observe redshifted HI emission from a few selected redshift windows whereas most other instruments have continuous coverage in redshift bounded on two sides. We choose to focus on the GMRT windows, as these are representative of the range of redshifts in the post-reionization universe. In particular we will focus on the following redshift windows of GMRT: $z_{out} = 5.04, 3.34, 1.33$. Finite box effects can lead to significant errors in the distribution of haloes that host galaxies, apart from errors in the abundance of haloes of different masses (Bagla & Prasad, 2006; Bagla, Prasad, & Khandai, 2009). The choice of simulations used in this work ensures that such effects do not contribute significantly. Previous studies have indicated that at $z \simeq 0$, we need a simulation box with $L_{box} \geq 140h^{-1}Mpc$ for the finite size effects to be negligible (Bagla & Ray, 2005; Bagla & Prasad, 2006). On the other hand the mass resolution of particles decreases as the cube of simulation volume. We balance the requirements of high mass resolution and a sufficiently large box size by using different simulations for studying the HI distribution at different redshifts. Details of the simulations are given in the table. 5.2.

⁵See <http://gmrt.ncra.tifr.res.in/> for further details.

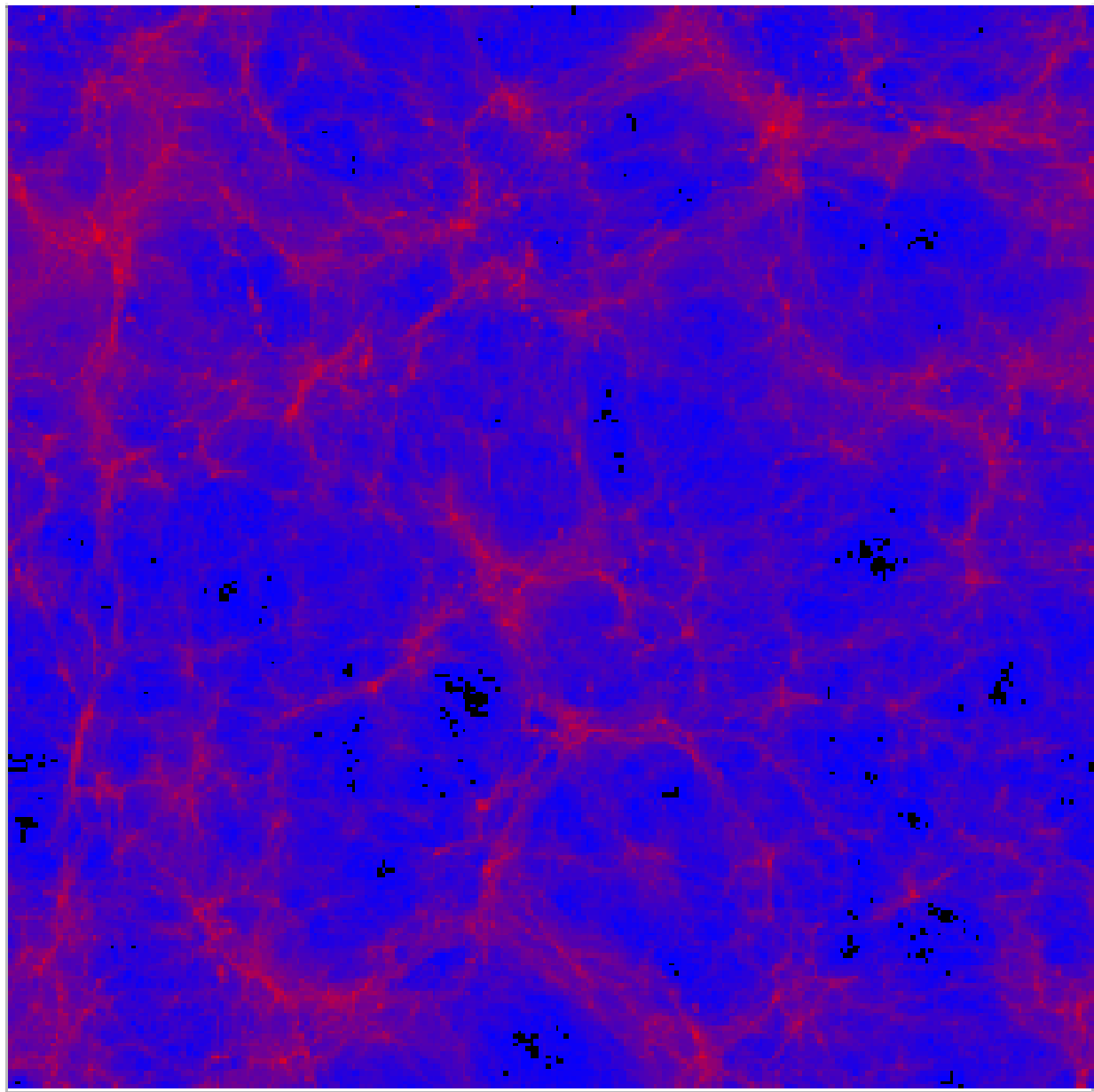


Figure 5.1: Slice of a simulation illustrating $(1+\delta_{DM})$ at $z = 3.34$ in a simulation box of side $L_{box} = 51.2h^{-1}\text{Mpc}$. The thickness of the slice corresponds to a bandwidth of 0.25MHz. This is color coded such that red represents the dense regions, blue represents the regions with average density and black indicates that there is no dark matter.

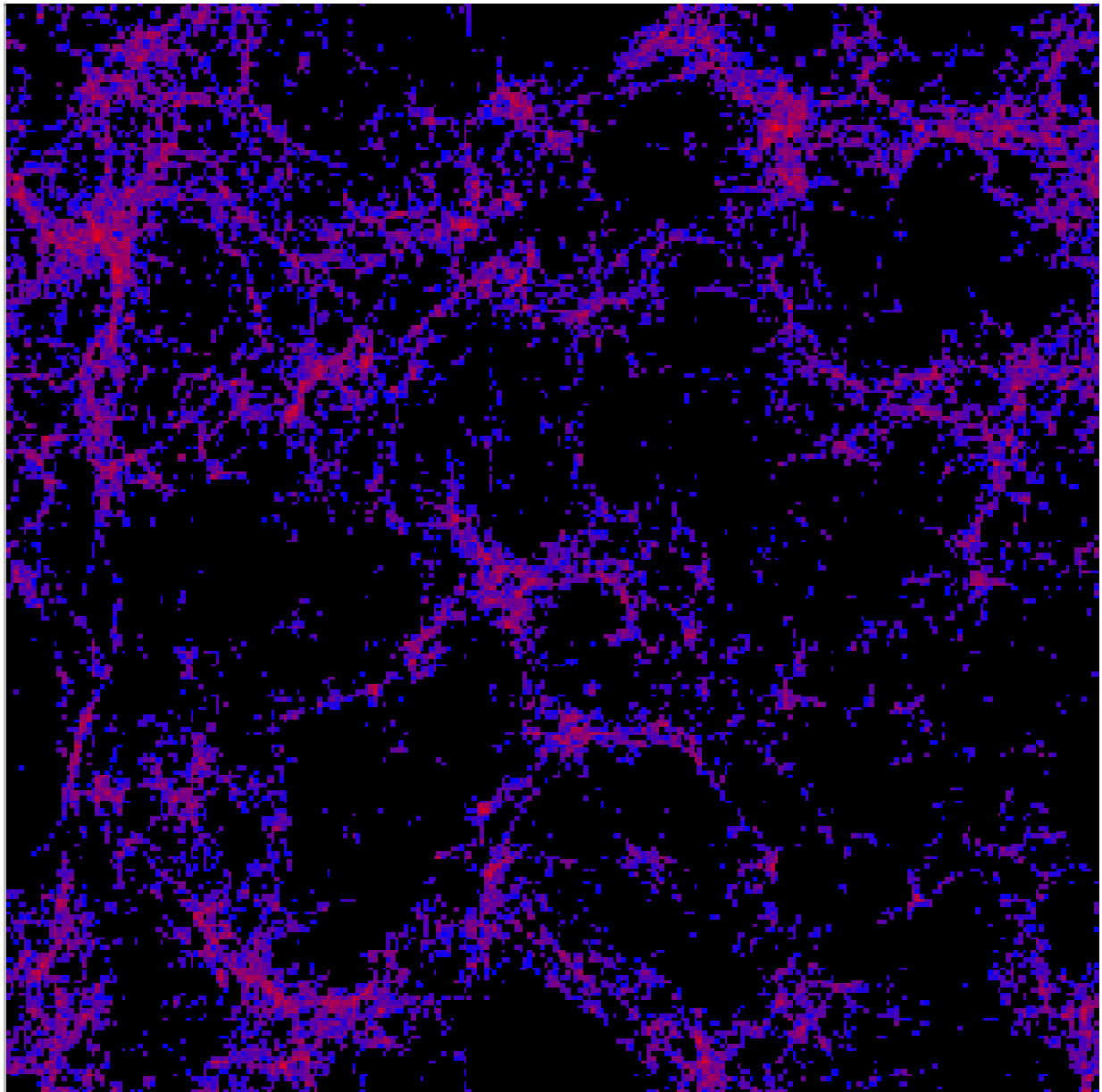


Figure 5.2: Slice of a simulation illustrating $(1 + \delta_{HALO})$ at $z = 3.34$ in a simulation box of side $L_{box} = 51.2h^{-1}\text{Mpc}$. The thickness of the slice corresponds to a bandwidth of 0.25MHz. The color coding is similar to figure 5.1

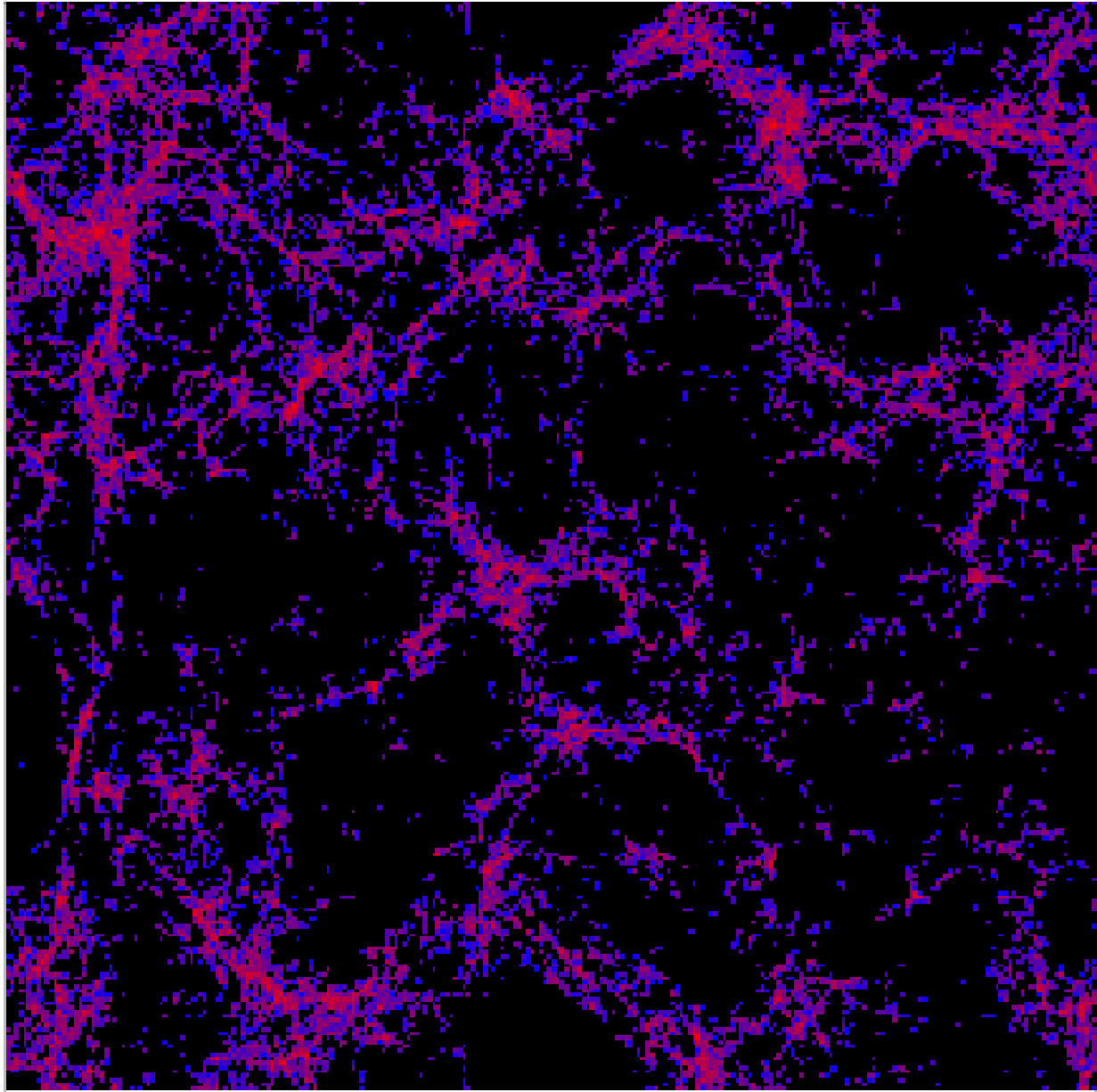


Figure 5.3: Slice of a simulation illustrating $(1 + \delta_{HI})$ at $z = 3.34$ in a simulation box of side $L_{box} = 51.2h^{-1}\text{Mpc}$. The thickness of the slice corresponds to a bandwidth of 0.25MHz. The color coding is similar to figure 5.1

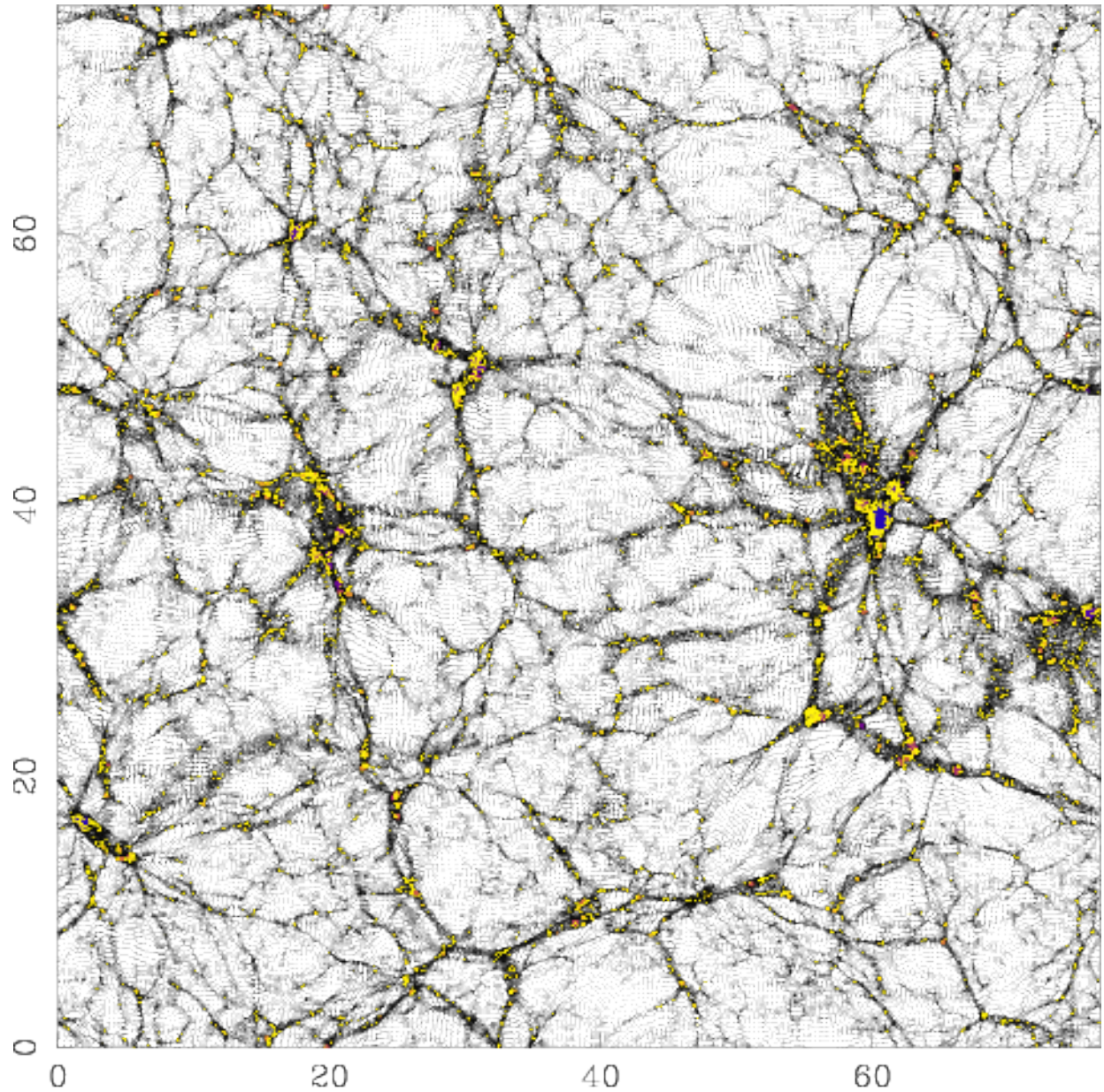


Figure 5.4: Slice of a simulation illustrating F_3 , eq. 5.6, at redshift $z = 1.33$ in a simulation box of side $L_{box} = 76.8h^{-1}\text{Mpc}$. The thickness of the slice corresponds to $0.45h^{-1}\text{Mpc}$. The color coding is such that yellow represents particles with the maximum F_3 and blue represents those with the least F_3 . Black indicates particles which haven't been assigned any H I.

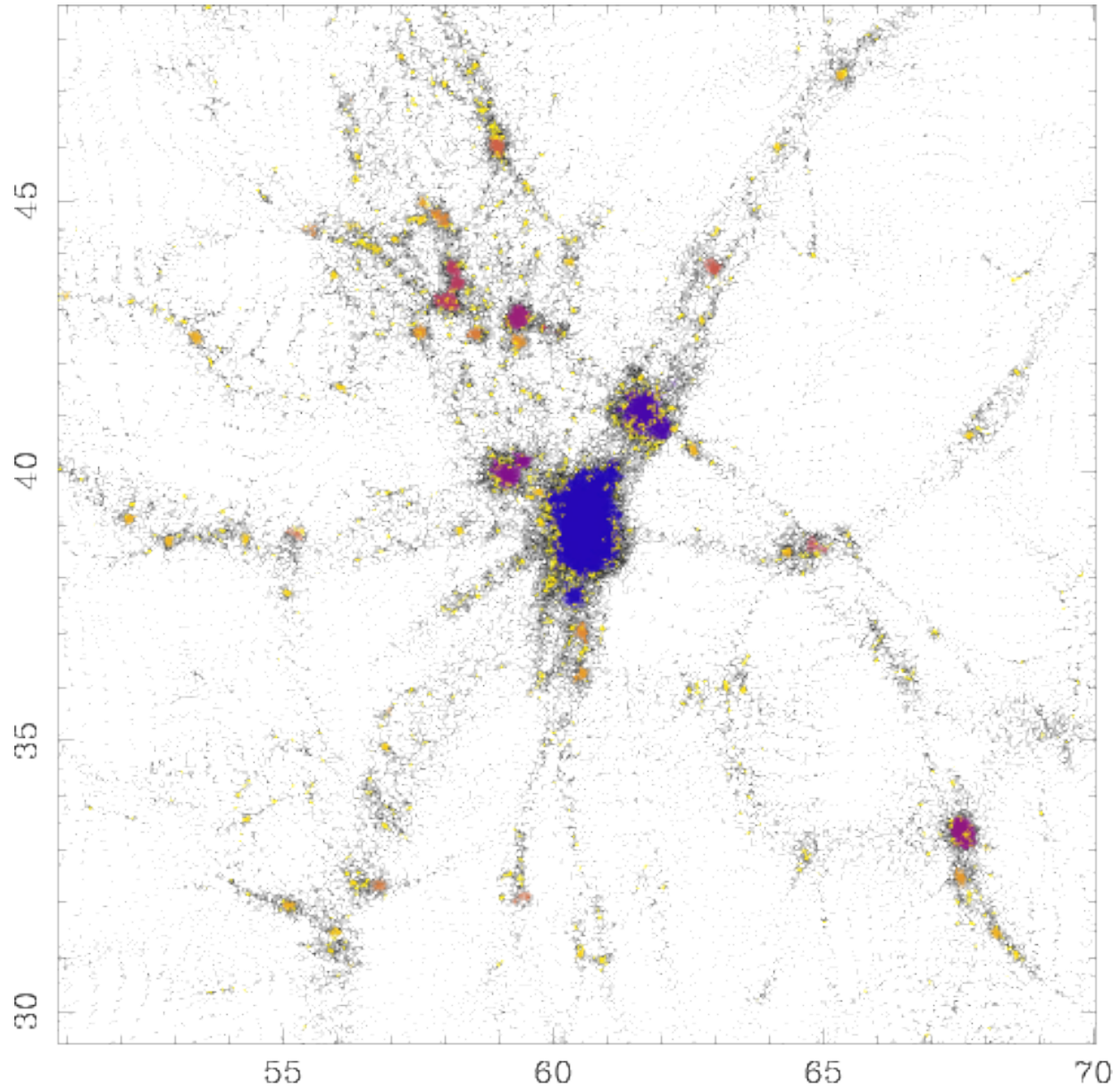


Figure 5.5: Zoom in of figure 5.4 around coordinates $(x, y) = (60, 40)$

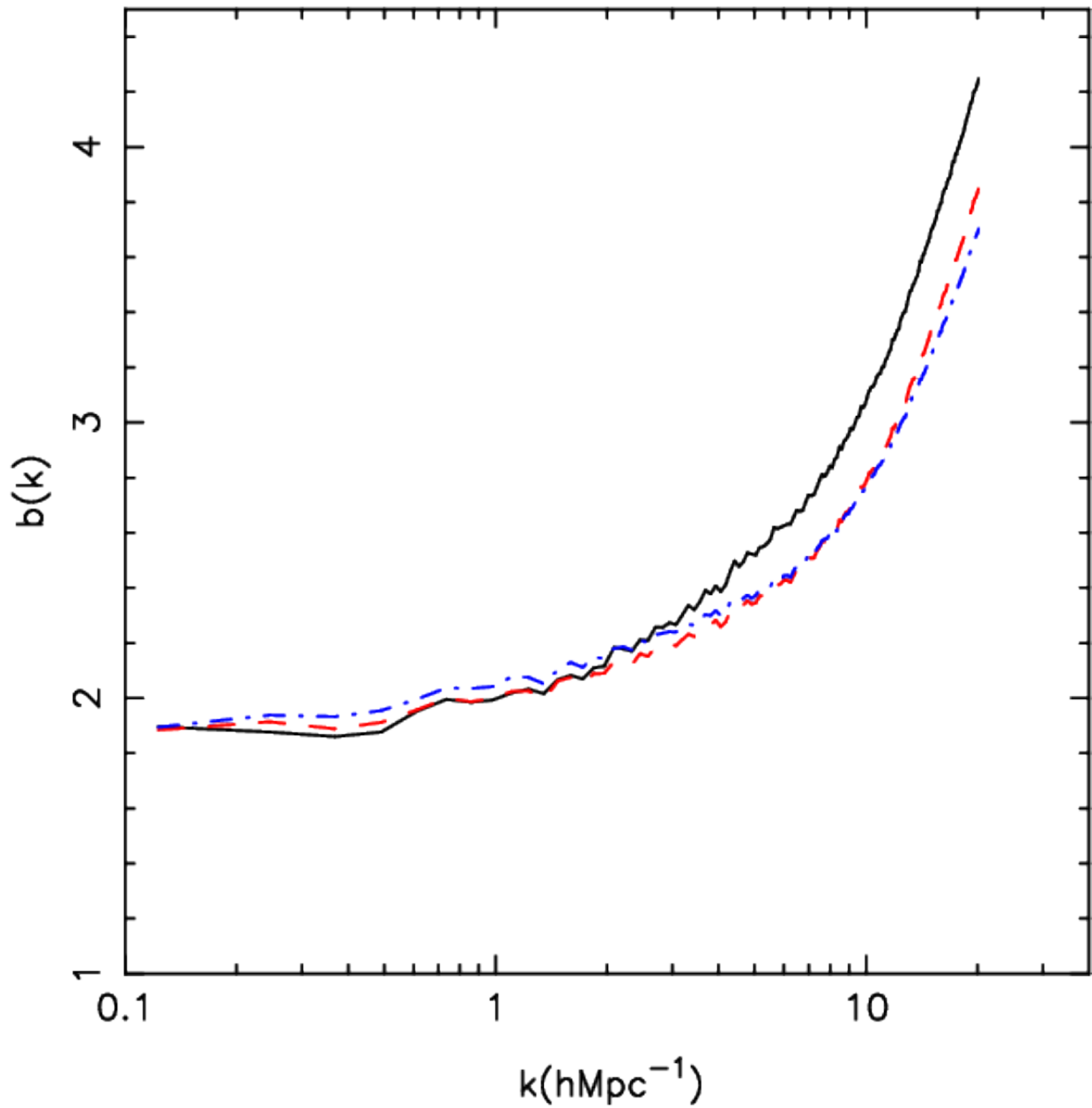


Figure 5.6: Effect of HI mass assignment type on bias. Solid, dashed and dot-dashed lines are for HI assignment types 1, 2 and 3 as described in eqs. 5.4-5.6. Bias was computed at $z = 3.34$ for the $51.2\text{h}^{-1}\text{Mpc}$ box with $M_{max} = 10^{11.5} M_\odot$.

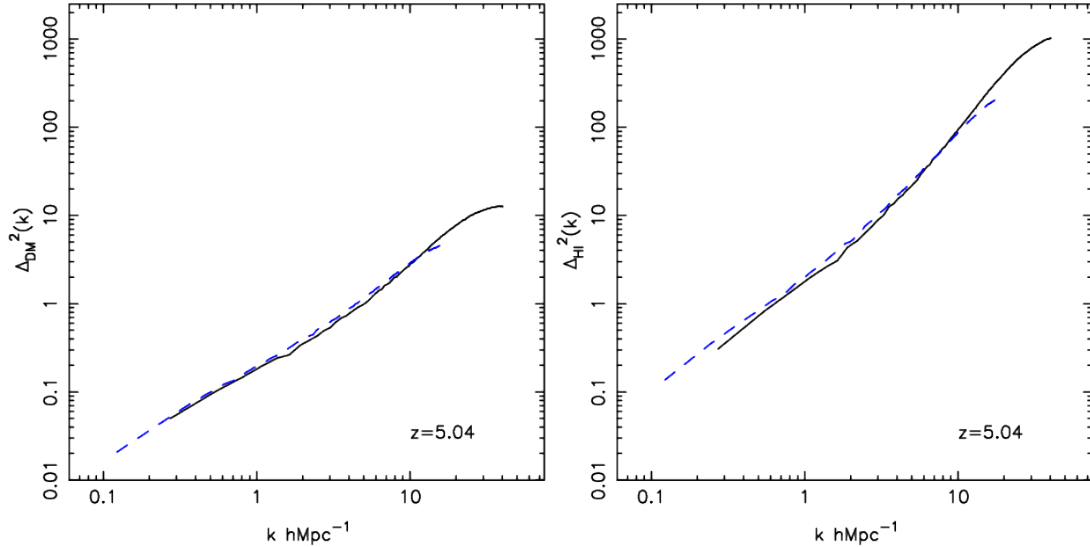


Figure 5.7: *Left:* The dark matter power spectrum in the simulations with $L_{box} = 23 \text{ h}^{-1}\text{Mpc}$ and $L_{box} = 51.2 \text{ h}^{-1}\text{Mpc}$ at $z = 5.1$. *Right:* HI power spectrum in the same simulations, see text for details.

5.3 Results

Given an HI mass assignment for particles in a simulation, we can proceed to compute the expected signal from the HI distribution by making mock radio maps and spectra.

However before proceeding to the main results we visually illustrate how HI is assigned in a dark matter simulation. Figure 5.1 shows a slice of thickness 0.25MHz from the $51.2\text{h}^{-1}\text{Mpc}$ simulation at redshift $z = 3.34$. The color codes values of $1 + \delta_{DM}$ with black representing the underdense regions, while blue represents the average and the red pixels are the densest regions. Owing to the large thickness of the slice, most of the fluctuations in density have been smoothed out. Figure 5.2 shows dark matter particles in haloes, color coded for $1 + \delta_{HALO}$. These particles are assigned HI with the assignment scheme 3 (eq.5.6) and figure 5.3 illustrates this, the color coding being for $1 + \delta_{HI}$. In the following discussion we will argue why we prefer this scheme. A careful inspection reveals that whereas δ_{HALO} decreases in the filaments δ_{HI} doesn't. One finds that the largest halos also contain a large

HI mass, because even though they have the lowest HI mass per dark matter particle, the assignment scheme guarantees that the mass contained in the largest halos saturates to a constant value. This point is illustrated in figures 5.4 and 5.5. Figure 5.5 is a zoom in of the region around the largest halo located near the coordinates $(x, y) = (60, 40)$. Here we take an even lower redshift in the $76.8h^{-1}\text{Mpc}$ box so as to have larger halos. The slice is extremely thin so as to cut across the largest halos. The color coding is for F_3 , eq. (5.6). With black marking the $F_3 = 0$ and yellow marking the particles with the maximum F_3 . Here we find that the bigger halos have less HI assigned per particle, whereas the smallest halos have the most HI. It is interesting to note that the satellite halos around the larger halos have a considerably larger HI as compared to the parent halo.

We also compute the power spectrum in both real and redshift space. For redshift space calculations, we use the peculiar velocity information of particles in haloes. Unlike earlier studies, we resolve haloes of individual galaxies and hence the internal velocity dispersion is naturally accounted for and there is no need to add it by hand (Kumar, Padmanabhan, & Subramanian, 1995; Bagla, Nath, & Padmanabhan, 1997; Bagla & White, 2003).

We use the clouds-in-cell (CIC) smoothing to interpolate densities from particle locations to grid points for the purpose of computing densities and the power spectrum. It is convenient to express the HI power spectrum in terms of the brightness temperature, though in comparisons with the dark matter power spectrum we revert to the usual dimensionless form.

We define the real and redshift space scale dependant bias by the ratio of the corresponding dark matter and HI power spectra.

$$b(k) = \left[\frac{P_{\text{HI}}(k)}{P_{\text{DM}}(k)} \right]^{1/2} \quad (5.7)$$

$$b^s(k) = \left[\frac{P_{\text{HI}}^s(k)}{P_{\text{DM}}^s(k)} \right]^{1/2} \quad (5.8)$$

We start by checking the effect of HI assignment scheme on the resulting distribution. We have computed the bias $b(k)$ at $z = 3.34$ for the $L_{\text{box}} = 51.2h^{-1}\text{Mpc}$ simulation using the three schemes introduced above. The results are illustrated in the left panel of Figure 5.6 for

the three assignment types Eqs. (5.4-5.6). We see that at large scales the three assignment schemes give very similar results, whereas there is some disagreement between the assignment scheme Eqn.(5.4) and the other two. The difference can be attributed to the fact that the scheme described in Eqn.(5.4) puts more HI mass in haloes with masses near M_{max} . The figure also highlights that the differences between the HI assignment schemes are relatively minor. We choose to work with scheme described in Eqn.(5.6) due to the better physical justification, as discussed in §5.2.

It is noteworthy that while the bias is strongly scale dependent at large k (small scales), it flattens out to a constant value at small k (large scales).

In order to check for the effects of a finite box size, we carried out a test for the $23 \text{ h}^{-1}\text{Mpc}$ simulation box. Instead of using the range of halo masses for HI assignment that is appropriate for $z = 5.1$, we work with a slightly smaller range so that haloes of these masses can be found in the $51.2 \text{ h}^{-1}\text{Mpc}$ simulation as well. Figure 5.7 shows the dark matter power spectrum (Left panel) and the HI power spectrum (Right panel) with the HI assignment restricted to a smaller range of masses, as described above. We see that the dark matter power spectra from the two simulations agree through the range of scales where there is an overlap. The HI power spectra also agree, though not as well as the dark matter power spectra. These differences are so small that we do not expect these to affect the final results in a significant manner. The difference can be attributed to the fact that clustering of haloes is effected more strongly by the box size effects in simulations (Gelb & Bertschinger, 1994; Bagla & Ray, 2005).

These tests validate our approach for assignment of HI to haloes, and also show that the effects of a finite box-size are not significant at the level of the power spectrum or the mass function.

5.3.1 Bias

This is amongst the first studies of the HI distribution at high redshifts where we resolve the smallest haloes that can host significant amount of HI while ensuring that the finite box size effects do not lead to an erroneous distribution of haloes. One of the points that we can address here is the effect of non-linear clustering on the HI distribution and the

scale dependance of bias. Some of these effects are illustrated in Figure 5.8 where we have plotted the power spectrum of fluctuations: the solid line shows the linearly extrapolated power spectrum, the dashed line shows the non-linear dark matter power spectrum and the dot-dashed line shows the HI power spectrum. All power spectra are for $z = 3.34$. The dark matter and the HI power spectra have been computed with the simulation with $L_{box} = 51.2 \text{ h}^{-1}\text{Mpc}$.

It is apparent that at $k > 0.5 \text{ h Mpc}^{-1}$ the effects of non-linear clustering significantly enhance the dark matter power spectrum. At $k \sim 10 \text{ h Mpc}^{-1}$, the enhancement is close to an order of magnitude. This is of utmost interest for upcoming instruments that can resolve small angular scales.

We find that bias $b(k)$ for the HI distribution is much greater than unity at high redshifts. This is to be expected of galaxies at high redshifts (Fry, 1996; Mo & White, 1996; Bagla, 1998a,b; Mo, Mao, & White, 1999; Baugh et al., 1999; Magliocchetti et al., 2000; Benson et al., 2000; Roukema & Valls-Gabaud, 2000; Sheth, Mo, & Tormen, 2001). We note that the bias is scale dependent, and leads to a larger enhancement in the power spectrum at very small scales.

The value of bias depends strongly on the choice of the characteristic mass of haloes with HI. This is shown in Figure 5.9. All curves are for $z = 3.34$ and have been computed with the simulation with $L_{box} = 51.2 \text{ h}^{-1}\text{Mpc}$. This figure illustrates that the bias at all scales varies monotonically with the charactersitic mass of haloes with HI. Variation is gentle at large scales but fairly strong at small scales. Therefore it is extremely important to have an accurate estimate of the charactersitic masses of such haloes. Indeed, it has been pointed out that observations of the amplitude of clustering in the HI distribution can be used to constrain masses of haloes that host DLAs (Wyithe, 2008).

While the preceeding figures describe the statistical bias computed from the ratio of power spectra, Figure 5.10 shows the stochasticity of bias (Dekel & Lahav, 1999) in the HI distribution. This figure shows a scatter plot of δ_{HI} smoothed at a scale of $3 \text{ h}^{-1}\text{Mpc}$ with a spherical top hat window, plotted as a function of δ_{DM} smoothed at the same scale. The figure shows a random subset of points from the simulation with $L_{box} = 51.2 \text{ h}^{-1}\text{Mpc}$ at $z = 3.34$. The scatter about the average trend in the $\delta_{HI} - \delta_{DM}$ is significant, and increases as we go towards large overdensities in dark matter. The scatter becomes small

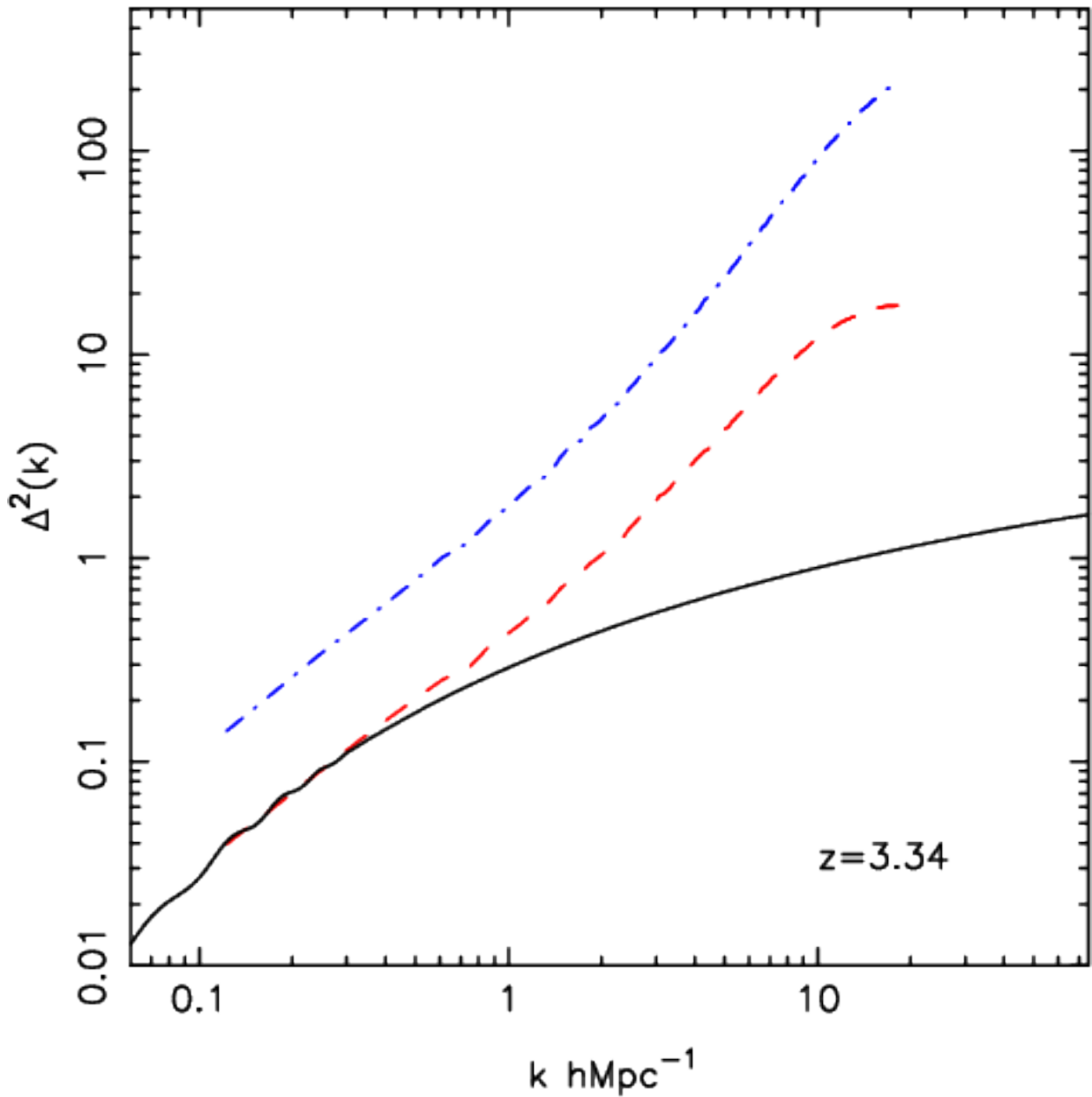


Figure 5.8: The power spectrum of fluctuations: the solid line shows the linearly extrapolated power spectrum, the dashed line shows the non-linear dark matter power spectrum and the dot-dashed line shows the HI power spectrum. All power spectra are for $z = 3.34$. The dark matter and the HI power spectra have been computed with the simulation with $L_{box} = 51.2 \text{ h}^{-1}\text{Mpc}$.

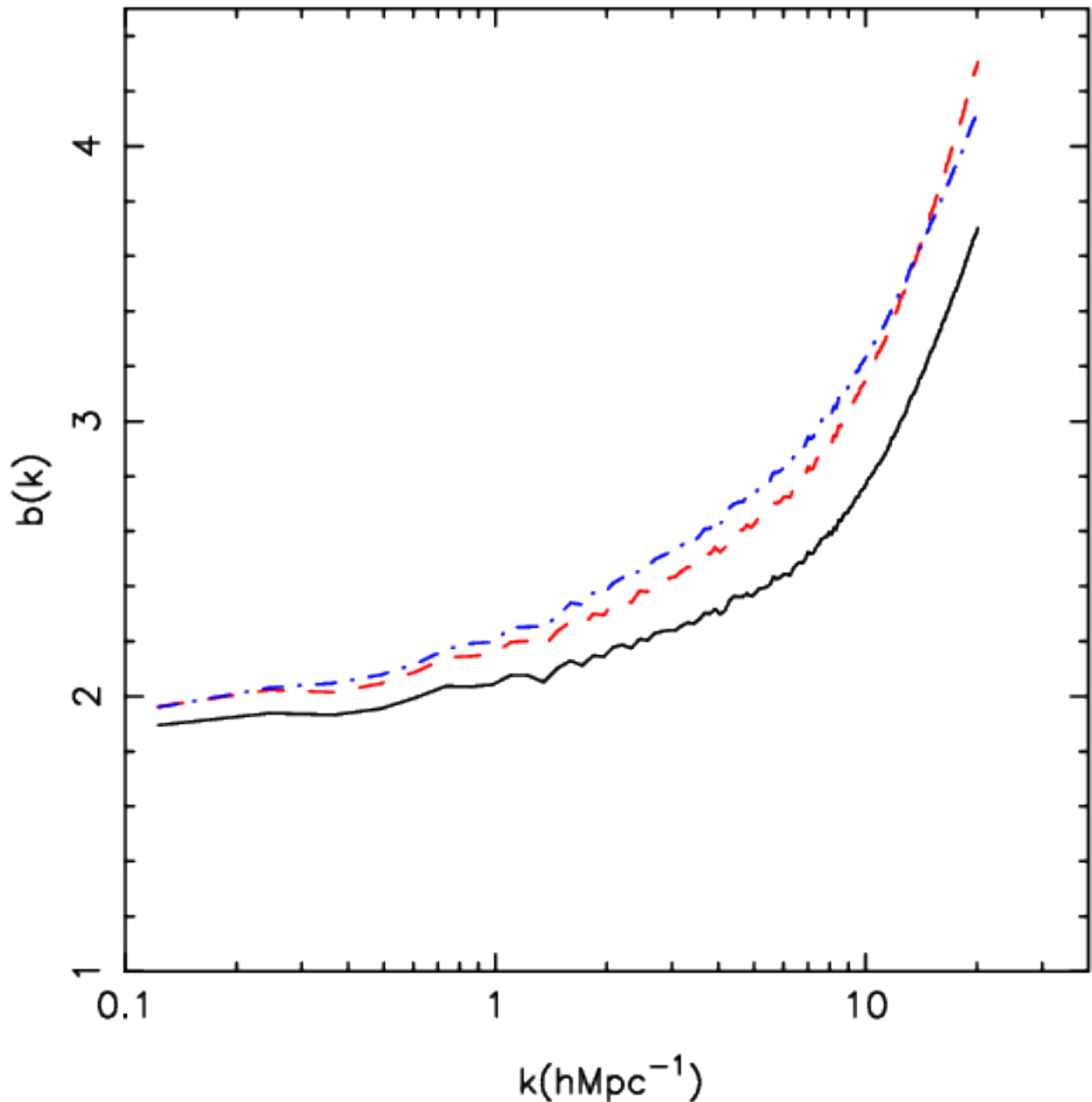


Figure 5.9: The dependance of bias on M_{min} and M_{max} . The solid curve shows $b(k)$ for the values of M_{min} and M_{max} shown in Table 5.1. The dashed line shows $b(k)$ when we use the reference value for M_{max} but increase M_{min} to twice the reference value. The dot-dashed curve shows $b(k)$ when M_{max} is chosen to be higher: $10^{11.9} M_\odot$, while M_{min} is kept at the reference value. We see that as the characteristic mass of haloes with HI increases, $b(k)$ increases. All curves are for $z = 3.34$ and have been computed with the simulation with $L_{box} = 51.2 \text{ h}^{-1}\text{Mpc}$.

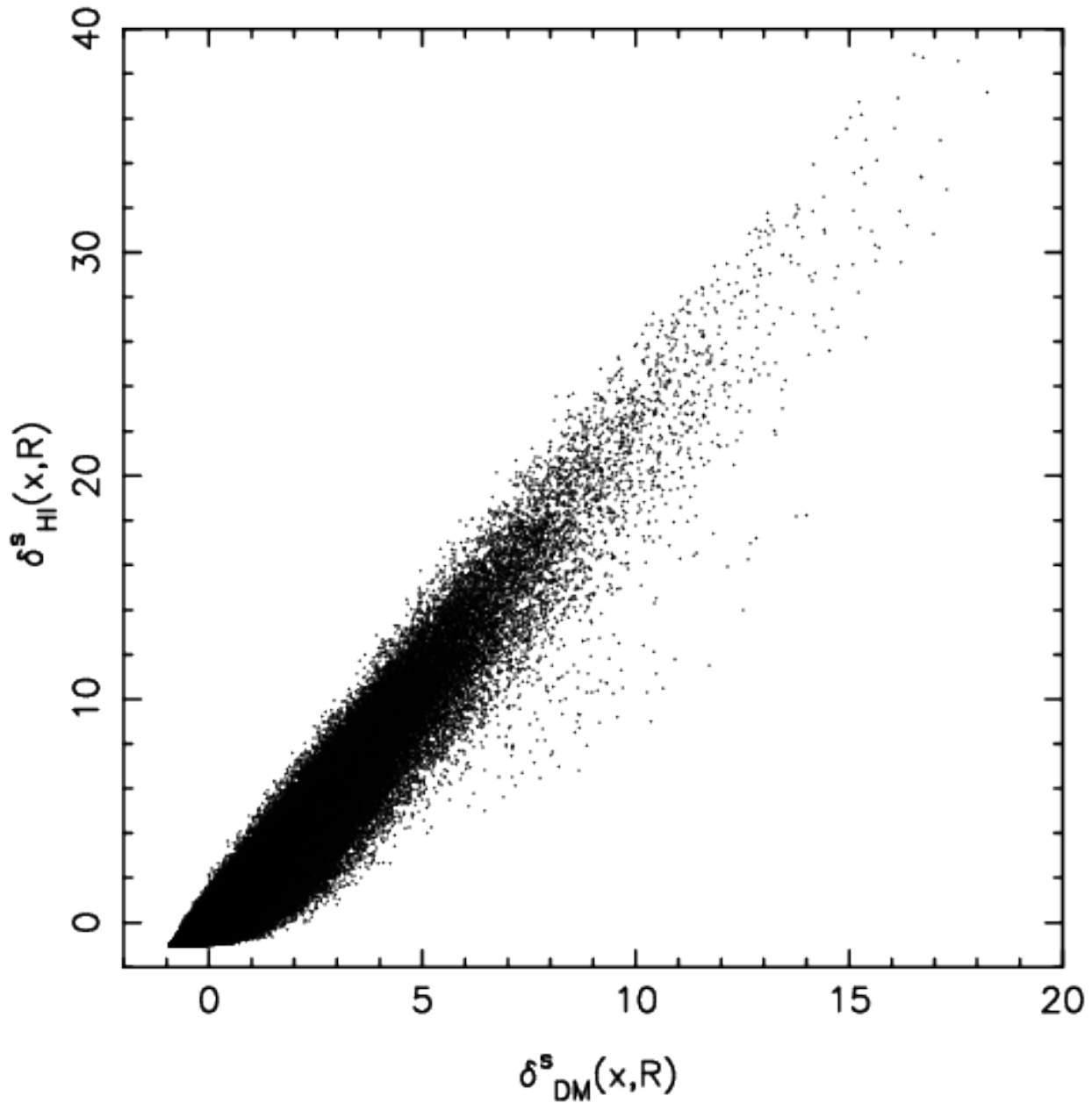


Figure 5.10: This figure shows a scatter plot of δ_{HI} smoothed at a scale of $3h^{-1}\text{Mpc}$ with spherical top hat window, plotted as a function of δ_{DM} smoothed at the same scale. The figure shows a random subset of points from the simulation with $L_{box} = 51.2 h^{-1}\text{Mpc}$ at $z = 3.34$.

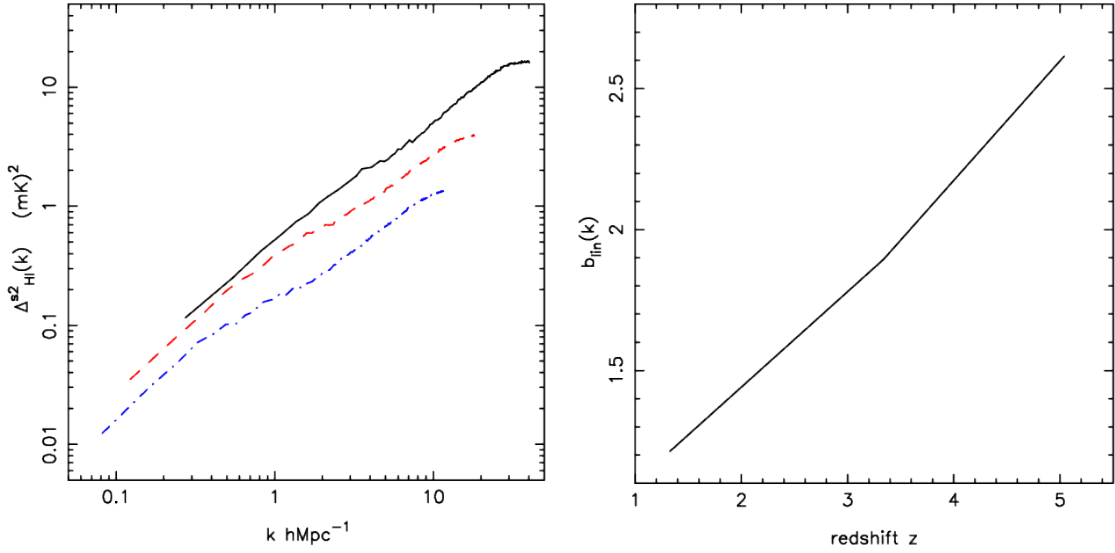


Figure 5.11: *Left:* Evolution of the HI powerspectrum $\Delta_{HI}^2(k)$. Solid, dashed, dot-dashed lines are for redshifts $z = 5.04, 3.34, 1.33$ respectively. *Right:* Evolution of the HI linear bias.

if we smooth the density distribution at much larger scales.

Similar results concerning the effect of non-linear gravitational clustering and bias are obtained for other redshifts. We concentrate on the evolution of bias and the power spectrum rather than go into a very detailed discussion of the HI distribution at each redshift. We discuss simulated maps in the following subsection.

Figure 5.11 (left panel) shows the evolution of the redshift space power spectrum for the HI distribution. Curves show the $\Delta_{HI}^2(k)$ as a function of k for $z = 5.1$ (solid line), $z = 3.34$ (dashed line) and $z = 1.3$ (dot-dashed line). Unlike the power spectrum in real space, the enhancement at very small scales is less strong and this is due to velocity dispersion within haloes at smaller scales. Power at larger scales is enhanced due to the Kaiser effect (Kaiser, 1987), leading to a relatively stronger enhancement at larger scales. Even though the amplitude of density perturbations increases with time, we see that the amplitude of brightness temperature fluctuations decreases instead. This is a manifestation of the decreasing correlation function, see, e.g., Bagla (1998b); Roukema & Valls-Gabaud

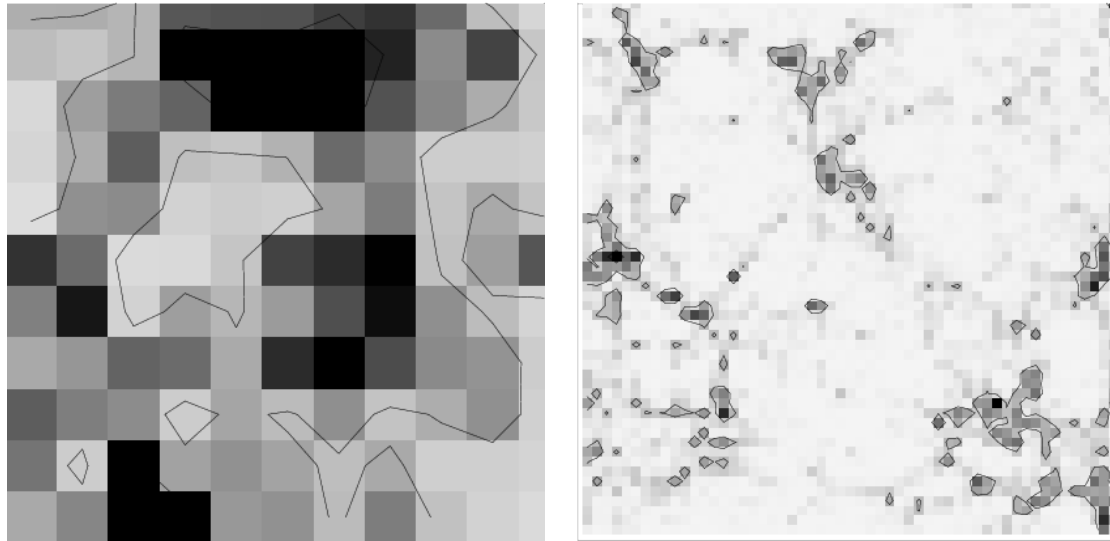


Figure 5.12: This figure shows shows mock radio maps, the left panel is for $z = 3.34$ and the right panel is for $z = 1.3$. The pixel size is chosen to be the resolution of the central square of the GMRT. The bandwidth of the map is 0.5MHz and 1.0MHz for $z = 3.34$, 1.33 respectively. The corresponding contours mark regions with signal $(9.2, 5.75, 1.15) \mu\text{Jy}$ and $(16.8, 10.5, 2.1) \mu\text{Jy}$ for $z = 3.34$ and 1.33 respectively. The mock maps show the brightest regions from the simulation. As we can see, these regions have a large angular extent this fact may be used to enhance prospects of detection.

(1998).

The evolution of bias at large scales, denoted as $b_{lin}(k)$ to emphasise that it refers to scales where clustering is still in the linear regime, is shown in the right panel of Figure 5.11. We see that this decreases from around 2.5 at $z = 5.1$ to 1.2 at $z = 1.3$, the variation is slightly steeper than $(1 + z)^{1/2}$ and hence the gradual lowering of the amplitude of the brightness temperature power spectrum.

5.3.2 Radio Maps

Figure 5.12 shows the simulated radio maps and spectra. The top row shows simulated radio maps, the left panel is for $z = 3.34$ and the right panel is for $z = 1.3$. The pixel size is chosen to be the same as the resolution of the central square of the GMRT. The bandwidth of the map is 0.5MHz and 1.0MHz for $z = 3.34$, 1.33 respectively. The corresponding contours mark regions with signal (9.2, 5.75, 1.15) μJy for $z = 3.34$ and (16.8, 10.5, 2.1) μJy for $z = 1.33$. As we can see in these maps, bright regions have a large angular extent this fact may be used to enhance prospects of detection.

Figure 5.13 shows spectra from the mock radio maps. These spectra have been plotted for regions that are the size of the resolution of the central square of the GMRT. We have chosen to plot the spectrum through the brightest region in the simulation. The left panel corresponds to $z = 3.34$ and the right panel shows the spectrum for $z = 1.3$. The peak flux is around 0.025 mJy and the FWHM of the line is close to 300 MHz. The strength of the signal for $z = 3.34$ is comparable to what we found in an earlier study, although the line width is much smaller. The reason for a smaller line width is likely to be the suppression of the HI fraction in very massive haloes. Considering the peak for which the spectrum has been plotted here, it may be possible to make a 2σ detection with about 2×10^3 hours of observations with the central square of the GMRT. Given that the GMRT observes a much larger volume at these redshifts than the simulation volume, it is highly probable that even rarer peaks in the HI distribution will be observed in a generic pointing.

The strength of the predicted signal at $z = 1.3$ is of the order of 0.05 mJy, with an FWHM of around 1 MHz. The best *rms* sensitivity achieved in this band at the GMRT is 0.02 mJy. This has been achieved with a bandwidth $\simeq 32$ MHz⁶. Thus direct detection of “clusters” of HI at $z \simeq 1.3$ is well within reach for the GMRT. Indeed, a simple estimate of noise in image suggests that a 2σ detection of such a rare peak in the HI distribution should be possible with around 400 hours of observation with the GMRT. As we shall show, it is possible to make a 2σ statistical detection of the redshifted 21 cm radiation from this epoch with about 10^3 hours of observations with the GMRT.

Detection of rare peaks in the HI distribution offers exciting possibilities. The size

⁶See http://www.gmrt.ncra.tifr.res.in/gmrt_hpage/Users/doc/GMRT_specs_June09.pdf

of the region represented in these rare peaks is fairly large, and it should be possible to establish the mass contained in these regions using observations in other wavebands. This will allow us to estimate Ω_{HI} in emission, and hence provide an independent measurement of the amount of cold gas.

The time required for detection of HI at high redshifts with the GMRT increases rapidly as we go to higher redshifts. This trend continues as we move to $z \simeq 5.1$ and therefore we do not discuss those results in detail here.

Upcoming instruments like the MWA can, however, detect signal from the HI distribution at high redshifts. The angular resolution of the MWA is fairly poor and hence the effects of non-linear clustering and scale dependant bias do not make a significant impact on predictions. We shall discuss the prospects for detection with the GMRT and the MWA in detail in the following chapter.

5.4 Discussion

Several attempts have been made in recent years to model the HI distribution in the post-reionization universe (Scott & Rees, 1990; Subramanian & Padmanabhan, 1993; Kumar, Padmanabhan, & Subramanian, 1995; Bagla, Nath, & Padmanabhan, 1997; Bharadwaj, Nath, & Sethi, 2001; Bharadwaj & Sethi, 2001; Bagla & White, 2003; Bharadwaj & Srikant, 2004; Bharadwaj & Ali, 2005; Loeb & Wyithe, 2008; Wyithe, Loeb, & Geil, 2008; Pritchard & Loeb, 2008), with the recent resurgence in interest being due to upcoming radio telescopes and arrays. In this paper we have revisited the issue using dark matter simulations and an ansatze for assigning HI to dark matter haloes. This is amongst the few attempts made using simulations where the smallest haloes that may contain significant amount of HI are resolved, and, the simulations are large enough to limit errors caused by a finite box size.

Our key conclusions may be summarized as follows:

- We have demonstrated that changes in the HI assignment schemes do not lead to significant variations in the statistics of the resulting HI distribution at large scales.
- We have shown that the finite box size effects are not important in even the smallest

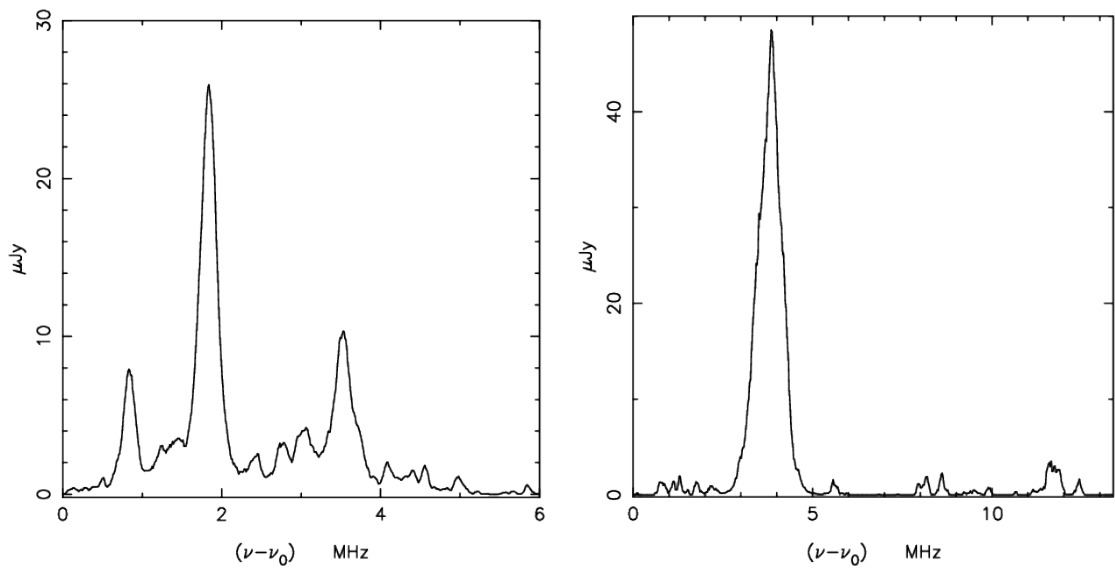


Figure 5.13: This figure shows spectra from the mock radio maps. These spectra have been plotted for regions that are the size of the resolution of the central square of the GMRT for $z = 3.34$ and twice the resolution of the central square of GMRT for $z = 1.33$. We chose to plot the spectrum through the brightest region in the simulation. The left panel corresponds to $z = 3.34$ and the right panel shows the spectrum for $z = 1.3$. The strength of the signal for $z = 3.34$ is comparable to what we found in an earlier study. The strength of the predicted signal at $z = 1.3$ is of the order of 0.05 mJy, with an FWHM of around 1 MHz. The best *rms* sensitivity achieved in this band at the GMRT is 0.02 mJy. This has been achieved with a bandwidth $\simeq 32$ MHz.

simulation we have used here.

- We find that non-linear gravitational clustering enhances the amplitude of perturbations by a significant amount at small scales.
- HI distribution is strongly biased at high redshifts and this enhances the HI power spectrum significantly as compared to the dark matter power spectrum. Bias $b(k)$ is scale independent at large scales $k \leq k_{nl}$, where k_{nl} is the scale of non-linearity.
- Bias decreases sharply from high redshifts towards low redshifts. This leads to a gradual decrease in the brightness temperature power spectrum. The change in the amplitude of the brightness temperature power spectrum is slow, being less than a factor two between $z = 5.1$ and $z = 1.3$.
- Brightest regions in the simulated radio maps are found to be extended, with an angular extent much larger than the resolution of the GMRT. This can be used to enhance prospects of detection.
- Spectra in the simulated maps appear to have an FWHM of around 1 MHz for $z = 1.3$ and about half of this for $z = 3.34$. A comparison with earlier work for $z = 3.34$ shows that the FWHM is found to be smaller in the present work. We attribute this to the low HI fraction assigned to the most massive haloes, whereas such haloes were not excluded in earlier work.
- Signal for the brightest source of redshifted 21 cm radiation from $z = 1.3$ appears to be significant, and within reach of an instrument like the GMRT.
- Detection of rare peaks in the HI distribution offers exciting possibilities. The size of the region represented in these rare peaks is fairly large, and it should be easy to establish the mass contained in these regions using observations in other wavebands. This may allow us to estimate Ω_{HI} in emission, and hence provide an independent measurement of the amount of cold gas.

We use the simulated maps to make estimates for prospects of detection using the GMRT and the MWA in the following chapter.

An interesting potential application of the method used here is to make predictions for $z < 1$ where detection with the GMRT and ASKAP is likely to be much easier. The main issue to be addressed there is that the observed volume becomes small and hence we can expect significant scatter in the observed visibility correlations from one field to another, and across frequency channels. This is particularly relevant for the GMRT where the primary beam covers a solid angle that is nearly 14 times smaller than that covered by ASKAP.

In this work we have used a fairly simple HI assignment scheme while ignoring the evolution of gas content of haloes. This is an aspect where there is a lot of scope for improvement.

Chapter 6

HI as a Probe of the Large Scale Structure in the Post-Reionization Universe: Visibility Correlations and Prospects for Detection

Simulated maps of the HI distribution in the post-reionization era are used to study the prospects for detection with existing and upcoming radio telescopes. We consider detection in the redshifted radiation from the hyperfine transition with a rest frame frequency of 1420 MHz. Possibility of a statistical detection using visibility correlations is discussed. We look at prospects for detection with the MWA¹, GMRT² and the hypothetical upgraded MWA, the MWA5000, often considered in the literature. The MWA5000 can detect visibility correlations at large angular scales at all redshifts in the post-reionization era. The GMRT can detect visibility correlations at lower redshifts, specifically there is a strong case for a survey at $z \simeq 1.3$. We also discuss prospects for direct detection of rare peaks in the HI distribution using the GMRT. We show that direct detection should be possible with integration time that is comparable to, or even less than, the time required for a statistical

¹ The Murchison Widefield Array. See <http://www.mwatelescope.org/> for details.

²Giant Meterwave Radio Telescope. See <http://gmrt.ncra.tifr.res.in> for details.

Table 6.1: Characteristics of the GMRT, MWA and MWA5000 that have been used for calculation of the visibility correlation and noise in the visibility correlation as well as noise in image are listed here. The values of the system parameters for GMRT and MWA were taken from <http://gmrt.ncra.tifr.res.in/> and Bowman (2007) respectively.

Instrument	Freq. (MHz)	$\Delta\nu$ (MHz)	B (MHz)	ΔU	θ_0 (deg.)	T_{sys} (K)	$A_{eff}(m^2)$
GMRT	610	1	16	32	0.56	102	1590
	330	1	16	17	1.03	106	1590
	235	1	16	12	1.45	237	1590
MWA	< 300	1	32	2	9	68	5.6
MWA5000	< 235	1	32	1.6	11.49	92	15

detection.

In the last chapter we studied the evolution of the HI distribution at high redshifts using N-Body simulations. We used the simulations to compute the power spectrum for the HI distribution at several redshifts. In this study we use the power spectra to compute visibility correlations using the relation enunciated by Bharadwaj & Sethi (2001). We estimate the level of noise for the GMRT and the MWA and compare these with the expected signal. We also discuss prospects for direct detection of rare peaks in the HI distribution. The basics theory is reviewed in §6.1. We summarize the simulations results in §6.2 and proceed to discuss the resulting visibility correlations in §6.2.1 where we also compare these with the expected noise. The signal expected from rare peaks is discussed in §6.2.2 along with prospects of direct detection of such peaks. We conclude with a discussion in §6.3.

6.1 Signal and Noise

In this section we briefly review the relation between the flux from sources and the observable quantities for radio interferometers. We then proceed to a discussion of the sensitivity

of interferometers and the corresponding limitations arising from that.

6.1.1 Visibility Correlation

The quantity measured in radio-interferometric observations is the visibility $V(\vec{U}, \nu)$ which is measured in a number of frequency channels $\nu - \nu\Delta\nu$ across a frequency bandwidth B for every pair of antennas in the array. The visibility is related to the sky specific intensity pattern $I_\nu(\vec{\theta})$ as

$$V(\vec{U}, \nu) = \int d^2\vec{\theta} A(\vec{\theta}) I_\nu(\vec{\theta}) e^{2\pi i \vec{\theta} \cdot \vec{U}}. \quad (6.1)$$

The baseline \vec{U} is \vec{d}/λ where \vec{d} is the antenna separation projected in the plane perpendicular to the line of sight. $\vec{\theta}$ is a two dimensional vector in the plane of the sky with origin at the center of the field of view, and $A(\vec{\theta})$ is the beam pattern of the individual antenna. For the GMRT this can be well approximated by Gaussian $A(\vec{\theta}) = e^{-\theta^2/\theta_0^2}$. We use $\theta_0 = 0.56^\circ$ at 610 MHz for the GMRT, and it scales as the inverse of frequency.

We next consider the visibility-visiblity correlation (hereafter only visibility correlation) measured at different baselines \vec{U} and $\vec{U} + \vec{\Delta}U$, at two frequencies ν and $\nu + \Delta\nu$. As argued in Bharadwaj & Ali (2005) the visibilities at baselines U and $\vec{U} + \vec{\Delta}U$ will be correlated only if $|\Delta\vec{U}| < 1/\pi\theta_0$. Visibilities at different frequencies are expected to be correlated only if the flux from sources is correlated. This is certainly true of continuum radiation. In case of spectral lines, like the redshifted 21 cm line being considered here, visibilities are expected to be correlated over a range of frequencies comparable to width of spectral lines. For generic applications, we can take this to be about 1 MHz though we can use the simulated radio maps for a more refined model. As a first approximation, the visibilities at frequencies ν and $\nu + \Delta\nu$ can be assumed to be uncorrelated for $\Delta\nu > 1$ MHz (Datta, Choudhury, & Bharadwaj, 2007) for range of baselines of our interest. To calculate the strength and nature of visibility correlation we consider the visibility correlation at same baselines and frequencies which can be written as (for details see Bharadwaj & Ali (2005))

$$\langle V(\vec{U}, \nu) V^*(\vec{U}, \nu) \rangle = \frac{\bar{I}_\nu^2 \theta_0^2}{2r_\nu^2} \int_0^\infty dk_{\parallel} P_{\text{HI}}(k) \quad (6.2)$$

where r_ν is comoving distance corresponds to frequency $\nu = 1420/(1+z)$. $\vec{k} = k_{\parallel}\hat{m} + \frac{2\pi\vec{U}}{r_\nu}$,

where \hat{m} is unit vector along the line of sight. We next shift our focus on the redshift space HI power spectrum $P_{HI}(k, z)$ (Bharadwaj & Ali, 2004). In the post-reionization epoch HI survives mainly in the inter-stellar medium (ISM) of galaxies. At sufficiently large scales one can write $P_{HI}(k, z)$ as

$$P_{HI}(k, z) = x_{HI}^2 b^2 \left[1 + \beta(k) \frac{k_{\parallel}^2}{k^2} \right]^2 P(k, z). \quad (6.3)$$

Here x_{HI} is neutral Hydrogen (HI) fraction. b is the scale independent bias at large scales. $\beta(k) = f/b$ where $f = \Omega_{nr}^{0.6}$ is the redshift distortion parameter. $P(k, z)$ is matter power spectrum at redshift z and is dominated by the spatial distribution of dark matter. We calculate $P_{HI}(k, z)$ from N-Body simulations and put this in eq. 6.2 to calculate the visibility correlation. As simulations have a finite box size, we patch it with a linearly extrapolated power spectrum with a constant bias at small k .

6.1.2 System Noise in the Visibility Correlation

The noise rms. in real part in each visibility for single polarization is

$$V_{rms} = \frac{\sqrt{2}k_B T_{sys}}{A_{eff} \sqrt{\Delta\nu \Delta t}} \quad (6.4)$$

where T_{sys} is the total system temperature, k_B is the Boltzmann constant, A_{eff} is the effective collecting area of each antenna, $\Delta\nu$ is the channel width and Δt is correlator integration time. This can be written in terms of the antenna sensitivity $K = \frac{A_{eff}}{2k_B}$ as

$$V_{rms} = \frac{T_{sys}}{K \sqrt{2\Delta\nu \Delta t}} \quad (6.5)$$

The noise variance in the visibility correlation is written as (Ali, Bharadwaj, & Chengalur, 2008)

$$\sigma_{VV}^2 = \frac{8 V_{rms}^4}{N_p} \quad (6.6)$$

where N_p is number of visibility pairs in a particular U bin and frequency separation less than $\Delta\nu$. The HI signal part remains correlated but the system noise is uncorrelated in the visibility correlation.

We next consider how N_p is calculated. We consider an elementary grid of area ΔU^2 in the $u - v$ plane where the signal remains correlated. Total observation time we consider is T . We further assume $\rho(U, \nu)$ (circularly symmetric) to be the baseline fraction per unit area per in the baseline range U and $U + \Delta U$. Number of visibility pairs in a given $U, \Delta\nu$ bin in the grid is

$$\frac{1}{2} \left[\frac{N(N-1)}{2} \frac{T}{\Delta t} \Delta U^2 \rho(U, \nu) \right]^2 \quad (6.7)$$

Note that the baseline fraction function $\rho(U, \nu)$ is different for different interferometric arrays and plays an important role in determining the sensitivity of an array. This function is also frequency dependent. The signal and the system noise is expected to be isotropic and only depends on the magnitude of U . We take average over all bins of area ΔU^2 in the circular annulus between U and $U + \Delta U$. Number of independent elementary bins in a circular annulus between U and $U + \Delta U$ is $2\pi U \Delta U / \Delta U^2$. Moreover there are $B/\Delta\nu$ independent channels for the total bandwidth B . Combining all these we have

$$N_p = \frac{1}{2} \left[\frac{N(N-1)}{2} \frac{T}{\Delta t} \Delta U^2 \rho(U, \nu) \right]^2 \frac{B}{\Delta\nu} \frac{2\pi U \Delta U}{\Delta U^2} \quad (6.8)$$

The noise rms in the visibility correlation can then be written as

$$\sigma_{VV} = \frac{4}{\sqrt{2\pi} N(N-1)} \left[\frac{T_{sys}}{K} \right]^2 \frac{1}{T \sqrt{\Delta\nu B}} \frac{1}{U^{0.5} \Delta U^{1.5} \rho(U, \nu)} \quad (6.9)$$

The bin size ΔU is determined by the field of view of the antenna and for a Gaussian antenna beam pattern $A(\theta) = e^{-\theta^2/\theta_0^2}$, one can show that $\Delta U = 1/\pi\theta_0$. The equation 6.9 gives the system noise in the visibility correlation for any radio experiment. Note that, the system noise *rms* in the visibility correlation scales as $\sim 1/N(N-1)T$ unlike the noise rms in the image which scales as $\sim 1/\sqrt{N(N-1)T}$.

There are two effects that we ignore in the analysis here.

- At small U , comparable with the inverse of the field of view, cosmic variance also limits our ability to measure the visibility correlations. As the field of view of the GMRT is (much) smaller than the MWA, this concern is more relevant in that case. Cosmic variance is subdominant to the system noise as long as we work with scales

that are much smaller than the field of view, or work with U that are much larger than the one that corresponds to the field of view.

- For MWA, the field of view is very large and one needs to take the curvature of sky into account (McEwen & Scaife, 2008; Ng, 2001, 2005). We ignore this as we are not estimating the signal at very large angles.

We consider three instruments: the GMRT, MWA and a hypothetical instrument MWA5000. The GMRT has a hybrid distribution with 14 antennae are distributed randomly in the central core of area $1 \text{ km} \times 1 \text{ km}$ and 16 antennae are placed along three arms (Y shaped). The antennae are parabolic dishes of diameter 45 m. The MWA will have 500 antennae distributed within a circular region of radius 750 m. The antennae are expected to follow $\rho_{ant}(r) \propto 1/r^2$ distribution with a 20 m flat core. The hypothetical instrument MWA5000 is almost similar to the MWA but with 5000 antennae. We assume antennae are distributed as $\rho_{ant}(r) \propto 1/r^2$ within 1000 m radius and with a flat core of radius 80 m (McQuinn et al., 2006). The normalized baseline distribution $\rho(U, \nu)$ for frequency $\nu = 330 \text{ MHz}$ is presented in the Figure 6.1 for the three instruments (see Datta et al. (2007) for details). Table 6.1 lists the wavebands and other instrument parameters for which analysis is done in this paper. We assume the effective antenna collecting area (A_{eff}) to be same as the antenna physical area. We also list parameters used for calculation of noise in visibility correlations.

We consider three instruments: the GMRT, MWA and a hypothetical instrument MWA5000. The GMRT has a hybrid distribution with 14 antennae are distributed randomly in the central core of area $1 \text{ km} \times 1 \text{ km}$ and 16 antennae are placed along three arms (Y shaped). The antennae are parabolic dishes of diameter 45 m. The MWA will have 500 antennae distributed within a circular region of radius 750 m. The antennae are expected to follow $\rho_{ant}(r) \propto 1/r^2$ distribution with a 20 m flat core. The hypothetical instrument MWA5000 is almost similar to the MWA but with 5000 antennae. We assume antennae are distributed as $\rho_{ant}(r) \propto 1/r^2$ within 1000 m radius and with a flat core of radius 80 m (McQuinn et al., 2006). The normalized baseline distribution $\rho(U, \nu)$ for frequency $\nu = 330 \text{ MHz}$ is presented in the Figure 6.1 for the three instruments (see Datta et al. (2007) for details). Table 6.1 lists the wavebands and other instrument parameters for

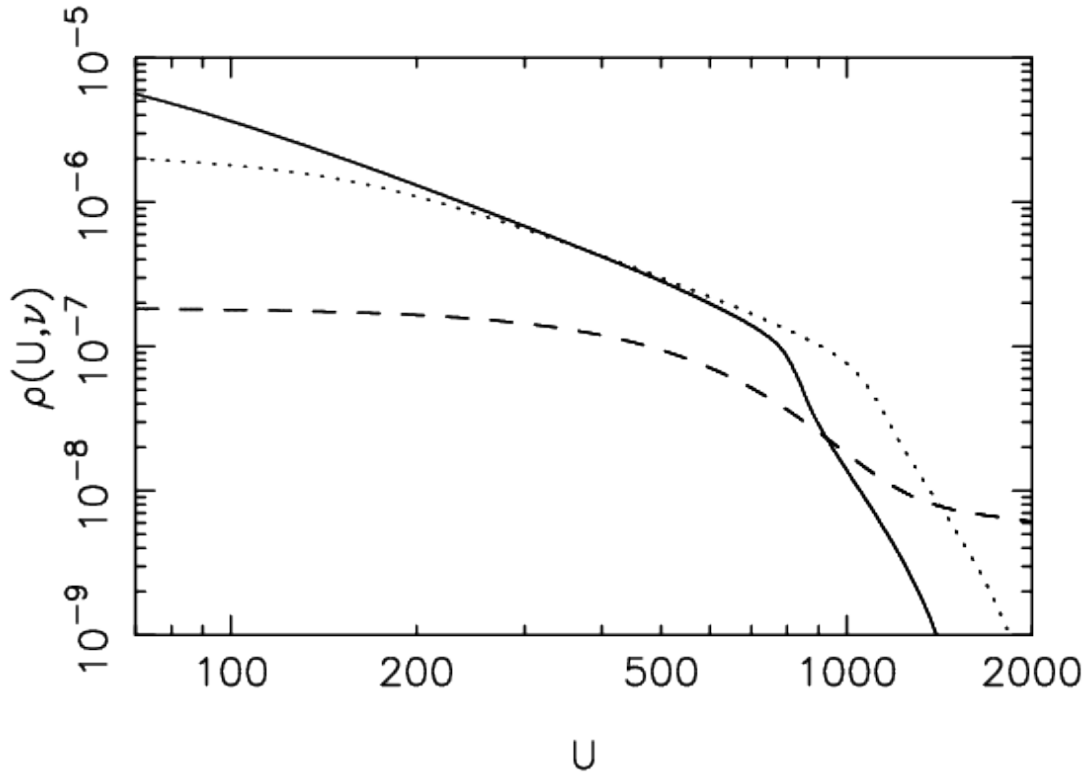


Figure 6.1: This shows the normalized baseline distribution function $\rho(U, \nu)$ as a function of baseline U for three instruments (GMRT, MWA and MWA5000) for frequency $\nu = 330$ MHz.

which analysis is done in this paper. We assume the effective antenna collecting area (A_{eff}) to be same as the antenna physical area. We also list parameters used for calculation of noise in visibility correlations.

6.1.3 Noise in Images

Observed visibilities are used to construct an image of the sky for each frequency channel. The size of the image is of the order of the primary beam θ_0 and the resolution depends on the largest baselines used. Both the size of the image and resolution, or the pixel size depend on the frequency of observation in the same manner.

Unlike visibilities, that are uncorrelated outside of the small bins, pixels in an image are not completely uncorrelated. The correlation of pixels in a raw image is similar to the *dirty beam*. Therefore the analysis of noise in images as a function of scale is a fairly complex problem. Scaling of noise with bandwidth is easy as the noise for different frequency channels is uncorrelated. *rms* noise for a given pixel can be computed:

$$\sigma_{image} = \frac{T_{sys}}{G} \frac{1}{\sqrt{\Delta t \Delta \nu} \sqrt{N(N-1)}} \quad (6.10)$$

Here G is the Gain for each antenna, T_{sys} is the system temperature, N is the number of antenna in the interferometer, Δt is the on source observation time and $\Delta \nu$ is the bandwidth for the image. We ignore foregrounds as at most frequencies of interest $T_{sys} \gg T_{sky}$. This assumption becomes invalid for redshifted 21 cm radiation from $z > 5$ and at these redshifts foregrounds present greater difficulties than the instrumental noise.

We find that for the $z = 3.3$ window of the GMRT $\sigma_{image} \simeq 9 \mu\text{Jy}$ for an integration time of 2000 hours and a bandwidth of 1 MHz. This has been computed for the central square of the GMRT with $N = 14$. The corresponding number of $z = 1.3$ is $\sigma_{image} \simeq 20 \mu\text{Jy}$ for an integration time of 400 hours and a bandwidth of 1 MHz.

As a first approximation, we assume that noise in images is uncorrelated and that it scales as the square root of the number of pixels over which signal is smoothed. This allows us to estimate signal to noise ratio for extended structures, but it must be noted that this analysis is approximate.

6.2 Simulated Maps & Signal

In this section we describe results from simulated HI maps. Details of the simulations we use here and the method used for assigning HI can be found in the previous chapter. We summarise some key aspects of the simulated HI distribution.

- We use gravity only simulations of the LCDM model with 512^3 particles. The simulations are run using the TreePM method (Bagla, 2002; Bagla & Ray, 2003; Khandai & Bagla, 2009).

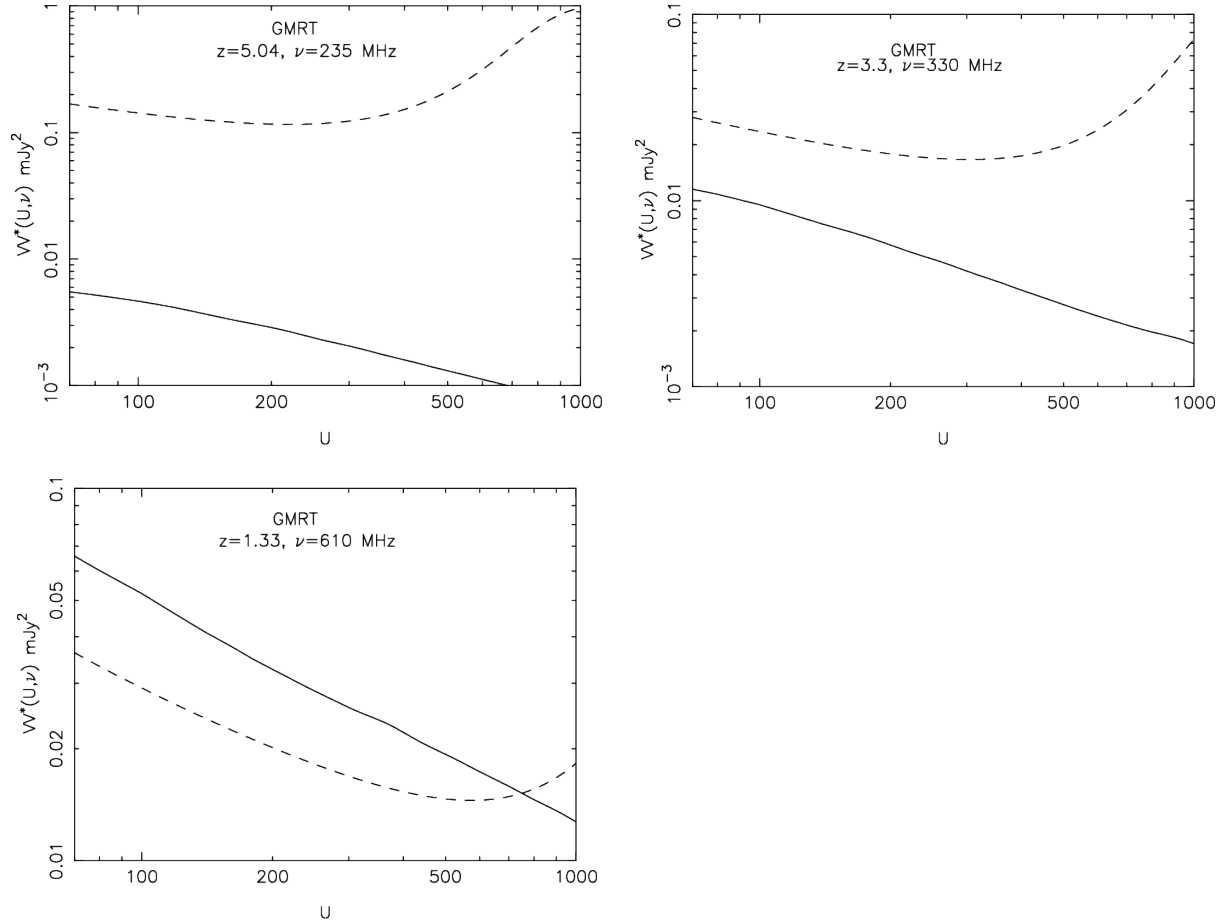


Figure 6.2: This figure shows the expected visibility correlation as a function of U for GMRT. The expected signal is shown with a solid curve and the expected noise in the visibility correlation is shown by a dashed curve. Different panels are for different redshifts. The noise in each panel has been computed assuming 10^3 hours of integration time and $\Delta\nu = 1 \text{ MHz}$. We have ignored the effect of foregrounds and only the system noise has been considered. Prospects of detection with the GMRT are encouraging for $z = 1.3$ where it should be possible to make a detection for $U < 700$. It is possible to enhance the signal to noise ratio by combining data from nearby bins in U , thus detection may be possible in a shorter time scale as well.

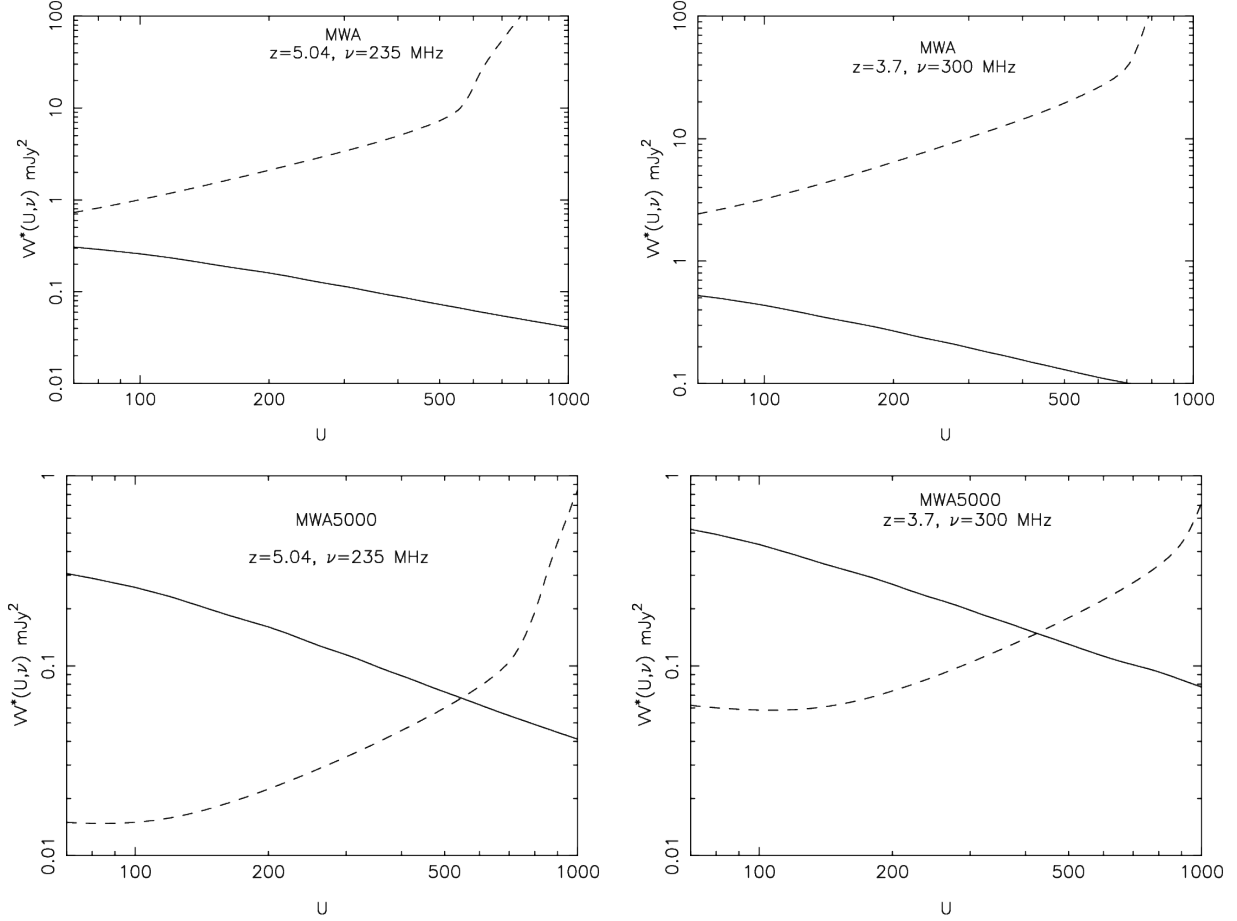


Figure 6.3: This figure shows the expected visibility correlation as a function of U for MWA and MWA5000. The expected signal is shown with a solid curve and the expected noise in the visibility correlation is shown by a dashed curve. Different panels are for different redshifts. The noise in each panel has been computed assuming 10^3 hours of integration time and a bandwidth of 1 MHz. We have ignored the effect of foregrounds and only the system noise has been considered. We note that the MWA5000 should detect visibility correlations at $U < 500$ at $z \simeq 5$ and at $U < 400$ at $z \simeq 3.7$. The detection at smaller U should be possible at a high significance level. It is possible to enhance the signal to noise ratio by combining data from nearby bins in U , thus detection may be possible in a shorter time scale as well.

- We identify haloes in these simulations. HI is assigned to haloes with circular velocity greater than 30 km/s. Mass resolution of simulations is chosen such that haloes with this minimum circular velocity contain at least 8 particles.
- HI assignment scheme is chosen to be such that the HI fraction drops rapidly in haloes with circular velocity greater than 200 km/s. For more massive haloes, the HI mass goes to a constant.
- It is assumed that particles not contained in these haloes do not have any neutral Hydrogen.
- Positions, velocities and HI mass of particles is then used to generate simulated maps, as well as to compute statistical quantities like the power spectrum and scale dependant bias.

6.2.1 Visibility Correlation

We use the power spectrum of the HI distribution derived from N-Body simulations to compute the visibility correlations. For large scales, larger than the simulation size, we patch this with the linearly extrapolated power spectrum with a constant bias. This is the only input required in Eqn.(6.2) for calculation of visibility correlation.

Visibility correlation for various redshifts is shown in Figures 6.2 and 6.3. We have also plotted the expected system noise in each of the panels. The expected visibility correlation is shown as a function of U . The expected signal is shown with a solid curve and the expected noise in the visibility correlation is shows by a dashed curve. This has been shown for the instruments: GMRT (figure 6.2) MWA (figure 6.3) and MWA5000. Different panels in the two columns are for different redshifts. The noise in each panel has been computed assuming 10^3 hours of integration time and $\Delta\nu = 1$ MHz. We have ignored the effect of foregrounds and only the system noise has been considered. Important conclusions that can be drawn from these figure are as follows:

- The MWA in its current design will not be able to detect visibility correlations.

- The MWA5000 should detect visibility correlations at $U < 500$ at $z \simeq 5$ and at $U < 400$ at $z \simeq 3.7$.
- The detection at smaller U should be possible at a high significance level.
- Prospects of detection with the GMRT are encouraging for $z = 1.3$ where it should be possible to make a detection for $U < 700$.

It is possible to enhance the signal to noise ratio by combining data from nearby bins in U , thus detection may be possible in a shorter time scale as well. The GMRT has been in operation for more than a decade, and its characteristics are well understood. Therefore it is important to make an effort to observe HI fluctuations at $z \simeq 1.3$ with the instrument. The observations need not pertain to the same field as the region observed by the GMRT in a single observation is fairly large and we do not expect significant fluctuations in the HI power spectrum and hence the visibility correlation from one field to another. Thus good quality archival data for a few fields can be combined, in principle, to detect visibility correlations.

Detection of visibility correlations in turn gives us a measurement of the power spectrum for the HI distribution (Bharadwaj & Sethi, 2001). This can be used to constrain various cosmological parameters (Bharadwaj, Sethi, & Saini, 2009; Wyithe, Loeb, & Geil, 2008). Recently, it has also been pointed out that the power spectrum can also be used to estimate the characteristic mass of damped lyman alpha systems (DLAS) (Wyithe, 2008).

6.2.2 Rare Peaks

We now discuss the possibility of directly detecting rare peaks in the HI distribution. This is an interesting possibility for instruments like the GMRT and ASKAP that can resolve small angular scales. At such scales, non-linear gravitational clustering and the large bias for the HI distribution combine to enhance the amplitude of fluctuations significantly. It is also of interest to see whether this enhancement can make detection of rare peaks as easy as statistical detection via visibility correlations.

Figure 6.4 shows the expected signal to noise ratio (SNR) for the brightest region in the simulated maps if it is observed using the central square of the GMRT. The left column

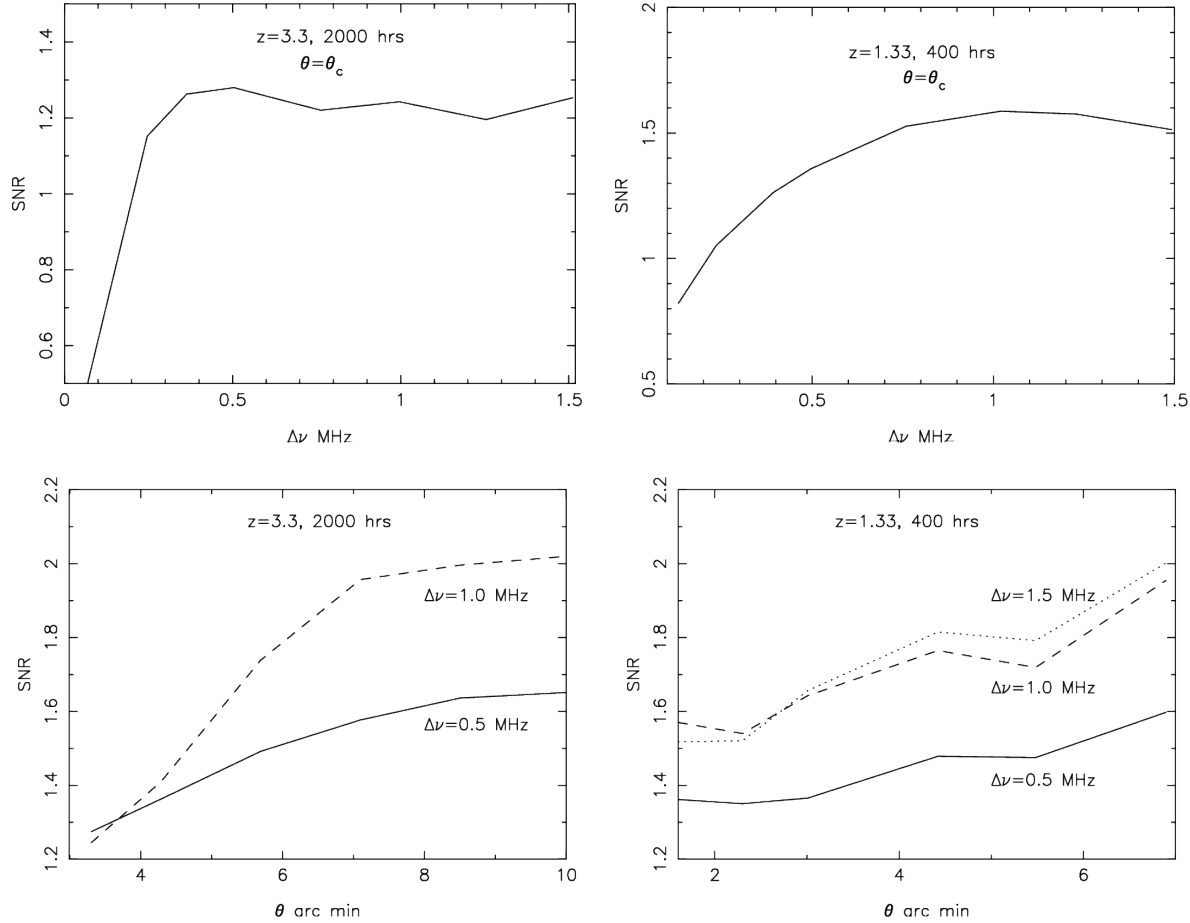


Figure 6.4: This figure shows the expected signal to noise ratio (SNR) for direct detection of rare peaks in the HI distribution at high redshifts. All the plots pertain to the GMRT and we use the expected noise in the image for the central square. The left column is for $z \approx 3.3$ and the right column is for $z \approx 1.3$. The top row is for variation of the SNR with bandwidth for one pixel, whereas the lower shows the variation of SNR with the square root of the solid angle over which signal has been smoothed for a given bandwidth. These figures show that a 2σ detection of a rare peak is possible in 400 hours for $z \approx 1.3$ and in 2000 hours for $z \approx 3.3$.

is for $z \simeq 3.3$ and the right column is for $z \simeq 1.3$. The top row shows variation of the SNR with bandwidth for one pixel, whereas the lower shows the variation of SNR with the square root of the solid angle over which signal has been smoothed for a given bandwidth. In plots of variation of SNR with the bandwidth, the peak is very close to the FWHM of spectral lines for large structures (see spectra of rare peaks in Bagla & Khandai (2009)).

These figures show that a 2σ detection of a rare peak is possible in 400 hours for $z \simeq 1.3$ and in 2000 hours for $z \simeq 3.3$. The time for detection here is comparable to, indeed slightly less than the time required for a statistical detection. This is a very exciting possibility as it allows us to measure the HI fraction of a fairly large region, potentially leading to a measurement of Ω_{HI} . However, unlike statistical detection of the HI distribution, the integration time cannot be divided across different fields for a direct detection.

The volume sampled in observation of one field with the GMRT at $z \simeq 3.3$ is much larger than the volume of the simulation used here. Thus there is a strong possibility of finding an even brighter region in a random pointing at that redshift. On the other hand, the volume sampled by the GMRT at $z \simeq 1.3$ is comparable to the volume of the simulation used for making mock maps.

6.3 Discussion

The prospects for detection of the HI distribution at high redshifts are very promising. We can expect an upgraded form of MWA, the MWA5000, often considered in the literature to measure visibility correlations at $z > 3.7$ and provide an estimate of the power spectrum. The GMRT can be used to measure visibility correlations at $z \simeq 1.3$. The integration time required is not very large. This is very encouraging as no other existing or upcoming instrument can probe this redshift, though ASKAP will be able to probe the HI distribution at $z < 1$. Measurement of visibility correlations, and hence the HI power spectrum can be used to constrain several cosmological parameters. If we are able to make measurements at several redshifts then it becomes possible to constrain models of dark energy.

Direct detection of rare peaks in the HI distributions does not require a much longer integration time as compared to statistical detection. The direct detection at $z \simeq 1.3$

requires only a few hundred hours of observing time with an existing instrument. Unlike statistical detection of fluctuations that are not dependant on the average HI fraction, such observations may be used in combination with other observations to constrain Ω_{HI} .

It is obvious that detection of rare peaks of HI with the GMRT may be even easier at lower redshifts ($z \leq 0.4$). However, the field of view of the GMRT for redshift 21 cm radiation is very small and hence one may need to observe several fields before finding a very bright object. Or one may need to observe for longer periods of time in order to observe a not so rare peak.

Appendix

Appendix A

Expressions for Cubic Spline Softened Potential and Force Kernels

One can integrate the Poisson equation for a given kernel to obtain the softened two-body potential kernel. For the case of the cubic spline kernel we have the expression for the two-body potential kernel $\phi(\mathbf{u}, \epsilon)$ and the regular two-body force $\mathbf{f}(\mathbf{u}, \epsilon) = -\nabla_{\mathbf{u}}\phi$:

$$\phi(\mathbf{u}, \epsilon) = \begin{cases} \frac{16}{\epsilon} \left[\frac{1}{3} \left(\frac{u}{\epsilon} \right)^2 - \frac{3}{5} \left(\frac{u}{\epsilon} \right)^4 + \frac{2}{5} \left(\frac{u}{\epsilon} \right)^5 \right] - \frac{14}{5\epsilon}, & 0 \leq \frac{u}{\epsilon} < 0.5 \\ \frac{1}{\epsilon} \left[\frac{1}{15} \left(\frac{u}{\epsilon} \right) + \frac{32}{3} \left(\frac{u}{\epsilon} \right)^2 - \frac{16}{1} \left(\frac{u}{\epsilon} \right)^3 + \frac{48}{5} \left(\frac{u}{\epsilon} \right)^4 - \frac{32}{15} \left(\frac{u}{\epsilon} \right)^5 \right] - \frac{16}{5\epsilon}, & 0.5 \leq \frac{u}{\epsilon} < 1.0 \\ -\frac{1}{u}, & 1.0 \leq \frac{u}{\epsilon} \end{cases} \quad (\text{A1})$$

$$\mathbf{f}(\mathbf{u}, \epsilon) = \begin{cases} -\frac{32\mathbf{u}}{\epsilon^3} \left[\frac{1}{3} - \frac{6}{5} \left(\frac{u}{\epsilon} \right)^2 + \left(\frac{u}{\epsilon} \right)^3 \right], & 0 \leq \frac{u}{\epsilon} < 0.5 \\ -\frac{\mathbf{u}}{\epsilon^3} \left[-\frac{1}{15} \left(\frac{u}{\epsilon} \right)^3 + \frac{64}{3} - \frac{48u}{\epsilon} + \frac{192}{5} \left(\frac{u}{\epsilon} \right)^2 - \frac{32}{3} \left(\frac{u}{\epsilon} \right)^3 \right], & 0.5 \leq \frac{u}{\epsilon} < 1.0 \\ -\frac{\mathbf{u}}{u^3}, & 1.0 \leq \frac{u}{\epsilon} \end{cases} \quad (\text{A2})$$

For variable or local smoothing length $\epsilon_i \equiv \epsilon(\mathbf{r}_i)$ there will be an additional term given in eqs.(10-12) for which one needs to compute $(\partial W/\partial\epsilon)$, $(\partial W/\partial\mathbf{u})$ and $(\partial\phi/\partial\epsilon)$ For the cubic spline kernel these expressions are:

$$\frac{\partial W}{\partial\epsilon} = \frac{8}{\pi\epsilon^4} \begin{cases} 3 \left[-1 + 10 \left(\frac{u}{\epsilon} \right)^2 - 12 \left(\frac{u}{\epsilon} \right)^3 \right], & 0 \leq \frac{u}{\epsilon} < 0.5 \\ 6 \left[-1 + 4 \left(\frac{u}{\epsilon} \right) - 5 \left(\frac{u}{\epsilon} \right)^2 + 2 \left(\frac{u}{\epsilon} \right)^3 \right], & 0.5 \leq \frac{u}{\epsilon} < 1.0 \\ 0, & 1.0 \leq \frac{u}{\epsilon} \end{cases} \quad (\text{A3})$$

$$\frac{\partial W}{\partial\mathbf{u}} = \frac{48}{\pi\epsilon^4 u} \begin{cases} -2 \left(\frac{u}{\epsilon} \right) + 3 \left(\frac{u}{\epsilon} \right)^2 & 0 \leq \frac{u}{\epsilon} < 0.5 \\ -1 + 2 \left(\frac{u}{\epsilon} \right) - \left(\frac{u}{\epsilon} \right)^2 & 0.5 \leq \frac{u}{\epsilon} < 1.0 \\ 0, & 1.0 \leq \frac{u}{\epsilon} \end{cases} \quad (\text{A4})$$

$$\frac{\partial\phi}{\partial\epsilon} = \begin{cases} \frac{16}{\epsilon^2} \left[- \left(\frac{u}{\epsilon} \right)^2 + 3 \left(\frac{u}{\epsilon} \right)^4 - \frac{12}{5} \left(\frac{u}{\epsilon} \right)^5 \right] + \frac{14}{5\epsilon^2} & 0 \leq \frac{u}{\epsilon} < 0.5 \\ \frac{1}{\epsilon^2} \left[-32 \left(\frac{u}{\epsilon} \right)^2 + 64 \left(\frac{u}{\epsilon} \right)^3 - 48 \left(\frac{u}{\epsilon} \right)^4 + \frac{64}{5} \left(\frac{u}{\epsilon} \right)^5 \right] + \frac{16}{5\epsilon^2} & 0.5 \leq \frac{u}{\epsilon} < 1.0 \\ 0, & 1.0 \leq \frac{u}{\epsilon} \end{cases} \quad (\text{A5})$$

Bibliography

- Ali S. S., Bharadwaj S., Chengalur J. N., 2008, MNRAS, 385, 2166
- Athanassoula E., Fady E., Lambert J. C., Bosma A., 2000, MNRAS, 314, 475
- Bagla J. S., Padmanabhan T., 1994, MNRAS, 266, 227
- Bagla J. S., Padmanabhan T., 1997, Pramana, 49, 161
- Bagla J. S., Padmanabhan T., 1997, MNRAS, 286, 1023
- Bagla J. S., Nath B., Padmanabhan T., 1997, MNRAS, 289, 671
- Bagla J. S., 1998b, MNRAS, 299, 417
- Bagla J. S., 1998a, MNRAS, 297, 251
- Bagla J. S., 1999, ASPC, 156, 9
- Bagla J. S., 2002, JApA, 23, 185
- Bagla J. S., Ray S., 2003, NewA, 8, 665
- Bagla J. S., White M., 2003, ASPC, 289, 251
- Bagla J. S., Ray S., 2005, MNRAS, 358, 1076
- Bagla J. S., 2005, CSci, 88, 1088
- Bagla J. S., Prasad J., 2006, MNRAS, 370, 993

- Bagla J. S., Prasad J., 2008, arXiv, arXiv:0802.2796
- Bagla J. S., Prasad J., Khandai N., 2009, MNRAS, 395, 918
- Bagla J. S., Khandai N., 2009, MNRAS, 396, 2211
- Bagla J. S., Kulkarni G., Padmanabhan T., 2009, MNRAS, 397, 971
- Bagla J. S., Khandai N., arXiv:0908.3796
- Barnes J., Hut P., 1986, Natur, 324, 446
- Barnes J. E., 1990, JCoPh, 87, 161
- Barrow J. D., Saich P., 1993, MNRAS, 262, 717
- Bartelmann M., Huss A., Colberg J. M., Jenkins A., Pearce F. R., 1998, A&A, 330, 1
- Bartolo N., Matarrese S., Riotto A., 2005, JCAP, 10, 10
- Baugh C. M., Benson A. J., Cole S., Frenk C. S., Lacey C. G., 1999, MNRAS, 305, L21
- Becker R. H., et al., 2001, AJ, 122, 2850
- Benson A. J., Cole S., Frenk C. S., Baugh C. M., Lacey C. G., 2000, MNRAS, 311, 793
- Bernardeau F., Colombi S., Gaztañaga E., Scoccimarro R., 2002, PhR, 367, 1
- Bertschinger E., 1998, ARA&A, 36, 599
- Bharadwaj S., Nath B. B., Sethi S. K., 2001, JApA, 22, 21
- Bharadwaj S., Sethi S. K., 2001, JApA, 22, 293
- Bharadwaj S., Srikant P. S., 2004, JApA, 25, 67
- Bharadwaj S., Ali S. S., 2004, MNRAS, 352, 142
- Bharadwaj S., Ali S. S., 2005, MNRAS, 356, 1519

- Bharadwaj S., Sethi S. K., Saini T. D., 2009, PhRvD, 79, 083538
- Binney J., 1977, ApJ, 215, 483
- Binney J., Knebe A., 2002, MNRAS, 333, 378
- Binney J., 2004, MNRAS, 350, 939
- Bode P., Ostriker J. P., 2003, ApJS, 145, 1
- Bode P., Ostriker J. P., Xu G., 2000, ApJS, 128, 561
- Bond J. R., Cole S., Efstathiou G., Kaiser N., 1991, ApJ, 379, 440
- Bouchet F. R., Adam J.-C., Pellat R., 1985, A&A, 144, 413
- Bouchet F. R., Kandrup H. E., 1985, ApJ, 299, 1
- Bouchet F. R., Hernquist L., 1988, ApJS, 68, 521
- Bowman J. D., et al., 2007, AJ, 133, 1505
- Bowman J. D., 2007, PhD Thesis, pp. 17
- Brainerd T. G., Scherrer R. J., Villumsen J. V., 1993, ApJ, 418, 570
- Brieu P. P., Evrard A. E., 2000, NewA, 5, 163
- Brieu P. P., Summers F. J., Ostriker J. P., 1995, ApJ, 453, 566
- Bromm V., Larson R. B., 2004, ARA&A, 42, 79
- Bryan G. L., Norman M. L., 1998, ApJ, 495, 80
- Chengalur J. N., Kanekar N., 2000, MNRAS, 318, 303
- Cohn J. D., White M., 2008, MNRAS, 385, 2025
- Cooray A., Sheth R., 2002, PhR, 372, 1

- Couchman H. M. P., 1991, ApJ, 368, L23
- Couchman H. M. P., Thomas P. A., Pearce F. R., 1995, ApJ, 452, 797
- Datta, K. K., Bharadwaj, S., & Choudhury, T. R. 2007, , MNRAS **3**, 82, 809
- Datta K. K., Choudhury T. R., Bharadwaj S., 2007, MNRAS, 378, 119
- Davis M., Peebles P. J. E., 1977, ApJS, 34, 425
- Davis M., Efstathiou G., Frenk C. S., White S. D. M., 1985, ApJ, 292, 371
- Diemand J., Moore B., Stadel J., Kazantzidis S., 2004, MNRAS, 348, 977
- Dehnen W., 2000, ApJ, 536, L39
- Dehnen W., 2001, MNRAS, 324, 273
- Dehnen W., 2002, JCoPh, 179, 27
- Dekel, A., & Lahav, O. 1999, ApJ, 520, 24
- Dolag K., Borgani S., Schindler S., Diaferio A., Bykov A. M., 2008, SSRv, 134, 229
- Dubinski J., 1996, NewA, 1, 133
- Dubinski J., Kim J., Park C., Humble R., 2004, NewA, 9, 111
- Dyer C. C., Ip P. S. S., 1993, ApJ, 409, 60
- Ebisuzaki T., Makino J., Fukushige T., Taiji M., Sugimoto D., Ito T., Okumura S. K., 1993, PASJ, 45, 269
- Efstathiou G., Davis M., White S. D. M., Frenk C. S., 1985, ApJS, 57, 241
- Efstathiou G., Frenk C. S., White S. D. M., Davis M., 1988, MNRAS, 235, 715
- Eke V. R., Cole S., Frenk C. S., 1996, MNRAS, 282, 263
- El-Zant A. A., 2006, MNRAS, 370, 1247

- Evrard A. E., 1988, MNRAS, 235, 911
- Evrard A. E., Crone M. M., 1992, ApJ, 394, L1
- Fan X., Carilli C. L., Keating B., 2006, ARA&A, 44, 415
- Fan X., et al., 2006, AJ, 132, 117
- Field G. B., 1958, Proc. I.R.E., 46, 240
- Field G. B., 1959, ApJ, 129, 536
- Fiedmann A., 1922, Z. Phys. **10**, 377
- Fry J. N., 1996, ApJ, 461, L65
- Furlanetto S. R., Oh S. P., Briggs F. H., 2006, PhR, 433, 181
- Gardner J. P., Katz N., Hernquist L., Weinberg D. H., 2001, ApJ, 559, 131
- Gelb, J. M., & Bertschinger, E. 1994, ApJ, 436, 491
- Gingold R. A., Monaghan J. J., 1977, MNRAS, 181, 375
- Gingold R. A., Monaghan J. J., 1982, JCoPh, 46, 429
- <http://gmrt.ncra.tifr.res.in/>
- Greengard L., Rokhlin V., 1987, JCoPh, 73, 325
- Gunn J. E., Gott J. R. I., 1972, ApJ, 176, 1
- Gurbatov S. N., Saichev A. I., Shandarin S. F., 1989, MNRAS, 236, 385
- Haehnelt M. G., Steinmetz M., Rauch M., 2000, ApJ, 534, 594
- Hamana T., Yoshida N., Suto Y., 2002, ApJ, 568, 455
- Hamilton A. J. S., Kumar P., Lu E., Matthews A., 1991, ApJ, 374, L1

- Heath D. J., 1977, MNRAS, 179, 351
- Heitmann K., Ricker P. M., Warren M. S., Habib S., 2005, ApJS, 160, 28
- Heitmann K., et al., 2008, CS&D, 1, 015003
- Henry J. P., 2000, ApJ, 534, 565
- Hernquist L., 1987, ApJS, 64, 715
- Hernquist L., Katz N., 1989, ApJS, 70, 419
- Hernquist L., 1990, JCoPh, 87, 137
- Hernquist L., Barnes J. E., 1990, ApJ, 349, 562
- Hernquist L., Bouchet F. R., Suto Y., 1991, ApJS, 75, 231
- Hockney R. W., Eastwood J. W., 1988, Computer Simulation using Particles, McGraw-Hill
- Hoyle F., 1953, ApJ, 118, 513
- Hubble E., 1929, PNAS, 15, 168
- Hui L., Bertschinger E., 1996, ApJ, 471, 1
- Jeans J. H., 1902, RSPTA, 199, 1
- Jain B., Mo H. J., White S. D. M., 1995, MNRAS, 276, L25
- Jernigan J. G., Porter D. H., 1989, ApJS, 71, 871
- Jenkins A., Frenk C. S., White S. D. M., Colberg J. M., Cole S., Evrard A. E., Couchman H. M. P., Yoshida N., 2001, MNRAS, 321, 372
- Joyce M., Marcos B., Baertschiger T., 2008, arXiv, arXiv:0805.1357
- Kaiser N., 1987, MNRAS, 227, 1
- Kanekar N., 2000, ApJ, 531, 17

- Kanekar N., Prochaska J. X., Ellison S. L., Chengalur J. N., 2009, MNRAS, 396, 385
- Kawai A., Makino J., 2001, ApJ, 550, L143
- Khandai N., Bagla J. S., 2009, RAA, 9, 861
- Klypin A. A., Shandarin S. F., 1983, MNRAS, 204, 891
- Knebe A., Green A., Binney J., 2001, MNRAS, 325, 845
- Knebe A., Kravtsov A. V., Gottlöber S., Klypin A. A., 2000, MNRAS, 317, 630
- Komatsu E., et al., 2009, ApJS, 180, 330
- Kravtsov A. V., Klypin A. A., Khokhlov A. M., 1997, ApJS, 111, 73
- Kuhlman B., Melott A. L., Shandarin S. F., 1996, ApJ, 470, L41
- Kumar A., Padmanabhan T., Subramanian K., 1995, MNRAS, 272, 544
- Lacey C., Cole S., 1994, MNRAS, 271, 676
- Lah P., et al., 2007, MNRAS, 376, 1357
- Lah P., et al., 2009, arXiv, arXiv:0907.1416
- Landau L. D., Lifshitz E. M., 1975, The Classical Theory of Fields, Pergamon International Library of Science
- Lemaître G., 1931, MNRAS, 91, 490
- Lemaître G., 1931, MNRAS, 91, 483
- Little B., Weinberg D. H., Park C., 1991, MNRAS, 253, 295
- Loeb A., Barkana R., 2001, ARA&A, 39, 19
- Loeb A., Wyithe J. S. B., 2008, PhRvL, 100, 161301
- Lucy L. B., 1977, AJ, 82, 1013

- Lukić Z., Heitmann K., Habib S., Bashinsky S., Ricker P. M., 2007, ApJ, 671, 1160
- Ma C.-P., 1998, ApJ, 508, L5
- Macfarland T., Couchman H. M. P., Pearce F. R., Pichlmeier J., 1998, NewA, 3, 687
- Magliocchetti M., Bagla J. S., Maddox S. J., Lahav O., 2000, MNRAS, 314, 546
- Makino J., 1991, PASJ, 43, 621
- Makino J., 2004, PASJ, 56, 521
- Makino J., 2002, NewA, 7, 373
- Makino J., 1990, JCoPh, 87, 148
- Makino J., Fukushige T., Koga M., Namura K., 2003, PASJ, 55, 1163
- Majumdar S., Mohr J. J., 2003, ApJ, 585, 603
- Manera M., Sheth R. K., Scoccimarro R., 2009, arXiv, 0906.1314
- Matarrese S., Lucchin F., Moscardini L., Saez D., 1992, MNRAS, 259, 437
- McEwen J. D., Scaife A. M. M., 2008, MNRAS, 389, 1163
- McKee C. F., Ostriker E. C., 2007, ARA&A, 45, 565
- McQuinn, M., Zahn, O., Zaldarriaga, M., Hernquist, L., & Furlanetto, S. R. 2006, ApJ, 653, 815
- Melott A. L., Shandarin S. F., Splinter R. J., Suto Y., 1997, ApJ, 479, L79
- Merritt D., 1996, AJ, 111, 2462
- Merz H., Pen U.-L., Trac H., 2005, NewA, 10, 393
- Miller R. H., 1983, ApJ, 270, 390
- Mo H. J., White S. D. M., 1996, MNRAS, 282, 347

- Mo H. J., Mao S., White S. D. M., 1999, MNRAS, 304, 175
- Monaghan J. J., Lattanzio J. C., 1985, A&A, 149, 135
- Monaghan J. J., 1992, ARA&A, 30, 543
- Mould J. R., et al., 2000, ApJ, 529, 786
- Nakamura T. T., Suto Y., 1997, PThPh, 97, 49
- Navarro J. F., Frenk C. S., White S. D. M., 1996, ApJ, 462, 563
- Neistein E., Maccio A. V., Dekel A., 2009, arXiv, 0903.1640
- Ng K.-W., 2001, PhRvD, 63, 123001
- Ng K.-W., 2005, PhRvD, 71, 083009
- Nityananda R., Padmanabhan T., 1994, MNRAS, 271, 976
- O'Shea B. W., Nagamine K., Springel V., Hernquist L., Norman M. L., 2005, ApJS, 160, 1
- Padmanabhan T., 1993, Large Scale Structure in the Universe. Cambridge University Press
- Padmanabhan T., 1996, Cosmology and Astrophysics through Problems, Cambridge University Press
- Padmanabhan T., 1996, MNRAS, 278, L29
- Padmanabhan T., Cen R., Ostriker J. P., Summers F. J., 1996, ApJ, 466, 604
- Padmanabhan T., 2002, Theoretical Astrophysics, Volume III: Galaxies and Cosmology. Cambridge University Press.
- Peacock J. A., Dodds S. J., 1996, MNRAS, 280, L19
- Peacock J. A., Dodds S. J., 1994, MNRAS, 267, 1020
- Peacock J. A., 1999, Cosmological Physics, Cambridge University Press

- Peebles P. J. E., 1974, A&A, 32, 391
- Peebles P. J. E., 1980, The Large-Scale Structure of the Universe, Princeton University Press
- Peebles P. J. E., 1993, Principles of physical cosmology, Princeton University Press
- Percival W. J., et al., 2007, ApJ, 657, 645
- Péroux C., Dessauges-Zavadsky M., D'Odorico S., Sun Kim T., McMahon R. G., 2005, MNRAS, 363, 479
- Power C., Knebe A., 2006, MNRAS, 370, 691
- Pontzen A., et al., 2008, MNRAS, 390, 1349
- Prasad J., 2007, JApA, 28, 117
- Press W. H., Schechter P., 1974, ApJ, 187, 425
- Price D. J., Monaghan J. J., 2007, MNRAS, 374, 1347
- Pritchard J. R., Loeb A., 2008, PhRvD, 78, 103511
- Purcell E. M., Field G. B., 1956, ApJ, 124, 542
- Ray S., Bagla J. S., 2004, astro, arXiv:astro-ph/0405220
- Rao S. M., Turnshek D. A., 2000, ApJS, 130, 1
- Reed D., Gardner J., Quinn T., Stadel J., Fardal M., Lake G., Governato F., 2003, MNRAS, 346, 565
- Reed D. S., Bower R., Frenk C. S., Jenkins A., Theuns T., 2007, MNRAS, 374, 2
- Reed D. S., Bower R., Frenk C. S., Jenkins A., Theuns T., 2009, MNRAS, 394, 624
- Rees M. J., Ostriker J. P., 1977, MNRAS, 179, 541
- Robertson H. P., 1929, PNAS, 15, 822

- Robertson H. P., 1935, ApJ, 82, 284
- Romeo A. B., Agertz O., Moore B., Stadel J., 2008, ApJ, 686, 1
- Roukema B. F., Valls-Gabaud D., 1998, wfsc.conf, 414
- Roukema B., Valls-Gabaud D., 2000, ASPC, 200, 24
- Sahni V., Coles P., 1995, PhR, 262, 1
- Salmon J. K., Warren M. S., 1994, JCoPh, 111, 136
- Sarkar P., Yadav J., Pandey B., Bharadwaj S., 2009, arXiv, arXiv:0906.3431
- Scott D., Rees M. J., 1990, MNRAS, 247, 510
- Shandarin S. F., Zeldovich Y. B., 1989, RvMP, 61, 185
- Sheth R. K., Tormen G., 1999, MNRAS, 308, 119
- Sheth R. K., Mo H. J., Tormen G., 2001, MNRAS, 323, 1
- Silk J., 1977, ApJ, 211, 638
- Smith R. E., et al., 2003, MNRAS, 341, 1311
- Smoot G. F., et al., 1992, ApJ, 396, L1
- Spergel D. N., et al., 2007, ApJS, 170, 377
- Splinter R. J., Melott A. L., Shandarin S. F., Suto Y., 1998, ApJ, 497, 38
- Springel V., Yoshida N., White S. D. M., 2001, NewA, 6, 79
- Springel V., Hernquist L., 2002, MNRAS, 333, 649
- Springel V., 2005, MNRAS, 364, 1105
- Springel V., et al., 2005, Natur, 435, 629

- Storrie-Lombardi L. J., McMahon R. G., Irwin M. J., 1996, MNRAS, 283, L79
- Subramanian K., Padmanabhan T., 1993, MNRAS, 265, 101
- Suisalu I., Saar E., 1995, MNRAS, 274, 287
- Sunyaev R. A., Zeldovich Y. B., 1972, A&A, 20, 189
- Sunyaev R. A., Zeldovich I. B., 1975, MNRAS, 171, 375
- Szebehely V., Peters C. F., 1967, AJ, 72, 1187
- Thacker R. J., Couchman H. M. P., 2006, CoPhC, 174, 540
- Theis C., 1998, A&A, 330, 1180
- Theuns T., 1994, CoPhC, 78, 238
- Thiébaut J., Pichon C., Sousbie T., Prunet S., Pogosyan D., 2008, MNRAS, 387, 397
- Tinker J., Kravtsov A. V., Klypin A., Abazajian K., Warren M., Yepes G., Gottlöber S., Holz D. E., 2008, ApJ, 688, 709
- Trimble V., 1987, ARA&A, 25, 425
- van de Hulst H. C., Raimond E., van Woerden H., 1957, BAN, 14, 1
- Warren M. S., Abazajian K., Holz D. E., Teodoro L., 2006, ApJ, 646, 881
- Wadsley J. W., Stadel J., Quinn T., 2004, NewA, 9, 137
- Walker A. G., 1936, Proc. London Math. Soc **42**, 90
- Weinberg S., 2008, Cosmology, Oxford University Press
- White S. D. M., Frenk C. S., 1991, ApJ, 379, 52
- White M., 2002, ApJS, 143, 241
- Wolfe A. M., Gawiser E., Prochaska J. X., 2005, ARA&A, 43, 861

- Wouthuysen S., 1952a, *Phy*, 18, 75
- Wouthuysen S. A., 1952b, *AJ*, 57, 31
- Wyithe J. S. B., Loeb A., Geil P. M., 2008, *MNRAS*, 383, 1195
- Wyithe S., 2008, arXiv, arXiv:0804.1624
- Xu G., 1995, *ApJS*, 98, 355
- Yadav J., Bharadwaj S., Pandey B., Seshadri T. R., 2005, *MNRAS*, 364, 601
- Yoshikawa K., Fukushige T., 2005, *PASJ*, 57, 849
- Zel'Dovich Y. B., 1970, *A&A*, 5, 84
- Zhan H., 2006, *ApJ*, 639, 617
- Zinnecker H., Yorke H. W., 2007, *ARA&A*, 45, 481
- Zwaan M. A., Meyer M. J., Staveley-Smith L., Webster R. L., 2005, *MNRAS*, 359, L30